Aspects of QCD on the lattice: Scaling and hadron masses.

Trivini, Aurora

Trivini, Aurora (2007) *Aspects of QCD on the lattice: Scaling and hadron masses..* thesis, Swansea University.
http://cronfa.swan.ac.uk/Record/cronfa42604

Aspects of QCD on the Lattice: Scaling and Hadron Masses

Aurora Trivini

Swansea University
Prifysgol Abertawe

SUBMITTED TO THE UNIVERSITY OF WALES
IN FULFILMENT OF THE REQUIREMENTS OF
DOCTOR OF PHILOSOPHY
AT
SWANSEA UNIVERSITY
SINGLETON PARK SWANSEA
SA2 8PP

Abstract

This thesis explores different aspects of QCD and QCD-like theories through the use of Lattice Gauge Theory (LGT).

This work is composed of three different projects: the first one investigating the scaling behaviour of pure $SU(N)$ gauge theories; the other two investigating and calculating hadron masses, using Domain Wall gauge configurations.

In the first project (chapter 3) the Lattice-Distorted Perturbation Theory approach to the lack of asymptotic scaling for Monte Carlo data is described. Quenched Monte Carlo data from different sources, different observables and different gauge actions are considered. The main purpose of our calculations is to show the importance of lattice corrections in the relationship between the running coupling $g^2(a)$ and the lattice spacing a, where $g^2(a)$ is either the bare lattice coupling or some renormalized one. We show not only that the $\mathcal{O}(a^n)$ corrections are not negligible, but also that their coefficients turn out to be the order we expect. We consider a parametrization of the lattice β-function which includes both the $\mathcal{O}(a^n)$ corrections and higher order terms in g^2, since the observed lack of asymptotic scaling is presumably due to a mixture of the two effects: the presence of lattice artefacts due to the finiteness of a and the inclusion of only a finite number of terms in the perturbative expansion (renormalized coupling approach). We study these two effects both together and separately. Furthermore, we apply our approach to $SU(N)$ data for the number of colours $N \neq 3$, and show the validity of the Lattice-Distorted PT method in particular at large N. All our investigations lead to a remarkable consistency both in the fitted Λ parameters and in the size of the $\mathcal{O}(a^n)$ corrections.

The second part of this work (chapter 4) uses lattice QCD for spectroscopy studies with Domain Wall gauge configurations generated with the Iwasaki gauge action by the RBC-UKQCD collaboration, at fixed lattice spacing. In particular, a study of nucleon masses is presented on two different lattice sizes. The calculation of the nucleon mass is a very good test for LGT since its value can be compared with the one very accurately determined by experiments. Furthermore, LGT can be a powerful predictive tool for other baryonic states whose experimental values are not known as accurately as the nucleon one. Here we present results using correlation functions at unitary, $m_{val} = m_{sea}$, and non-unitary points, multiple sources per configuration and several different types of smearing to improve the signal. Firstly, we determine the masses for each channel via a fit to individual correlators; then in order to increase the precision of the result, we fit the correlation functions simultaneously to the same mass M for each channel. The study also includes the nucleon parity partner, N^*.

In chapter 5 preliminary results are presented for a study of the D_s meson spectrum. The discoveries of new resonances D_{sJ} some years ago have provoked much interest in heavy-light systems in general and in the D_s mesons in particular. The existence and properties of the multiplet $\{0^+, 1^+\}$, partner of the $\{0^-, 1^-\}$, were predicted from the theory before its discovery. In fact the mass splittings between these different states can be understood in terms of a combination of heavy quark and chiral symmetry. In particular, the quantities mainly investigated in D_s

calculations are the parity and hyperfine splittings, in order to compare them with their experimental values, and their independence on the spin and on the parity respectively. We carry out this study using dynamical domain wall configurations. The novelty of our study is considering the charm quark propagating as an overlap fermion and the strange quark as a domain wall fermion. Also a quenched calculation is performed with identical valence quarks as the dynamical case in order to investigate sea quark effects.

To my family

Declaration

This thesis is the result of my own investigations, except where otherwise stated. Other sources are acknowledged by explicit references. A bibliography is appended.
Some preliminary results of the calculations in chapter 3 are in

- Asymptotic scaling and Monte Carlo data, A. Trivini and C. R. Allton, PoS **LAT2005** (2006) 036 [arXiv:hep-lat/0511006].

The results in chapter 3 will appear in a paper which is in progress.

Chapter 4 is part of the ongoing baryon project by the baryon group of the RBC-UKQCD collaboration. The results in chapter 4 will appear in a paper which is in preparation. The DWF gauge configurations in both chapter 4 and 5, as well as the correlators in chapter 4, were generated on the QCDOC machines in Edinburgh and Columbia University jointly by members of the RBC-UKQCD collaboration.

The project in chapter 5 is carried out in collaboration with Chris Maynard and Robert Tweedie within the RBC-UKQCD collaboration. The quenched gauge configurations were generated by Alistair Hart. The meson correlators, unquenched and quenched, were generated by me using UKQCD computer code. Preliminary results of the calculations in chapter 5 are in

- Exploratory study of the D_s spectrum in 2+1 domain wall QCD with heavy overlap, C. Allton, C. Maynard, A. Trivini and R. Tweedie, PoS **LAT2006** (2006) 202 [arXiv:hep-lat/0610068].

This work has not previously been accepted in substance for any degree and is not being concurrently submitted in candidature for any degree.

I hereby give consent for my thesis, if accepted, to be available for photocopying and for inter-library loan, and for the title and summary to be made available to outside organisations.

Signature of Author

16/11/2007

Date

Acknowledgements

This work would not have been possible without the support and help of many people I take the chance to thank now.

Firstly I am very grateful to my supervisor Chris Allton for all he taught me through all my PhD, as well as for his support and patience in listening and answering even stupid questions. I also would like to thank all the Physics group in Swansea University for the friendly welcome and nice atmosphere through the years. A special thought to Dave, Linda and Ray for the prompt help they always offered. I also would like to thank Swansea University for providing funding and making all this possible.

I thank members of the RBC and UKQCD collaborations who I had useful discussions with: in particular while visiting Edinburgh University and Brookhaven National Laboratory, I learnt a lot from Chris Maynard, Robert Tweedie and Meifeng Lin.

My years in Swansea would have been mush less enjoyable without the company of many colleagues and friends, especially Avtar, Andy, Steve, Antonio and Emiliano: I especially thank Emiliano for listening to me and my frustrations in the last few months. My thoughts also go to all the special friends I found in my first year in Beck House, in particular Gayane, Annie, Ganesh, Arun and Deepak: I hope to see you all again soon. I cannot forget my dearest friends in Italy. A list will be too long, but hopefully I will have the chance to thank them in person. However, I would like to name my dearest friend Bianca, who so promptly came to visit me and get to know my life here.

I am also grateful to Mestre Maxwell, Teacher Soraia and all the Ile de Capoeira Welsh School to help me relieve the stress of my final year through movement as well a smile and laugh. Through them I met people I will never forget: above all Amy.

My experience in Swansea of course is made of all the persons I met over these three years, but a special place is definitely taken by Avtar: these three years would have been much different without him and the special relation between us.

Finally and most importantly, there are no words to explain how thankful I am to all my family. The smile of my splendid nieces often kept me up in bad moments: I only wish I had spent more time with them. I will always be grateful to my parents, my brother and my sister in law for their unconditional love and support. To all my family I dedicate this thesis.

Contents

Chapter 1

Introduction

Quantum field theories are the generally accepted framework for describing the electromagnetic, weak and strong interactions between elementary particles. The Standard Model is up to now the most successful description of the interactions of elementary particles. This theory incorporates quantum electrodynamics (QED), the electroweak theory of Glashow, Salam and Weinberg, and quantum chromodynamics (QCD), the currently accepted framework to describe strong interactions. The Lagrangian describing these combined quantum fields has a $SU(3)_C \times SU(2)_L \times U(1)_Y$ gauge symmetry[1], with degrees of freedom respectively *colour* for $SU(3)$, *weak isospin* for $SU(2)$ and *weak hypercharge* for $U(1)$.

The elementary particles which are currently known to exist in nature are *fermions*, divided into two categories, leptons and quarks, and *gauge bosons*, which mediate or 'carry' the fundamental forces between fermions. The photon γ is the mediator of the electromagnetic interactions and is massless; the gauge bosons corresponding to the weak interactions are the massive $W^{\pm}$ and Z; finally, the strong force is mediated by a 'colour' octet of massless gluons. Both leptons and

---

[1] A gauge theory is a theory which is invariant under a set of (gauge) local transformations, i.e. transformations that depend on space and time.

quarks can interact via the weak nuclear force and, excluding the neutral leptons, or neutrinos, via the electromagnetic force. Quarks, carrying the *colour charge*, are also subject to strong interactions, or in other words, $SU(3)_C$ acts only on the colour degree of freedom. The strong interactions are flavour blind, but sensitive to colour. From this QCD takes its name. The fact that its gauge group $SU(3)$ is non-Abelian makes QCD a very different theory from QED.

QCD presents two peculiar properties: *asymptotic freedom* and *confinement*, related to the strong interactions properties in the high and low energy regimes respectively. As discussed in more detail later in this work, the coupling constant in a non-Abelian theory becomes a *running coupling*. Asymptotic freedom tells us that at small quark separations the coupling of QCD becomes so small that quarks are like free particles: this allows perturbative methods to provide reliable predictions for physical observables in processes involving only high momenta or short distances. However, in order to study hadrons and quarks and understand better their features, perturbative methods cannot be applied, since the coupling constant becomes very large at scales corresponding to the size of hadrons (large distances, low energies). Quarks have never been detected in isolation, but only as constituents of hadrons: the non-observation of free colour charges is called confinement.

Lattice field theory is a non-perturbative method that provides a very powerful tool in the investigation of low energy QCD. Lattice QCD, LQCD, was first proposed by Wilson in 1974 [1] to investigate the confinement mechanism of quarks. Until then all predictions of QCD were restricted to the perturbative regime. LQCD mainly provides a numerical way of testing low energy QCD by calculating the masses of the hadrons and then comparing them with their experimental values. In fact, the QCD Lagrangian (see Section 2.2) has seven unknown input parameters: the coupling constant and the masses of the up, down, strange, charm, bottom and top quarks. In the lattice formulation, once these free parameters have been fixed in terms of seven measured hadron masses for instance, the properties of the other particles made up of these quarks and gluons have to agree with experiments. Thus this formulation of a gauge field theory on a discretized Euclidean space-time, allows the evaluation of physical observables from first principles. LQCD also may be used as a predictive tool for quantities difficult to be measured directly by experiments.

The natural framework to quantize the lattice theory is the path integral formalism: the path integrals corresponding to expectation values of physical observables can be computed numerically via Monte Carlo simulations. This is an important advantage of the lattice formulation. However for years, the applicability of lattice gauge theory was strongly constrained by limited computational resources. Therefore, the quenched approximation has been for a long time the main framework for lattice calculations: it consists in excluding the contribution from dynamical quarks, introducing many unphysical effects into lattice simulations. Fortunately, the availability of powerful computational resources, together with algorithmic advancements in recent years, allows us to simulate dynamical quarks. Of course this is much more expensive and constant further development is necessary in order to include the correct number of flavours as well as simulate at quark masses closer to the physical ones (in other words, require the correct flavour and chiral symmetries of QCD).

In the next chapter, after a brief review of the main features of QCD in the continuum, the basic ideas and concepts behind lattice gauge theories, and in particular lattice QCD, are explored. More emphasis will be given to those topics that will be of use for the calculations described later in this work.

Chapters 3, 4 and 5 explore different aspects of LQCD.

Chapter 3 investigates the generally known problem that the behaviour predicted from perturbation theory for asymptotically free theories like QCD has not been directly observed in Monte Carlo simulations. In particular, we show that the lattice artefacts due to the finiteness of the lattice spacing give the best explanation to such disagreement. We also explore the possibility that this discrepancy is due to the poor convergence properties of the perturbative series in the bare coupling constant, by replacing it with some renormalized coupling constants. Preliminary results of the same calculations applied to $SU(N)$ data, with the number of colours N different from 3, are also presented. All the data considered are from quenched calculations. An estimate of the $SU(3)$ $\Lambda_{\overline{MS}}$ in the Wilson gauge action case is also given.

A study of the nucleon state and its parity partner is carried out in chapter 4, as part of a more comprehensive calculation of the baryon spectrum by the RBC-UKQCD collaboration. The nucleon correlators are obtained from simulations of domain wall QCD with one dynamical flavour approximating the strange quark, and two degenerate dynamical flavours approximating the up and down quarks. Two different lattice sizes are considered at fixed lattice spacing and several kind of smearing are implemented while generating the nucleon correlators. Our results for the nucleon mass are in good agreement with the experimental values.

Chapter 5 presents preliminary results of the D_s meson spectrum on the same $2+1$ domain wall gauge background with a single lattice spacing. We implement the strange quark as a domain wall fermion and the charm quark as an overlap fermion, in order to make good use of the chiral properties of domain wall fermions and the $\mathcal{O}(am_c)$ error suppression from the overlap formalism. A quenched calculation is also performed in order to investigate possible sea quark effects. We investigate the signal of different J^P channels and perform a study of the dispersion relation, as a reflection of the $\mathcal{O}(a^2m_c^2)$ errors. We find that the parity splittings, at least for the two heavier mesons considered, are in agreement with the experimental values within rather large errors. The hyperfine splitting is overestimated, in both the dynamical and quenched case. Our calculations seem to be affected by $\mathcal{O}(a^2m_c^2)$: a finer lattice spacing is therefore necessary.

Finally, our conclusions are summarized in chapter 6.

Chapter 2

Background Theory

LQCD calculations are non-perturbative implementations of field theory based upon the Feynman path integral approach. The technique essentially involves a rotation to the Euclidean metric and the discretization of space-time to obtain a finite hyper-cubic lattice. In this formulation the system takes the form of a classical four-dimensional statistical model. The path integrals can then be performed over the discretized space-time using numerical methods. The matter fields are treated as classical stochastic variables assigned to the points of the lattice, while the gauge fields are associated to the links. A fundamental requirement is that the continuum limit of the lattice action reproduces the correct continuum action. Before going into more details, let us have a closer look at the path integrals and the continuation to imaginary time.

2.1 Path Integral Approach

Path integrals are used to calculate the expectation values of the physical observables of a quantum field theory. In QCD, given some observable $\mathcal{O}[\psi, \bar{\psi}, \mathrm{A}_\mu]$ in terms of the time-ordered product of gauge and quarks fields, its expectation value in the Feynman path integral approach is given by:

$$\langle 0|\mathcal{T}\mathcal{O}[\psi,\bar{\psi},\mathrm{A}_\mu]|0\rangle = \frac{1}{\mathcal{Z}}\int \mathcal{D}\psi\mathcal{D}\bar{\psi}\mathcal{D}\mathrm{A}_\mu \mathcal{O}[\psi,\bar{\psi},\mathrm{A}_\mu]e^{iS[\psi,\bar{\psi},\mathrm{A}_\mu]}, \tag{2.1}$$

where $\mathcal{Z}$ is the partition function

$$\mathcal{Z} = \int \mathcal{D}\psi\mathcal{D}\bar{\psi}\mathcal{D}\mathrm{A}_\mu e^{iS[\psi,\bar{\psi},\mathrm{A}_\mu]} \tag{2.2}$$

and S is the action of the theory, related to the Lagrangian density $\mathcal{L}(\psi,\bar{\psi},\mathrm{A}_\mu)$ by

$$S[\psi,\bar{\psi},\mathrm{A}_\mu] = \int d^4x\mathcal{L}(\psi,\bar{\psi},\mathrm{A}_\mu). \tag{2.3}$$

Since we are particularly interested in QCD, the expression for the QCD action is explained in section 2.2 .

The integral (2.1) is over all field values, $\psi(x), \bar{\psi}(x)$ and $A_\mu(x)$, and since space-time is continuous, this means it is over an infinite number of degrees of freedom. Later in this chapter it is shown how to introduce a lattice of points in space and time and overcome this problem.

The second thing to notice is that the functional integral is complex and strongly oscillating. The way to overcome this issue is performing all calculations in Euclidean space rather than Minkowsky space. There is no loss of generality in this, since path integrals in the Minkowsky space can be obtained by analytic continuation of the Euclidean ones. Performing an analytic continuation to imaginary time, essentially by making the substitution $t \to -it$[1], gives the Euclidean partition function as

$$\mathcal{Z}_E = \int \mathcal{D}\psi\mathcal{D}\bar{\psi}\mathcal{D}\mathrm{A}_\mu e^{-S_E[\psi,\bar{\psi},\mathrm{A}_\mu]}, \tag{2.4}$$

---

[1] Or in other words by performing a Wick rotation: $x_0 \to -ix_0,\ x_i \to x_i$.

where S_E denotes the action in the Euclidean space. The partition function is now similar to those in statistical mechanics, weighted by the factor e^{-S_E} instead of the Boltzmann factor. The integrand is now real and exponentially decreasing, that means numerically tractable. Note that all the indices E will be dropped from now on.

We now have a closer look at the QCD action, first in the continuum, then at its discretized form.

2.2 Quantum Chromodynamics

Quantum Chromodynamics (QCD) is a non-Abelian gauge theory invariant under colour $SU(3)$ transformations. It is currently the best description of the strong interactions and owes its name to the colour quantum numbers of quarks and gluons. The quarks belong to the fundamental representation of the colour $SU(3)$ gauge group, while their antiparticles belong to the conjugate representation. These particles interact via the exchange of vector bosons called gluons, corresponding to the eight generators of the $SU(3)$ group. The quarks also carry flavour degrees of freedom which are independent of the colour. At present, there are six flavours, forming three generations of quarks, $(u, d), (c, s)$ and (t, b).

The Lagrangian density of QCD is given by

$$\mathcal{L}_{QCD} = \sum_{i=1}^{N_f} \bar{\psi}_i^{\alpha}(x)(i\not{D} - m_i)^{\alpha\beta}\psi_i^{\beta}(x) - \frac{1}{4}F^a_{\mu\nu}F^{\mu\nu}_a, \tag{2.5}$$

where $\psi_i(x)$ is the fermionic field corresponding to a quark of flavour i with mass m_i: it is a 4-component spinor and the conjugate field $\bar{\psi}$ is given by

$$\bar{\psi} = \psi^{\dagger}\gamma_4. \tag{2.6}$$

Note that m_i is a $N_f \times N_f$ mass matrix in the flavour space. The sum in (2.5) is over the number of flavours, α and β run over the 3 colours, and the covariant derivative is defined as

$$\not{D} = \gamma^\mu D_\mu = \gamma^\mu(\partial_\mu - igA_\mu(x)), \tag{2.7}$$

in terms of the vector gauge fields $A_\mu(x) = \sum_a \lambda^a A^a_\mu(x)$, with λ^a, $a = 1, ..., 8$, denoting the Gell-Mann matrices, generators of the $SU(3)$ group[2]. The field strength tensor is related to the vector potential through

$$F^a_{\mu\nu} = \partial_\mu A^a_\nu - \partial_\nu A^a_\mu - g f_{abc} A^b_\mu A^c_\nu, \tag{2.8}$$

where f_{abc} are the completely antisymmetric structure constants of the $SU(3)$ group and g the bare coupling constant. The covariant derivative (2.7), with the gauge fields $A_\mu(x)$, is introduced in order for the Lagrangian density to remain invariant under a local gauge transformation

$$S(x) \equiv e^{i\alpha_a(x)\lambda^a}, \tag{2.9}$$

where $\alpha_a(x)$, $a = 1, ..., 8$, are a set of arbitrary $SU(3)$ group parameters. The third term in (2.8) is typical of non-Abelian gauge theories: it implies that the gauge fields can self-interact, since the Yang-Mills piece in the Lagrangian density will involve triple and quartic interaction terms such as:

$$+g f_{abc}(\partial_\mu A^a_\nu) A^b_\mu A^c_\nu - \frac{1}{4} g^2 f_{abc} f_{ade} A^b_\mu A^c_\nu A^d_\mu A^e_\nu. \tag{2.10}$$

This means that gluons themselves carry colour.

---

[2] The $SU(3)$ Lie algebra generators satisfy $[\lambda^a, \lambda^b] = i f^{abc}\lambda^c$ and $Tr(\lambda^a\lambda^b) = \frac{\delta^{ab}}{2}$ in the fundamental representation. See Appendix A for their expression.

2.3 Lattice Discretization

At long distances, the self-interaction of the gauge bosons, or gluons, leads to an increase in the coupling strength, which allows only non-perturbative treatments, like lattice QCD, to extract physics from QCD.

The QCD action has to be transcribed onto a discrete space-time lattice in such a way to preserve all the key properties of QCD. The simplest choice is an isotropic hyper-cubic space-time lattice with lattice spacing a, the distance between two sites, equal in both spatial and time directions. The continuum space-time index x_μ is replaced by a discrete index n_μ, only defined on the sites of the lattice, i.e.

$$x_\mu = n_\mu a, \qquad n_\mu = 0, 1, ..., N_{s,t} - 1, \tag{2.11}$$

where $N_{s,t}$ determines the size L of the lattice, $L_{s,t} = N_{s,t}a$, in the spatial and time direction respectively. Consequently, the fermionic fields $\psi(n)$, $\bar{\psi}(n)$ are now only defined on the lattice sites.

For numerical simulations all the parameters need to be scaled by the lattice spacing according to their canonical dimensions[3]. Also the integration over the Euclidean space-time is replaced by the sum over all sites on the lattice, and the derivatives become finite differences, i.e.[4]

$$\partial_\mu \psi(x) = \partial_\mu \psi(n) = \frac{1}{2a}[\psi(n + \hat{\mu}) - \psi(n - \hat{\mu})], \tag{2.12}$$

where $\hat{\mu}$ is a unit vector in the μ direction (the hats will be dropped in the following).

---

[3] For example, $\psi(x) \rightarrow \frac{1}{a^{3/2}}\psi(n)$.

[4] Note that a different choice could be made as long as the ordinary derivative is recovered in the limit $a \rightarrow 0$.

2.4 The Gauge Action

The gauge part of the action, the second term in (2.5), is constructed from elements of $SU(3)$ corresponding to transporters of the field from a lattice site n to a neighbouring site $n+\mu$, defined as $U(n, n+\mu) = U_\mu(n)$. Since these group elements live on the links connecting two sites, they are often called *link variables*. Thanks to their unitarity, the conjugate $U_\mu^\dagger(n)$ connects the two sites in the opposite direction, i.e. $U(n, n+\mu) = U^\dagger(n+\mu, n)$ (see figure 2.1). Each link transforms under the $SU(3)$ gauge group in the fundamental representation as

$$U(n, n+\mu) \rightarrow U'(n, n+\mu) = S(n)U(n, n+\mu)S^\dagger(n+\mu), \qquad S(n) \in SU(3). \quad (2.13)$$

In section 2.5, we will see how $U(n, n+\mu)$ allows to construct a gauge invariant bilinear term with fermionic fields, i.e. $\bar{\psi}(n)U(n,m)\psi(m)$, where $U(n,m)$ can be written as

$$U(n,m) = e^{ig\int_m^n A_\mu(z_n)dz_{n_\mu}}, \quad (2.14)$$

and in the limit of small a,

$$U(n,m) = e^{iagA_\mu(n)} \sim 1 + iagA_\mu(n), \quad (2.15)$$

where $A_\mu(n)$ is the gauge potential on the site n. The simplest gauge invariant object that we can build from the link variables is the trace of the product of gauge links along a closed curve, referred to as a Wilson loop. The smallest and simplest such loop is the plaquette, graphically represented in figure 2.1,

$$P_{\mu\nu}(n) = U_\mu(n)U_\nu(n+\mu)U_\mu^\dagger(n+\nu)U_\nu^\dagger(n). \quad (2.16)$$

Note that the order is important since the $U_\mu(n)$ matrices do not commute. The Wilson gauge action [1] is defined in terms of these plaquette variables,

$$S_G = \frac{\beta}{N_c} \sum_{\mu<\nu} \mathcal{R}eTr(1 - P_{\mu\nu}(n)), \tag{2.17}$$

where the coupling, g, has been written in terms of the constant $\beta = \frac{2N_c}{g^2}$ with N_c number of colours; the trace is over the colour indices and the sum is over all plaquettes on the lattice with $\mu < \nu$. It can be shown that the action (2.17) reproduces the correct continuum limit expression when $a \to 0$. Substituting the expression (2.15) for the link variable in eq.(2.16), we obtain

$$P_{\mu\nu}(n) = e^{iagA_\mu(n)} e^{iagA_\nu(n+\mu)} e^{-iagA_\mu(n+\nu)} e^{-iagA_\nu(n)}. \tag{2.18}$$

For small a, we can expand this expression in powers of a using

$$A_\mu(n+\nu) = A_\mu(n) + a\partial_\nu A_\mu(n) + \mathcal{O}(a^2); \tag{2.19}$$

then applying the Baker-Campbell-Hausdorff formula

$$e^A e^B = e^{A+B+\frac{1}{2}[A,B]+\dots} \tag{2.20}$$

gives

$$P_{\mu\nu}(n) = e^{ia^2 g F_{\mu\nu}(n)}, \tag{2.21}$$

with $F_{\mu\nu}$ given by

$$F_{\mu\nu} = \partial_\mu A_\nu - \partial_\nu A_\mu + ig[A_\mu, A_\nu], \tag{2.22}$$

analogous in components to eq.(2.8). Expanding eq.(2.21) gives

$$P_{\mu\nu}(n) = 1 + ia^2 g F_{\mu\nu}(n) - \frac{g^2 a^4}{2} F_{\mu\nu}(n) F^{\mu\nu}(n) + \mathcal{O}(a^6), \tag{2.23}$$

which, once substituted in (2.17), will give

$$S_G = a^4 \sum_n \sum_{\mu,\nu} [F_{\mu\nu}(n) F^{\mu\nu}(n) + \mathcal{O}(a^2)] \rightarrow \int d^4x F_{\mu\nu} F^{\mu\nu} + \mathcal{O}(a^2). \tag{2.24}$$

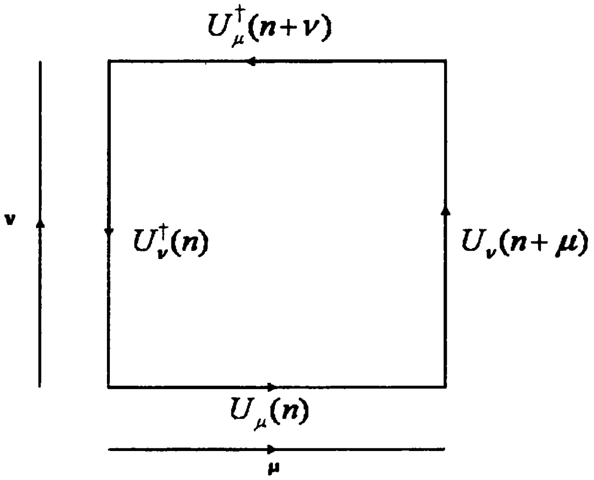

Figure 2.1: The plaquette in a two-dimensional isotropic lattice.

2.4.1 Improved Gauge Actions

As eq.(2.24) shows, the Wilson action suffers from $\mathcal{O}(a^2)$ errors, which can be significant if the lattice spacing a is not small enough. Improved gauge actions attempt to reduce the $\mathcal{O}(a^2)$ discretization errors further by adding irrelevant operators to the action, i.e. operators that go to zero in the continuum limit. This means adding some higher order terms to the action. The simplest choice are terms involving Wilson loops created from six links instead of four, as the standard plaquette. There are three types of six link loops that one can draw on the lattice: they are shown in fig. 2.2. The simplest example is the first one on the left, called planar rectangular 1 × 2 Wilson loop, $R_{\mu\nu}(n)$,

$$R_{\mu\nu}(n) = U_\mu(n)U_\mu(n+\mu)U_\nu(n+2\mu)U_\mu^\dagger(n+\mu+\nu)U_\mu^\dagger(n+\nu)U_\nu^\dagger(n). \qquad (2.25)$$

When the Wilson action is improved by adding this type of loop, the lattice gauge action becomes

$$S_G = -\frac{\beta}{N_c}(c_0\sum_n\sum_{\mu<\nu}\mathcal{R}eTr[P_{\mu\nu}(n)] + c_1\sum_n\sum_{\mu<\nu}\mathcal{R}eTr[R_{\mu\nu}(n)]). \qquad (2.26)$$

The coeffiecients c_0, c_1 are determined by Renormalization Group considerations and this kind of improved actions are called Renormalization Group Improved, RGI. The main idea of the RGI actions is to have an action as close as possible to the Renormalized Trajectory RT, where there are no scaling violations: for clarity, simulations done using an action along the exact RT, would reproduce the continuum physics without discretization errors. The RGI actions are usually obtained through block transformations, which rescale the size of the system and suppress the short distance lattice artefacts with a proper choice of the additional parameters c_i.

The most popular examples of this type of improved gauge actions in 2-parameter space (c_0, c_1) with the form (2.26) are the Iwasaki [2] and the Double Blocked Wilson (DBW2) [3] actions. Note that the two parameters follow the normalization condition $c_0 = (1 - 8c_1)$, in order to ensure that the correct gauge action is restored in the continuum limit. In particular, $c_1 = -1.4069$ for the DBW2 and $c_1 = -0.331$ for the Iwasaki gauge action.

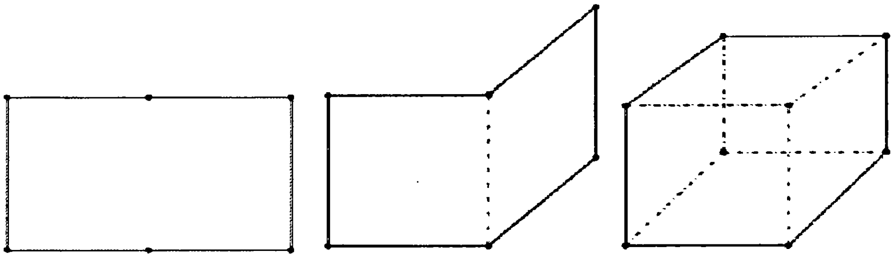

Figure 2.2: Six link loops: from left to right, the rectangle, the bent rectangle and the chair.

2.5 Fermions on Lattice

To discretize the Dirac fermionic action is less straightforward. Simply replacing the derivative in the Euclidean free fermion action

$$S_F = \int d^4x \bar{\psi}_f(x)(\gamma_\mu \partial_\mu + m_f)\psi_f(x) \tag{2.27}$$

with the symmetrized difference and applying the other transformations considered in section 2.3 leads to

$$S_F = \sum_{n,\mu} \frac{1}{2}\bar{\psi}(n)\gamma_\mu[\psi(n+\mu) - \psi(n-\mu)] + \sum_n m\bar{\psi}(n)\psi(n). \tag{2.28}$$

This discretized expression of the action contains bilinear terms in the fermionic fields, $\bar{\psi}(n)\psi(n+\mu)$, which are not invariant under a local gauge transformation

$$\psi(n) \to S(n)\psi(n) \qquad \bar{\psi}(n) \to \bar{\psi}(n)S^\dagger(n). \tag{2.29}$$

In fact,

$$\bar{\psi}(n)\psi(n+\mu) \to \bar{\psi}(n)S^\dagger(n)S(n+\mu)\psi(n+\mu), \tag{2.30}$$

and this is not surprising since we are trying to compare two fields at two different points in space-time. The solution is in the link variables (2.15) which allow to construct a gauge invariant bilinear term with fermionic fields, since $U_\mu(n)$ transforms according to eq.(2.13). Therefore, a more sensible substitution to the derivative piece of the action, including appropriate gauge links, leads to a discretized gauge invariant version of the fermion action

$$\begin{aligned} S_F &= \sum_{n,\mu} \frac{1}{2}\bar{\psi}(n)\gamma_\mu[U_\mu(n)\psi(n+\mu) - U_\mu^\dagger(n-\mu)\psi(n-\mu)] \\ &+ \sum_n m\bar{\psi}(n)\psi(n), \end{aligned} \tag{2.31}$$

commonly referred to as 'naive fermion action'.

2.5.1 Fermion Doubling

It is important to remember that the form of the lattice action is not unique: the naive fermion action in (2.31) is the simplest gauge invariant choice. However this choice results in a lattice model with extra low energy modes which need to be eliminated in order to obtain the correct continuum limit.

In order to show how these extra fermion species arise, we write eq.(2.31) in a more compact notation as

$$S_F = \sum_{n,m} \bar{\psi}(n) M_{nm} \psi(m), \tag{2.32}$$

where M is the fermion matrix, whose inverse gives the fermion propagator S. In particular, the free field propagator can be calculated in momentum space by Fourier transformations

$$M_{nm} = \int_{-\pi}^{\pi} \frac{d^4p}{(2\pi)^4} S^{-1}(p) e^{ip(n-m)} \tag{2.33}$$

with

$$S^{-1}(p) = \frac{i}{a}\sum_{\mu}\gamma_\mu \sin(ap\mu) + m. \tag{2.34}$$

The naive free fermion propagator is then

$$S(p) = \frac{m - i\sum_\mu \gamma_\mu \sin(ap_\mu)/a}{m^2 + \sin^2(ap_\mu)/a^2}, \tag{2.35}$$

which reduces to

$$S(p) = \frac{m - i\gamma_\mu p_\mu}{m^2 + p_\mu^2} + \mathcal{O}(a^2) \tag{2.36}$$

in the continuum limit $a \to 0$. The continuum propagator has a pole at $p_4 = i\sqrt{m^2 + \mathbf{p}^2}$ corresponding to a Dirac particle, while the discretized propagator with $m = 0$ has a pole at each of the sixteen corners of the 4-dimensional Brillouin zone, $-\pi < ap_\mu < \pi$, all giving $\sin(ap_\mu)/a = 0$. In d space-time dimensions there will be 2^d species of fermions. This is known as the *doubling problem*.

The two most popular schemes for eliminating these extra fermions have been proposed by Wilson [1] and Kogut and Susskind [4], and are briefly described in the following two sections.

2.5.2 Wilson Fermions

Since one has the freedom to add an arbitrary number of irrelevant operators to the action, as these do not change the continuum limit, Wilson proposed to add a second-derivative-like term to the naive fermion action:

$$\bar{\psi}(n)\frac{ar}{2}\partial_\mu^2\psi(n), \tag{2.37}$$

where r is called the Wilson parameter and the 4-dimensional lattice Laplacian is defined as

$$\partial_\mu^2\psi(n) = \frac{1}{a^2}[U_\mu(n)\psi(n+\mu) + U_\mu^\dagger(n-\mu)\psi(n-\mu) - 2\psi(n)]. \tag{2.38}$$

The effect of this term is to modify the mass m in the propagator in momentum space by

$$m + \frac{r}{a}\sum_{\mu}(1 - \cos(ap_{\mu})), \tag{2.39}$$

and this new mass term will diverge near the edges of the Brillouin zone as $a \to 0$. In practice, the result is to raise the masses of the unwanted fermions to values above the order of the cutoff, $1/a$, so that they become infinitely heavy in the continuum limit and decouple from the continuum physics, or in other words, will not appear in the dynamics of the continuum theory. Unfortunately this removal of the doublers comes at the expense of the chiral symmetry which is now explicitly broken even at $m = 0$.

This is a very general problem. In fact the so called no-go theorem by Nielson and Ninomiya [5] shows that it is impossible to define a local hermitian lattice theory which has no doublers and at the same time is chirally symmetric. In section 2.6, after reviewing the idea of chiral symmetry, we will discuss how this can be recovered on the lattice. But first, we discuss briefly another very popular approach to the doubling problem.

2.5.3 Staggered Fermions

Another commonly used method to deal with the fermion doubling problem is the one proposed by Kogut-Susskind, known as staggered fermion formalism. This essentially consists in interpreting the additional fermions as different degrees of freedom and eliminating them through spin-diagonalization. In practice, a local change of the fermionic variables is performed,

$$\psi(n) = T_n \chi(n), \qquad \bar{\psi}(n) = \bar{\chi}(n) T_n^{\dagger}, \tag{2.40}$$

where

$$T_n = \gamma_0^{n_0}\gamma_1^{n_1}\gamma_2^{n_2}\gamma_3^{n_3} \tag{2.41}$$

is a 4 × 4 unitary matrix diagonalizing all the γ matrices in such a way that

$$T_n^\dagger \gamma_\mu T_{n+\mu} = \eta_\mu(n)\mathbb{I}. \tag{2.42}$$

The phase factors $\eta_\mu(n)$ satisfy

$$\eta_\mu(n) = (-1)^{n_1+\ldots+n_{\mu-1}}, \qquad \eta_1(n) = 1. \tag{2.43}$$

The action written in terms of $\chi(n)$ and $\bar{\chi}(n)$ is diagonal in the spinor space. Although χ is a 4-component spinor, all components interact independently and identically, i.e. they are decoupled, so we can reduce the multiplicity of naive fermions by a factor of four simply by discarding all but one Dirac component of χ. The resulting one-component field is the staggered fermion field. The residual 'doublers' degrees of freedom are called 'tastes': a single staggered fermion corresponds to four tastes of continuum fermions in the 4-dimensional theory. In order to simulate such a single quark, the quark determinant that appears in the path integral (see eq.(2.83)) is replaced by a fourth root.

Let us notice that the one-component action for staggered fermions is invariant under a modified $U(1)$ chiral transformation: this remnant chiral symmetry is the reason why staggered fermions are preferred over Wilson ones when the chiral properties of the fermions dominate the dynamics, and they can be used to study the spontaneous breakdown of the remaining lattice symmetry $U(1) \times U(1)$. Otherwise Wilson fermions may be preferred due to their correspondence with Dirac fermions in terms of spin and flavour [6].

2.6 Chiral Symmetry

The fermionic field ψ can always be decomposed into 'left'- and 'right'-handed parts as follows:

$$\psi = \psi_R + \psi_L. \tag{2.44}$$

The projection operators $P_{R,L} = \frac{1}{2}(1 \pm \gamma_5)$, $P_{R,L}^2 = P_{R,L}$, where $\gamma_5 = i\gamma_0\gamma_1\gamma_2\gamma_3$, project out left- and right-handed field states,

$$\begin{aligned} \psi_R &= P_R\psi, \quad & \psi_L &= P_L\psi, \\ \bar{\psi}_R &= \bar{\psi}P_L, \quad & \bar{\psi}_L &= \bar{\psi}P_R. \end{aligned} \tag{2.45}$$

Chiral symmetry is the symmetry associated with the independent transformations of the left- and right-handed chiral states of a particle. Therefore, for N_f quark flavours, QCD possesses chiral symmetry if the QCD Lagrangian is invariant under separate transformations of the left- and right-handed chiral fields, or in other words, possesses a $SU(N_f)_L \times SU(N_f)_R$ symmetry. This is equivalent to the $SU(N_f)_V \times SU(N_f)_A$ symmetry, under the vector and axial transformations

$$SU(N_f)_V: \quad \psi \to e^{i\theta}\psi \qquad \bar{\psi} \to \bar{\psi}e^{-i\theta} \tag{2.46}$$

$$SU(N_f)_A: \quad \psi \to e^{i\gamma_5\theta}\psi \qquad \bar{\psi} \to \bar{\psi}e^{i\gamma_5\theta}, \tag{2.47}$$

where θ can be written as $\theta_a\tau_a$, with τ_a the generators of flavour $SU(N_f)$. These two transformations are associated with the conservation of the vector and axial current respectively, $J_\mu(x) = \bar{\psi}(x)\gamma_\mu\theta\psi(x)$ and $J_{\mu 5}(x) = \bar{\psi}(x)\gamma_\mu\gamma_5\theta\psi(x)$. For non-vanishing quark mass, the axial current is not conserved, and this symmetry is explicitly broken from $SU(N_f)_V \times SU(N_f)_A$ to $SU(N_f)_V$. This is why the chiral symmetry is often referred as γ_5 symmetry. Associated with this broken symmetry are $(N_f^2 - 1)$ Goldstone bosons, i.e. the non-zero mass of the pions.

2.6.1 Chiral Symmetry on the Lattice

In order for the fermionic lattice action to be invariant under the transformation $\psi \rightarrow e^{i\gamma_5\theta}\psi$, $\bar{\psi} \rightarrow \bar{\psi}e^{i\gamma_5\theta}$, the lattice Dirac operator D, i.e. the fermionic matrix in eq.(2.32) in the massless limit, has to satisfy

$$\gamma_5 \not{D} \gamma_5 = \not{D}^\dagger. \tag{2.48}$$

The naive fermion action (2.31) for $m = 0$ is clearly chiral invariant since the Dirac operator was defined by simply taking the symmetric difference for the derivative. However, introducing for example the Wilson term in order to solve the doubling problem, spoils this symmetry, even for zero mass[5].

As we already mentioned, this is a general problem, validated in the Nielsen-Ninomiya theorem [5]. However chiral symmetry can be recovered on the lattice without doublers if we only require that the Dirac operator satisfies the Ginsparg-Wilson [7] relation (GW)

$$\gamma_5 \not{D} + \not{D} \gamma_5 = \{\gamma_5, \not{D}\} = a \not{D} \gamma_5 \not{D}. \tag{2.49}$$

This corresponds to the following field transformation

$$\psi \rightarrow e^{i\gamma_5\theta(1-\frac{a}{2}\not{D})}\psi, \;\; \bar{\psi} \rightarrow \bar{\psi}e^{i\theta(1-\frac{a}{2}\not{D})\gamma_5}, \tag{2.50}$$

so that for an infinitesimal transformation, $\theta << 1$, the massless fermion lattice Lagrangian $\mathcal{L} \sim \bar{\psi}\not{D}\psi$, with $\not{D}$ satisfying (2.49), will be invariant under such transformation. Provided one can find a Dirac operator satisfying the GW relation, it is then possible to construct a chiral theory without the presence of the fermion doublers.

---

[5] The Wilson term is $\sim \frac{1}{a}\bar{\psi}\psi$, analogous to a mass term $m\bar{\psi}\psi$.

Overlap fermions [8, 9] and *Domain Wall* fermions [10, 11, 12] are two closely related, but independently developed, formulations of the 'Ginsparg-Wilson' fermions. The overlap fermions have exact chiral symmetry even at finite lattice spacing and contain the correct flavour symmetry. We will describe the overlap operator in section 2.8 since it has been used in the D_s project (chapter 5). Domain Wall fermions (DWF) also preserve flavour symmetry and restore chiral symmetry by introducing an infinitely long fifth dimension. In practice this dimension is finite, but the residual chiral symmetry breaking is in any case smaller than the Wilson fermions case, for example, by a few orders of magnitude. As explained in next section, the only effect of this chiral symmetry breaking is an additive renormalization to the bare quark mass.

2.7 Domain Wall Fermions

Kaplan [10] first proposed the idea of reproducing the behaviour of massless chiral fermions in $2n$ dimensions from massive interacting fermions in $2n+1$ dimensions. This formulation introduces an extra space-time dimension, usually denoted with s with length L_s. In the case of QCD, this means formulating the chiral four-dimensional theory by constructing a five-dimensional theory with massive fermions[6]. In the fifth dimension the mass term has the shape of a step function:

$$m(s) = \begin{cases} M_5 & s > 0 \\ 0 & s = 0 \\ -M_5 & s < 0. \end{cases} \qquad (2.51)$$

Such a mass defines a domain wall separating the two half-spaces $s > 0$ and $s < 0$ from each other. If the fifth dimension is infinite, there is a single chiral

---

[6] Note that the extra dimension contains only fermion fields: the gauge fields remain four-dimensional.

fermion on the four dimensional boundary. But for a finite L_s on a lattice with $0 \leq s \leq L_s - 1$, if a domain wall is located at $s = 0$, there will necessarily be a second wall, an "anti-domain wall", on the other boundary, $s = L_s - 1$: the zero-modes of opposite chirality are bound to the opposite walls and their overlap will exponentally decrease. Therefore, while in the infinite-length limit for the fifth dimension, exact chiral symmetry is restored, for finite values of L_s these two states mix between the walls, with consequent chiral symmetry breaking. However, their mixing, and the chiral violation, is exponentially suppressed with the size of the fifth dimension, i.e. $\mathcal{O}(exp(-\alpha L_s)/a)$.

2.7.1 DWF Operator

The formalism generally used to describe DWF is the one developed by Furman and Shamir [12]. Following their conventions, we denote the coordinates in the usual four dimensions as x, while the $s = 0, 1, ..., L_s - 1$ is the coordinate of the fifth direction, with L_s assumed to be even. The DWF operator acts on a five-dimensional fermion field denoted as $\Psi(x, s)$, while the four-dimensional fermion field is still denoted $\psi(x)$. The domain wall fermion action is then given by:

$$S_F^{DW} = \sum_{x,x';s,s'} \bar{\Psi}(x,s) D_{x,s;x',s'} \Psi(x',s'), \tag{2.52}$$

with the DWF Dirac operator defined as

$$D_{x,s;x',s'} = \delta_{s,s'} D^{||}_{x,x'} + \delta_{x,x'} D^{\perp}_{s,s'}. \tag{2.53}$$

The $D^{\|}_{x,x'}$ part has the form of a Wilson action with modified mass term[7]:

$$\begin{aligned} D^{\|}_{x,x'} &= \frac{1}{2}\sum_{\mu=1}^{4}[(1-\gamma_\mu)U_\mu(x)\delta_{x+\hat{\mu},x'} + (1+\gamma_\mu)U^\dagger_\mu(x')\delta_{x-\hat{\mu},x'}] \\ &+ (M_5-4)\delta_{x,x'}. \end{aligned} \tag{2.54}$$

M_5 is sometimes referred as the *domain wall height.* The gauge field is replicated along the s direction, so that each four-dimensional slice in the fifth dimension has identical gauge fields (see figure 2.3). The $D^{\perp}_{s,s'}$ term instead describes the propagation in the fifth dimension. It can be thought of as describing the coupling between the five dimensional slices:

$$\begin{aligned} D^{\perp}_{s,s'} &= \frac{1}{2}[(1-\gamma_5)\delta_{s+1,s'} + (1+\gamma_5)\delta_{s-1,s'} - 2\delta_{s,s'}] \\ &- \frac{m_f}{2}[(1-\gamma_5)\delta_{s,L_s-1}\delta_{0,s'} + (1+\gamma_5)\delta_{s,0}\delta_{L_s-1,s'}]. \end{aligned} \tag{2.55}$$

m_f is the input bare quark mass and directly couples the two domain walls at $s = 0$ and $s = L_s - 1$.

The four dimensional fermionic fields, $\psi(x)$, are constructed from the five dimensional ones, $\Psi(x, s)$, by projection of the different chiralities on the walls [12]

$$\begin{aligned} \psi(x) &= P_L\Psi(x,0) + P_R\Psi(x,L_s-1) \\ \bar{\psi}(x) &= \bar{\Psi}(x,L_s-1)P_L + \bar{\Psi}(x,0)P_R, \end{aligned} \tag{2.56}$$

where $P_{R,L}$ are the projection operators defined in section 2.6.

2.7.2 Residual Chiral Symmetry Breaking

The discretization of the action seen in the previous section, leads to one left-handed fermion mode localised on the left boundary of the fifth dimension, and one right-handed fermion mode on the right boundary: their wave functions decay

---

[7] Note that the modified mass makes the modes heavy and suppresses their propagation along the 4-d slices.

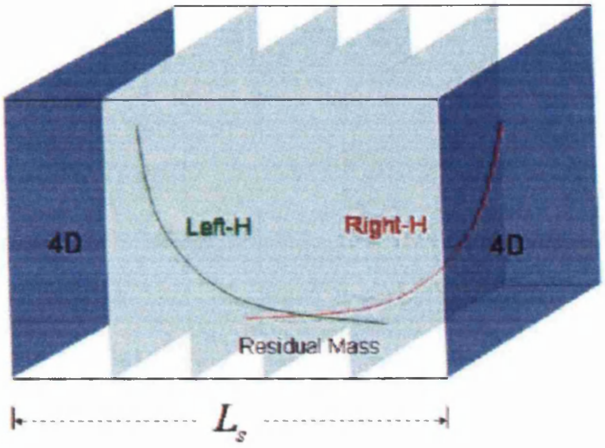

Figure 2.3: Schematic illustration of the domain wall fermion formulation. The massless chiral states fall off the walls exponentially. The light blue slices give an idea of how the gauge fields are replicated along the fifth direction.

exponentially in the fifth dimension and, for finite separation between the two boundary walls, they overlap in the middle of the fifth dimension. We see now how to quantify the size of the consequent symmetry breaking.

The chiral transformation is defined to rotate the fermions in the two halves of the fifth dimension[8]:

$$\begin{aligned} \delta\Psi(x,s) &= i\epsilon(s)\tau^a\Psi(x,s) \\ \delta\bar{\Psi}(x,s) &= -i\epsilon(s)\tau^a\bar{\Psi}(x,s) \end{aligned} \tag{2.57}$$

where

$$\epsilon(s) = \begin{cases} 1, & 0 \leq s < L_s/2 \\ -1, & L_s/2 \leq s \leq L_s - 1. \end{cases} \tag{2.58}$$

---

[8] Eq.(2.57) corresponds to the usual chiral transformation for the four-dimensional quark fields, $\delta^a\psi(x) = i\tau^a\gamma_5\psi(x)$, $\delta^a\bar{\psi}(x) = \bar{\psi}(x)i\tau^a\gamma_5$.

The axial current generated by this transformation is

$$\mathcal{A}^a_\mu = \sum_{s=0}^{L_s-1} sign(s - \frac{L_s - 1}{2}) j^a_\mu(x,s), \tag{2.59}$$

where

$$\begin{aligned} j^a_\mu(x,s) &= \frac{1}{2}[\bar{\Psi}(x+\hat{\mu},s)(1+\gamma_\mu)U^\dagger_\mu(x+\hat{\mu})\tau^a\Psi(x,s) \\ &- \bar{\Psi}(x,s)(1-\gamma_\mu)U_\mu(x)\tau^a\Psi(x+\hat{\mu},s)]. \end{aligned} \tag{2.60}$$

The divergence of this current satisfies

$$\Delta_\mu \mathcal{A}^a_\mu = 2m_f J^a_5(x) + 2J^a_{5\psi}(x), \tag{2.61}$$

where $\Delta_\mu f(x) = f(x) - f(x - \hat{\mu})$ is a finite difference operator and $J^a_5(x)$ is the pseudoscalar density, written in terms of Ψ and $\bar{\Psi}$ as

$$\begin{aligned} J^a_5(x) &= -\bar{\Psi}(x, L_s - 1)P_L\tau^a\Psi(x,0) + \bar{\Psi}(x,0)P_R\tau^a\Psi(x, L_s - 1) \\ &= \bar{\psi}(x)\tau^a\gamma_5\psi(x). \end{aligned} \tag{2.62}$$

Equation (2.61) differs from the corresponding continuum expression by the term $J^a_{5\psi}$, referred as the "mid-point" operator, built from fermion fields in the middle of the fifth dimension and given by

$$\begin{aligned} J^a_{5\psi}(x) = &- \bar{\Psi}(x, L_s/2 - 1)P_L\tau^a\Psi(x, L_s/2) \\ &+ \bar{\Psi}(x, L_s/2)P_R\tau^a\Psi(x, L_s/2 - 1). \end{aligned} \tag{2.63}$$

This mid-point term adds an additional term to the axial Ward identity for DWF [12] which can be written then as

$$\Delta_\mu < \mathcal{A}^a_\mu(x)O(y) >= 2m_f < J^a_5(x)O(y) > +2 < J^a_{5\psi}(x)O(y) > +i < \delta^a O(y) > . \tag{2.64}$$

The mid-point term in eq.(2.64), which vanishes when $L_s \to \infty$ [12], represents the contributions of finite L_s effects on the low-energy physics of domain wall fermions. Since in the continuum limit eq.(2.64) must agree with the corresponding identity in the effective continuum theory, the sum of the first two terms must be equivalent to an effective quark mass, $m_{eff} = m_f + m_{res}$, times the pseudoscalar density $J_5^a(x)$:

$$J_{5\psi}^a(x) = m_{res} J_5^a(x) + \mathcal{O}(a). \tag{2.65}$$

An especially important case is when the operator is itself a pseudoscalar density, $O(y) = J_5^a(y)$. In this case, close to the continuum limit, eq.(2.64) becomes

$$\Delta_\mu < \mathcal{A}_\mu^a(x) J_5^a(y) >= 2(m_f + m_{res}) < J_5^a(x) J_5^a(y) > . \tag{2.66}$$

So the pseudoscalar meson masses vanish for $m_f + m_{res} = 0$, i.e. the chiral limit for domain wall fermions is defined at $m_f = -m_{res}$, instead of $m_f = 0$ as in the continuum limit. In other words, the effect of the violation in chiral symmetry is to shift the four dimensional bare quark mass, m_f, by some small additive piece m_{res}, the residual or anomalous mass. In practice the residual mass term is computed by means of the ratio [13]

$$R(t) = \frac{< \sum_x J_{5\psi}^a(\mathbf{x}, t) J_5^a(\mathbf{0}, 0) >}{< \sum_x J_5^a(\mathbf{x}, t) J_5^a(\mathbf{0}, 0) >}, \tag{2.67}$$

and for sufficiently large t, where the effects of low-energy long-distance physics are dominant, $J_{5\psi}^a$ behaves as eq.(2.65) and $R(t)$ represents m_{res}.

2.8 Overlap Operator

A possible operator that satisfies eq.(2.49) was proposed by Neuberger [9] after a long time since Ginsparg and Wilson suggested the relaxation of the chirality condition as a way around the no-go theorem. Writing the operator as

$$a\not{D}_o = 1 + \gamma_5 V, \tag{2.68}$$

without loss of generality, the search for D_o is algebraically equivalent to a search for a unitary, hermitian operator V. In fact, the hermiticity of V, $V = V^\dagger$, comes from requiring the γ_5 hermiticity of $\not{D}_o$ itself, eq.(2.48), while its unitarity comes by multiplying the GW relation on the left by γ_5

$$\not{D}_0 + \not{D}_0^\dagger = a\not{D}_0^\dagger \not{D}_0, \tag{2.69}$$

so that

$$\begin{aligned}
\frac{1}{a}(1+\gamma_5 V) + \frac{1}{a}(1+V^\dagger\gamma_5) &= \frac{a}{a^2}(1+V^\dagger\gamma_5)(1+\gamma_5 V) && (2.70)\\
2+\gamma_5 V + V\gamma_5 &= 1+\gamma_5 V + V\gamma_5 + V^2 && (2.71)\\
\Rightarrow V^2 &= 1. && (2.72)
\end{aligned}$$

The expression proposed by Neuberger for V can be written as

$$V = \frac{\gamma_5 D_W(\rho)}{\sqrt{D_W(\rho)^\dagger D_W(\rho)}}, \tag{2.73}$$

where $D_W(\rho)$ is the usual Wilson fermion operator[9] with a negative mass parameter, $D_W(\rho) = D_W(0) - \rho/a$ with $0 < \rho < 2$. The reason why we get exactly massless quarks is that no fine tuning is needed for V to have eigenvalues very close to -1. Note that $D_W(0)$ may have near zero eigenvalues, causing problems when inverting the matrix. This is why the additive mass parameter ρ is present: it does not affect the continuum limit since, as showed below, we only require the

---

[9] In general, it can be any valid lattice Dirac operator: it needs to be γ_5-hermitian in order for V to be unitary and hermitian.

sign of the D_W eigenvalues. In fact, substituting V into eq.(2.68)

$$\begin{aligned} a\not{D}_o &= 1+\frac{D_W(\rho)}{\sqrt{D_W(\rho)^\dagger D_W(\rho)}} && (2.74)\\ &= 1+\gamma_5\frac{\gamma_5 D_W(\rho)}{\sqrt{[\gamma_5 D_W(\rho)]^\dagger[\gamma_5 D_W(\rho)]}} && (2.75)\\ &= 1+\gamma_5\frac{\gamma_5 D_W(\rho)}{\sqrt{[\gamma_5 D_W(\rho)]^2}}, && (2.76)\end{aligned}$$

where we used that $H = \gamma_5 D_W(\rho)$ is hermitian. This expression can be written as

$$a\not{D}_o = 1+\gamma_5 sgn(H), \qquad (2.77)$$

where $sgn(H) = H/\sqrt{H^2}$ is the matrix sgn function of H. For the massive case, this gives[10]

$$a\not{D}_o(m_q,\rho) = \rho(1+\frac{am_q}{2\rho}) + \rho(1-\frac{am_q}{2\rho})\gamma_5 sgn(H) \qquad (2.78)$$

which is sometimes written as

$$a\not{D}_o(\mu) = \rho(1+\mu) + \rho(1-\mu)\gamma_5 sgn(H), \qquad (2.79)$$

where $\mu = \frac{am_q}{2\rho}$. This is the form of the overlap operator used in chapter 5 to simulate the charm valence quark.

The overlap fermions, despite their high cost, have very desiderable features, significant for both light and heavy fermions [75]. Apart from the essential feature of allowing an exact chiral symmetry on the lattice, in numerical simulations with overlap fermions there is no additive quark mass renormalization, no exceptional configurations and no flavour symmetry breaking. Not only they are free from $\mathcal{O}(a)$ and $\mathcal{O}(am)$ errors, but the $\mathcal{O}(a^2m^2)$ and $\mathcal{O}(\Lambda_{QCD}a^2m)$ errors are apparently small (see [75] for an in depth discussion and references).

---

[10] Note the factor ρ is a rescaling factor in order to have the correct continuum limit.

2.9 Monte Carlo Integration

As mentioned in section 2.1, the starting point for any calculation of hadron masses and matrix elements in lattice QCD is the path integral

$$\langle \mathcal{O} \rangle = \frac{1}{\mathcal{Z}} \int \prod_f \mathcal{D}U \mathcal{D}\psi_f \mathcal{D}\bar{\psi}_f \mathcal{O} e^{-S_{LQCD}[U,\psi,\bar{\psi}]} \tag{2.80}$$

with the partition function given by

$$\mathcal{Z} = \int \prod_f \mathcal{D}U \mathcal{D}\psi_f \mathcal{D}\bar{\psi}_f e^{-S_{LQCD}[U,\psi,\bar{\psi}]}, \tag{2.81}$$

and the QCD lattice action composed of both fermionic and gauge actions,

$$S_{LQCD}[U,\psi,\bar{\psi}] = S_F[U,\psi,\bar{\psi}] + S_G[U]. \tag{2.82}$$

The fermionic piece S_F is bilinear in the quark fields, so we can integrate out the fermionic degrees of freedom by applying the Grassman algebra (see Appendix B) and obtain a determinant of the fermionic matrix for each flavour

$$\langle \mathcal{O} \rangle = \frac{1}{\mathcal{Z}} \int \prod_f \mathcal{D}U det(M^f[U]) \mathcal{O} e^{-S_G[U]}. \tag{2.83}$$

The fermionic contribution is now contained in the highly non-local determinant and the integration is only on the gauge degrees of freedom. The direct computation of the fermionic determinant is numerically very expensive. This is why for a long time the so called "quenched approximation" played a central role in lattice calculations: it consists of setting the determinant in the integral equal to one. In perturbation theory, it is equivalent to turning off vacuum polarization effects of quark loops, which is unphysical and can introduce uncontrollable systematic errors. However, since quenched QCD differs from full QCD only in the weighting of the background gauge configurations, it was considered reasonable to perform quenched simulations in order to understand and control other sources of errors. Fortunately today the advent of powerful computers together with the improvement of the algorithms allow dynamical simulations to be performed. We now briefly describe how this works.

The number of integration variables in the integral (2.83) is normally extremely large, so generating the gauge configurations would be computationally extremely demanding[11]: this is why statistical methods must be used to evaluate such quantities. Monte Carlo techniques can be used to generate a sample of gauge configurations with probability distribution $e^{-S_G[U]}$. Note also that the probability distribution of the gauge configurations is highly peaked at the classical minimum of the action, so that the functional integral (2.83) is dominated by those configurations around the peak: this is why one can generated a sequence of N *importance-sampled* gauge configurations according to the probability distribution given by

$$P[U] = \frac{1}{\mathcal{Z}} e^{-S_G[U_i]} \prod_f det(M^f[U_i]). \tag{2.84}$$

Therefore the expectation value of an observable $\mathcal{O}$ becomes an ensemble average over N gauge configurations

$$\langle \mathcal{O} \rangle \sim \frac{1}{N} \sum_{i=1}^{N} \mathcal{O}[U_i], \tag{2.85}$$

where the sum is now over the gauge configurations appropriately weighted as explained above.

Numerical algorithms generate a sequence of configurations known as Markov chain such that the C_{i+1} element is generated from the C_i one stochastically ac-

---

[11] For instance, in a $16^3 \times 32$ lattice, the number of links U is $4 \times 16^3 \times 32$, and since they are $SU(3)$ matrices, it corresponds to a total of $8 \times 4 \times 16^3 \times 32 = 4194304$ integrations. Furthermore, if each integration is approximated by n points, the number of terms to be calculated is $n^{4194304}$.

cording to some transition probability. The chain will converge to the desired probability distribution if it satisfies the two important conditions of detailed balance and ergodicity. Details of the Markov Chain Monte Carlo (MCMC) methods and different algorithms used can be found in literature: [14, 15, 16] are some examples. Here we just remark the fact that in the generation of the gauge configurations there is some amount of simulation, or Monte Carlo, time before the system reaches the equilibrium. When this happens, we say that the system is thermalized. The number of measurements required for thermalization depends on the observable considered or on the algorithm used for instance. In order to find this number, the plot of some observable (typically the Polyakov loop or the plaquette) versus the Monte Carlo time is considered: the thermalization typically starts at the onset of the plateau. The thermalized configurations are then the ones used to measure the observables of interest.

In this work the RHMC algorithm and its recent improved versions have been used [17, 18, 19, 20].

2.10 Autocorrelation

The fact that the gauge configurations are generated in a Markov chain as explained in the previous section, gives rise to correlations between the configurations in the molecular simulation time, known as *autocorrelations.* The autocorrelation function between two measurements of some observable $\mathcal{O}$, separated by t molecular dynamics time units, is defined as

$$\rho(t) = \sum_{i=1}^{N} (\mathcal{O}_i - \bar{\mathcal{O}})(\mathcal{O}_{i+t} - \bar{\mathcal{O}}), \tag{2.86}$$

where $\bar{\mathcal{O}}$ is the average over the N measurements which, for $N \to \infty$, gives the vacuum expectation value $\langle \mathcal{O} \rangle$, as defined in eq.(2.85). In order to measure the statistical dependence between gauge configurations, the integrated autocorrelation time is defined as[12]

$$\tau_{int} = \frac{1}{2} \sum_{t=-\infty}^{\infty} \frac{\rho(t)}{\rho(0)} = \frac{1}{2} + \sum_{t=1}^{\infty} \frac{\rho(t)}{\rho(0)}. \tag{2.87}$$

In practice, the sum in the equation above is truncated at some t_{max}: for values of t large enough, $t > t_{max}$, the measurements are sufficiently independent and $\rho(t)$ becomes a random noise. Typically two measurements which are separated by $2\tau_{int}$ in the molecular dynamics time can be considered statistically independent. The standard way to deal with autocorrelations is to bin the data into blocks of length b equal or bigger than $2\tau_{int}$, and then from the blocked (or binned) data, carry out the analysis described in the following sections. Of course an important test is investigating possible variations in the final results as b is changed.

2.11 Correlation Functions

In order to calculate observables, hadron masses for instance, and test our theory against physical values obtained by experiments, we can use *correlation functions*, or correlators, constructed from interpolating quantum field operators whose form depends on the particular observable one wants to compute. In the previous section we saw how the expectation value of some observable can be estimated by an average over an ensemble of gauge configurations. In particular, the two point correlation functions are defined to be the vacuum expectation value of the time

---

[12] Note that $\rho(-t) = \rho(t)$.

ordered product of two interpolating operators at two times,

$$\begin{aligned} C_{AB}(\vec{x},t;\vec{0},0) &= \frac{1}{Z}\int \mathcal{D}U\mathcal{D}\psi\mathcal{D}\bar{\psi} O_A(\vec{x},t)O_B^\dagger(\vec{0},0)e^{-S_{LQCD}} \\ &= \langle 0|\hat{T}\{O_A(\vec{x},t)O_B^\dagger(\vec{0},0)\}|0\rangle \\ &= \langle 0|O_A(\vec{x},t)O_B^\dagger(\vec{0},0)|0\rangle, \end{aligned} \tag{2.88}$$

where $O_B^\dagger(\vec{0},0)$ creates a hadron at the source location $(\vec{0},0)$ and $O_A(\vec{x},t)$ destroys the hadron at the sink $(\vec{x},t)$. In momentum space eq.(2.88) becomes

$$C_{AB}(\vec{p},t;\vec{0},0) = \sum_{\vec{x}} \langle 0|O_A(\vec{x},t)O_B^\dagger(\vec{0},0)|0\rangle e^{-i\vec{p}\cdot\vec{x}}. \tag{2.89}$$

Expecially when we want to determine hadron masses from the lattice, the correlators are usually projected to zero momentum. The two-point correlator can then be written as

$$C_{AB}(t) = \sum_{\vec{x}} \langle 0|O_A(\vec{x},t)O_B^\dagger(\vec{0},0)|0\rangle. \tag{2.90}$$

If we insert a complete set of energy eigenstates of the Hamiltonian and consider that $O_i(t)$ evolves as $e^{Ht}O_ie^{-Ht}$, eq.(2.90) becomes

$$C_{AB}(t) = \sum_n \frac{\langle 0|O_A|n\rangle\langle n|O_B^\dagger|0\rangle e^{-m_n t}}{2m_n}, \tag{2.91}$$

where the normalization $\langle n|n'\rangle = 2m_n\delta_{n,n'}$ is used[13]. In the limit of large time the correlation function is dominated by the lowest states. In particular, the ground state mass of the particle m_0 can be extracted from the large time limit

$$\lim_{t\to\infty} C_{AB}(t) \to \mathcal{A}_{AB}^0 e^{-m_0 t} \tag{2.93}$$

---

[13] Note the special case of a diagonal correlator, i.e. $A = B$, gives

$$C(t) = \sum_n \frac{|\langle 0|O|n\rangle|^2 e^{-m_n t}}{2m_n}. \tag{2.92}$$

where $\mathcal{A}^0_{AB} = \frac{\langle 0|O_A|0\rangle\langle 0|O^\dagger_B|0\rangle}{2m_0}$. Due to the finite time extent of the lattice, the hadron correlators will also receive contributions from the backward propagating state, so that the function to be fitted will actually differ from (2.93) and will depend on the particular hadron state. We will see examples in next two sections.

2.11.1 Meson Correlation Functions

For meson correlators, the operator $O_i = O_M$ takes the form of

$$O_M(x) = \bar{\psi}_i(x)\Gamma\psi_j(x), \tag{2.94}$$

where Γ is some combination of the γ matrices which will give the spin and parity properties of the meson state to be studied. Since there is no unique correspondence between particle states and operators, the request is that the operator has the same flavour content and same J^{PC} as the state in question, where J is the total angular moment and P and C are the parity and charge conjugation quantum numbers. Table 2.1 shows the mapping of the Γ operators to the corresponding meson states.

Written in terms of the quark fields, the meson correlator is

$$C_M(t) = \sum_{\vec{x}} \langle \bar{\psi}^\alpha_i(x)\Gamma^{\alpha\beta}\psi^\beta_j(x)\bar{\psi}^\gamma_j(0)\Gamma^{\gamma\delta\dagger}\psi^\gamma_i(0)\rangle. \tag{2.95}$$

By performing Wick contractions of the Grassmann quark fields, the correlators can be reduced to products of quark propagators. If the propagator is given by $\langle\psi^\alpha_i(x)\bar{\psi}^\beta_j(0)\rangle = G^{\alpha\beta}_{ij}(x;0)$, neglecting the disconnected part present for flavour singlet mesons, eq.(2.95) becomes

$$C_M(t) = -\sum_{\vec{x}} \langle Tr[G(0,x)\Gamma G(x,0)\Gamma^\dagger]\rangle, \tag{2.96}$$

where the trace runs over spin and colour indices which have been dropped for simplicity. The evaluation of this term means computing two point-to-all propagators: the γ_5-hermiticity of the Dirac operator can be used though and the two propagators can be related to each other,

$$G(0,x) = \gamma_5 G^\dagger(x,0)\gamma_5. \tag{2.97}$$

Equation (2.96) becomes

$$C_M(t) = -\sum_{\vec{x}} \langle Tr[\gamma_5 G^\dagger(x,0)\gamma_5 \Gamma G(x,0)\Gamma^\dagger]\rangle_U, \tag{2.98}$$

where $\langle\rangle_U$ reminds us of the integration over the gauge fields U (see section 2.9). Therefore only one inversion of the fermionic matrix per configuration is required in the degenerate quark case. In the flavour-singlet case, there will be another term in (2.96) which requires the computations of all-to-all propagators, i.e. $G(x;x) = G(x,t;x,t)$, considerably more difficult and computationally more expensive, therefore neglected in most calculations.

Recalling eq.(2.93) and how the ground state mass is extracted, the backward propagating state needs to be included. So the two point function for large time is properly given by

$$\lim_{t\to\infty} C_{AB}(t) \to \mathcal{A}^0_{AB}[e^{-m_0 t} + \eta e^{-m_0(T-t)}], \tag{2.99}$$

where $T = N_t$ is the extent of the lattice in the time direction and the factor η depends on the time reversal symmetry of the operators. For instance, the pseudoscalar meson state for degenerate operators will have $\eta = 1$ and

$$C(t) \to 2\mathcal{A}^0 e^{-m_0 T/2}\cosh[m_0(\frac{T}{2} - t)]. \tag{2.100}$$

Bilinear	Γ	J^{PC}	Example
Scalar	$\mathbb{I}$, γ_4	0^{++}	f_0 or σ
Pseudoscalar	$\gamma_5, \gamma_4\gamma_5$	0^{-+}	π, K
Vector	$\gamma_i, \gamma_i\gamma_4$	1^{--}	ρ
Axial vector	$\gamma_i\gamma_5$	1^{++}	a_1
Tensor	$\gamma_i\gamma_j(\sigma_{ij})$	1^{+-}	b_1

Table 2.1: Meson states created by the quark bilinear interpolating operators $\bar{\psi}\Gamma\psi$.

2.11.2 Baryon Correlation Functions

For baryons, the standard interpolating operator is composed of a local diquark operator and a spectator-like quark field:

$$O_{B,k,\delta}(x) = \epsilon_{abc}\epsilon^{ij}[\psi^{T,a}_{i,\alpha}(x)C\Gamma^{\alpha\beta}\psi^{b}_{j,\beta}(x)]\psi^{c}_{k,\delta}(x), \tag{2.101}$$

where Γ is again one of the possible 16 Dirac matrices and $C = \gamma_4\gamma_2$[14] is the charge conjugation operator. The superscript T denotes transpose and abc, ijk and $\alpha\beta\delta$ are colour, flavour and Dirac indices respectively. Note the totally antisymmetric tensor ϵ^{ij} on two indices ($\epsilon^{11} = \epsilon^{22} = 0$, $\epsilon^{12} = 1$ and $\epsilon^{21} = -1$) ensures the operators have the correct flavour content. This baryon operator is colour singlet and has one free spinor index necessary for describing spin-$\frac{1}{2}$ octet and spin-$\frac{3}{2}$ decuplet baryons. More details will be given in chapter 4. In particular in this work (chapter 4) we will deal with nucleons. The operators corresponding to the

---

[14] Note

$$\begin{aligned} C^{\dagger} = C^{-1} &= C^{T} = -C \\ C\gamma_{\mu}C^{-1} &= -\gamma_{\mu}^{T}. \end{aligned}$$

nucleon (proton) state are

$$\begin{aligned} N_{1,\alpha}(x) &= \epsilon_{abc}(u^{T,a}(x)\mathcal{C}\gamma_5 d^b(x))u^c_\alpha(x) \\ N_{2,\alpha}(x) &= \epsilon_{abc}(u^{T,a}(x)\mathcal{C}\gamma_4\gamma_5 d^b(x))u^c_\alpha(x), \end{aligned} \tag{2.102}$$

where u and d nominally indicate the up and down quark respectively. Note that a combination of these two operators can also be considered. Also, the baryon operators do not have a definite parity. They couple to both the negative and positive parity states, transforming under parity as

$$\mathcal{P}O_{B,k,\delta}(x_4,\vec{x})\mathcal{P} = \gamma_4 O_{B,k,\delta}(x_4,-\vec{x}). \tag{2.103}$$

Since $\gamma_4 = diag(1,1,-1,-1)$, the two upper components of O_B transform with positive parity while the lower two transform with negative parity. In particular it turns out that the backward propagating state has an opposite parity to the forward propagating one. And since the masses of positive and negative parity states are not necessarily the same due to the spontaneously broken chiral symmetry, the projection operators $P_\pm = \frac{1}{2}(1 \pm \gamma_4)$ are used to project out positive and negative states. In general a baryon two-point correlator at time t, $C_N(t) = \sum_{\vec{x}}\langle N(t)N^\dagger(0)\rangle$, can be written as

$$\begin{aligned} C_N(t) = (1+\gamma_4)A_+e^{-m_+t} &\pm (1-\gamma_4)A_+e^{-m_+(T-t)} \\ &\mp(1+\gamma_4)A_-e^{-m_-(T-t)} - (1-\gamma_4)A_-e^{-m_-t}, \end{aligned} \tag{2.104}$$

where the subscripts indicate the parity of the corresponding state and the (lower) upper sign corresponds to choice of a finite lattice with (anti-) periodic boundary conditions. Projecting out the positive and negative parity states gives

$$\begin{aligned} C^+_N(t) &= Tr\{P_+C_N(t)\} = A_+e^{-m_+t} \mp A_-e^{-m_-(T-t)} \\ C^-_N(t) &= Tr\{P_-C_N(t)\} = -A_-e^{-m_-t} \pm A_+e^{-m_+(T-t)}. \end{aligned} \tag{2.105}$$

As we can see, there is no time reflection symmetry as in the meson case, since the forward and backward propagating states depend on different mass values.

The physical states represented by the operators (2.104) are not only the nucleons, $N(940)$, with $J^P = \frac{1}{2}^+$, but also the heavier state $N(1535)$, commonly known as N^*, parity partner of the nucleon, $J^P = \frac{1}{2}^-$. In order to find their corresponding masses, the positive and negative correlators (2.105) need to be fitted simultaneously. Note that contributions to the negative parity state come also from the interpolating operator (2.101) with $\Gamma = \mathbf{1}$, i.e. $\epsilon_{abc}(u^{T,a}(x)Cd^b(x))u^c_\alpha(x)$, while its corresponding positive parity operator has a poor overlap with the nucleon ground state. We will see more details in chapter 4. From now on we will indicate $m_+ = M_N$ and $m_- = M_{N^*}$.

2.11.3 Effective Masses

We just saw how the ground state masses can be extracted from the correlators. However it is not always easy setting t_{min} in the fitting range, $[t_{min}, t_{max}]$, high enough that the lowest mass dominates the correlation function and the contamination from higher mass states is not significant. A convenient way to proceed is to examine *effective mass* plots. The effective masses for mesons and baryons are defined as

$$\begin{aligned} m^M_{eff}(t) &= \cosh^{-1}[\frac{C(t+1)+C(t-1)}{2C(t)}], \\ m^B_{eff}(t) &= -\ln[\frac{C(t+1)}{C(t)}]. \end{aligned} \qquad (2.106)$$

A plot of these functions versus t should plateau where the lowest mass term dominates and the excited states have decayed away: looking at this kind of plots then gives an indication on the fitting range to extract the ground state mass.

2.11.4 Smearing

We saw that the main idea of creating mesons and baryons functions is to choose operators with a non-zero overlap with the state to be studied, i.e. with the correct quantum numbers J^{PC}. In some cases it can be necessary to improve the signal from the data, in particular when we want to extract ground state masses since we need to look at large Euclidean times, where the noise increases. In this case we may like to increase the ground state amplitude relative to the first excited state. A way of proceeding is using *smeared* operators at the source and/or the sink which cover an extended region of the lattice, instead of a local point, in order to obtain a better overlap with the desired state. Since in most cases the source is constructed on a single time-slice, it is computationally cheaper to perform source smearing than sink smearing. All the smearing in this work are at source, apart from the case when both sink and source are smeared. The smearing operators used are wall/box [21], hydrogen-like [22] and Gaussian [23] operators.

2.12 Fitting Methods

In section 2.11 we gave examples of model functions that parametrize the large time behaviour of mesonic and baryonic correlation functions. In general we need to fit the numerical data, in our case correlation functions, $C(t)$, to some known function model $f(\vec{a})$, where $a_1, a_2, ...$ represent the unknown parameters of the model. Assuming N_D independent data points, the general approach is to find the model parameters $\vec{a}$ that minimize the so called uncorrelated χ^2, defined as

$$\chi^2(\vec{a}) = \sum_{i=1}^{N_D} \frac{[\bar{C}(t_i) - f(\vec{a}, t_i)]^2}{e_i^2}, \tag{2.107}$$

where $\bar{C}(t_i)$ is the average value of the i^{th} data point over all the configurations N,

$$\bar{C}(t_i) = \frac{1}{N}\sum_{k=1}^{N} C_k(t_i) \tag{2.108}$$

with e_i its standard error (see section 2.13 for more details). The number of data points to be fit minus the number of parameters to be determined gives the number of degrees of freedom, dof. With many degrees of freedom, we expect to get $\chi^2 = dof \pm \sqrt{2dof}$, so $\chi^2/dof \simeq 1$ indicates a good fit[15].

In Monte Carlo simulations, the data points are more likely to be correlated since, for instance, the correlators necessary to obtain hadron masses are calculated from the same operator and gauge configurations. The function to minimize in this case is the correlated χ^2

$$\chi^2(\vec{a}) = \sum_{i,j=1}^{N_D} (\bar{C}(t_i) - f(\vec{a}, t_i))(Cov^{-1})_{ij}(\bar{C}(t_j) - f(\vec{a}, t_j)). \tag{2.109}$$

Cov is the covariance matrix which describes correlations among the data points or correlators. It describes the distribution of the data around the mean value $\bar{C}(t_i)$ and it can be written as

$$Cov_{ij} = \frac{1}{N(N-1)}\sum_{k=1}^{N}(C_k(t_i) - \bar{C}(t_i))(C_k(t_j) - \bar{C}(t_j)). \tag{2.110}$$

Note that only when the number of measurements is much larger than the number of data points, $N >> N_D$, a good estimate of the covariance matrix is possible. In the other cases, the estimated covariance matrix introduces too much noise in the fit, or in other words, the correlated χ^2 would be larger than one[16]. In this work we will always quote uncorrelated fit results.

---

[15] The probability distribution for the best fit is the probability distribution for χ^2, i.e. for a (dof) dimensional vector: each component will be Gaussian distributed with a standard deviation of unity.

[16] In the extreme case $N \leq N_D$, the smallest eigenvalues are zero and the covariance matrix cannot be inverted.

2.13 Error Analysis

Numerical simulations on the lattice introduce two sources of errors: statistical and systematic errors. The latter are due for instance to the finite size of the lattice and the finite lattice spacing. Systematic errors are also introduced in the fitting procedure described in the previous section, for instance in the choice of the time range. Usually the systematic uncertainties are considered negligible if smaller than the statistical errors. A calculation of systematic errors is often difficult since several sources of errors need to be included in the analysis. We will discuss finite volume effects, a possible source of systematics, in chapter 4, but in this work we will always quote statistical errors, except where specified.

The statistical errors come from the fact that performing the functional integrals as seen in section 2.9 in order to compute observables, employs statistical sampling: the results then will have statistical errors. The so called standard error is simply calculated from the standard deviation of the average of our measurements. Keeping the same conventions as in section 2.12, it is given by

$$e_s = \sqrt{\frac{\sigma_i^2}{N-1}} = \sqrt{\frac{\sum_{k=1}^{N}(C_k(t_i) - \bar{C}(t_i))^2}{N(N-1)}}. \tag{2.111}$$

Accurate methods for estimating the standard error and taking into account correlations within the measurements are the *jackknife* and *bootstrap* methods. They are methods of regrouping a data sample in order to find a reliable estimate of the error for a quantity computed from that sample.

2.13.1 Jackknife Method

Starting from a sample of N values, the jackknife method removes one of them in turn, leaving a sample size of $N-1$: the analysis is carried out on the reduced set of

$N-1$ configurations and a best fit result for the parameters is obtained. Then the measurement is repeated N times, each time removing a different element of the sample. The jackknife variance is the average of the squared deviation multiplied by $N-1$ to compensate for the bias introduced by the reuse of data in constructing the sample:

$$\sigma_i^2 = \frac{N-1}{N} \sum_{k=1}^{N} (\hat{C}_k(t_i) - \bar{C}(t_i))^2, \tag{2.112}$$

where $\hat{C}_k(t) = \frac{1}{N-1} \sum_{i=1, i \neq k}^{N} C_i(t)$.

2.13.2 Bootstrap Method

The bootstrap method has similarities with the jackknife, but the main difference is that it involves a random selection of N values, where N is the total number of configurations. The quantity of interest is then evaluated from this sample. This procedure is repeated N_{boot} times, giving N_{boot} replications of the quantity to estimate, one for each bootstrap sample. In this case, it is possible that the new set has repetitions: in fact we could even have $N_{boot} > N$. The standard error is given by the standard deviations on the N_{boot} estimates or replications. The advantage of the bootstrap sampling method is that it does not assume any prior form for the distribution of the correlation functions.

Chapter 3

Scaling and Asymptotic Scaling

The two main features of the strong interactions are *asymptotic freedom* and *confinement*, related to their properties in the high and low energy regimes, respectively.

One way to show that QCD is the correct theory of strong interactions is through the coupling constant: the coupling extracted at different scales is unique, in the sense that its variation with scales is described by the renormalization group[1]. The consequence is that the coupling constant that appears in the QCD Lagrangian or action, see eqs.(2.5 & 2.7), becomes a *running coupling* in the full quantum theory and its dependence on the energy scale is quantified by the so-called β-function. Through the perturbative study of the β-function, it was shown that at very high energies the coupling becomes so small that the quarks are like free particles - hence the term *asymptotic freedom.*

In the following section we will explore in detail the concept of asymptotic freedom. We will see that it is necessary that lattice predictions of QCD reproduce the weak coupling perturbation theory in the limit of the bare coupling going to

---

[1] The renormalization group equation describes how the parameters behave by changing the scale of the theory, in the case of our interest, the lattice spacing.

zero, $g_0 \to 0$. However, it is a generally known problem that the behaviour predicted from perturbation theory for asymptotically free theories like QCD has not yet been observed in Monte Carlo simulations of these theories. This discrepancy has been explained in the past [24] with the poor convergence properties of the perturbative series in the bare coupling constant.

This chapter is devoted to illustrate this possibility and in particular to explore an alternative method which explains the disagreement between Monte Carlo data and perturbative scaling through the presence of *lattice artefacts.*

3.1 Asymptotic Scaling

The term asymptotic freedom implies that the running coupling goes to zero as the momentum scale, μ, goes to infinity, in accordance with predictions from perturbation theory. The β-function quantifies the dependence of the coupling on the scale μ through the renormalization group equation, $\beta(\mu) = \mu\frac{\partial g}{\partial \mu}$.

In a lattice regularised theory, μ is replaced by a^{-1}, the inverse lattice spacing. For a finite lattice spacing, a, the functional dependence of the coupling $g(a)$ on a will depend on the observable considered. For sufficiently small a, however, a universal function $g(a)$ should exist, which ensures the finiteness of any observable. The renormalization group equation for the bare coupling on the lattice is given by:

$$\beta_L(g_0^2) = -a\frac{dg_0^2}{da} = -2b_0g_0^4 - 2b_1g_0^6 - 2b_2g_0^8 + \ldots, \tag{3.1}$$

where the one- and two-loop coefficients, b_0 and b_1, are scheme independent. In the case of $SU(N)$ pure-gauge theories, when the number of flavours is equal to zero, they depend only on the number of colours[2] N:

$$b_0 = \frac{11}{3\,(4\pi)^2}\,N, \qquad b_1 = \frac{34}{3\,(4\pi)^4}\,N^2. \tag{3.2}$$

The three-loop coefficient b_2 is scheme-dependent and its expression in the lattice scheme, b_2^L, can be obtained with a 2-loop calculation relating the lattice coupling to some other coupling for which b_2 is already known. For the Wilson pure-gauge $SU(N)$ action, the three-loop coefficient on the lattice is [25]

$$b_2^L = \left(\frac{N}{16\pi^2}\right)^3 \left(-366.2 + \frac{1433.8}{N^2} - \frac{2143}{N^4}\right). \tag{3.3}$$

Integrating the expression of the β-function (3.1) up to three loops, one obtains a relation between g_0 and a which is the usual expression for the running of the coupling:

$$a^{-1} = \frac{\Lambda_L}{f_{PT}(g_0^2)}, \tag{3.4}$$

where

$$\begin{aligned} f_{PT}(g_0^2) &= e^{-\frac{1}{2b_0g_0^2}}\ (b_0g_0^2)^{\frac{-b_1}{2b_0^2}}\ (1 + \frac{1}{2b_0^3}(b_1^2 - b_2^L b_0)g_0^2) \\ &= e^{-\frac{1}{2b_0g_0^2}}\ (b_0g_0^2)^{\frac{-b_1}{2b_0^2}} (1 + d_2^L g_0^2) \end{aligned} \tag{3.5}$$

is the scaling function. The subscript 'PT' refers to quantities obtained from weak-coupling perturbation theory. The integration constant Λ_L is the scale of the lattice regularized theory with dimensions of mass. It is the fundamental QCD parameter Λ_{QCD} 'measured' in the lattice scheme, and can be related to Λ_{QCD} in other schemes by a multiplicative constant. In a pure gauge theory (i.e. number of flavours $N_f = 0$) there exists only one relevant coupling corresponding to a single universal scaling function defined in equation (3.5). Every physical quantity

---

[2] Note the number of colours will be referred as N in this chapter.

with dimension of a mass must then be proportional to Λ_L in the continuum limit. And the mass in lattice units, which is the quantity that one evaluates in numerical simulations, should vary as a function of g_0 according to eqs.(3.4 & 3.5) as the coupling goes to zero, $g_0^2 \to 0$. This perturbative scaling behaviour is called *asymptotic scaling.*

However, this perturbative behaviour has not been observed for current parameter values in lattice simulations when the coupling used is the bare coupling g_0. This old problem has been approached in the past by stressing the need for improved lattice coupling schemes, in particular by Lepage and Mackenzie [24]. In fact, using a *renormalized* coupling, g_R, usually defined in terms of quantities obtained from a Monte Carlo simulation, enhances the convergence of the perturbative series. Lattice perturbation theory expressed in terms of g_R then becomes much more reliable. Of course the choice of the expansion parameter is not unique and its value can depend on the length scale relevant to the process considered.

An alternative point of view to the renormalized coupling approach has been developed [26] where the presence of cut-off effects due to the finiteness of the lattice spacing are assumed to cause the disagreement between Monte Carlo data and the asymptotic scaling formula. Following this alternative scenario, we extended the work in [26] in different directions, as illustrated in detail in the rest of this chapter.

3.2 Lattice-Distorted Perturbation Theory

The approach described in this section, called "Lattice-Distorted Perturbation Theory", stresses the need for lattice spacing corrections. Any quantity determined from a lattice simulation will suffer from systematic lattice spacing effects due to the discretization inherent in the lattice action used. Thus, for example, gluonic sector quantities in quenched SU(3), will have $\mathcal{O}(a^2)$ errors associated with them when the Wilson action (see eq.(2.17)) is used. It is then natural to assume that eqs.(3.1 & 3.4) will need to be adjusted by these same $\mathcal{O}(a^2)$ systematics whenever the scale is determined by such a gluonic sector quantity obtained from a Monte Carlo simulation. The coefficients of these $\mathcal{O}(a^2)$ terms can be found from simple fits to the Monte Carlo data, and will be, in general, quantity dependent.

A complete parametrization of the lattice β-function should include both the $\mathcal{O}(a^n)$ terms and higher order terms in g_0^2, since the observed lack of asymptotic scaling is presumably due to a mixture of the two effects [26], [27]: (i) the presence of lattice artefacts due to the finiteness of a and (ii) the inclusion of only a finite number of terms in the PT expansion. We can then write the lattice β-function in the following implicit form:

$$\begin{aligned} \beta_L(g_0^2) &= -a\frac{dg_0^2}{da} = -2(b_0 g_0^4 + b_1 g_0^6 + b_2^L g_0^8 + \sum_{l=4} b_{l-1}^L g_0^{2l+2}) \\ &\times (1+\sum_{n=1} c_n(g_0^2) a^n(g_0^2)). \end{aligned} \tag{3.6}$$

This is simply eq.(3.1) with the addition of $\mathcal{O}(a^n)$ terms. The c_n are the (non-universal) coefficients of the $\mathcal{O}(a^n)$ terms and are, in general, polynomial functions of g_0^2.

Equation (3.6) can be integrated giving

$$a^{-1}(g_0^2) = \frac{\Lambda_L}{f_{PT}(g_0^2)} \times (1+\sum_{l=4} d_{l-1}^L g_0^{2l-4})^{-1} \times (1+\sum_{n=1} c'_n(g_0^2) f_{PT}^n(g_0^2)), \tag{3.7}$$

where f_{PT} is defined in equation (3.5). The $\mathcal{O}(a^n)$ term has been expressed in terms of f_{PT}^n without any loss of generality since any difference between a and f_{PT}

is higher order and can be absorbed into the coefficients $c'_m(g_0^2)$ for $m \geq n$.

We will use this ansatz for the asymptotic scaling function later in this work. For the moment we set the higher order coefficients in g_0^2, d^L, to zero and focus our attention on lattice-distorted PT, i.e. on the $\mathcal{O}(a^n)$ part.

While there can be no doubt about the presence of such $\mathcal{O}(a^n)$ corrections, their importance could be questioned: we will show that their contribution is actually never negligible and that their coefficients turn out to be of the order we expect. In order to make progress with fitting data, higher order terms in eq.(3.7) are truncated leaving the following simpler form:

$$a^{-1}(g_0^2) = \frac{\Lambda_L}{f_{PT}(g_0^2)} \times \left[1 - X_{n,\nu}\frac{g_0^{\nu} f_{PT}^n(g_0^2)}{G_{std}^{\nu} f_{PT}^n(G_{std}^2)} - Y_{n',\nu'}\frac{g_0^{\nu'} f_{PT}^{n'}(g_0^2)}{G_{std}^{\nu'} f_{PT}^{n'}(G_{std}^2)}\right]. \tag{3.8}$$

Here $X_{n,\nu}$ and $Y_{n',\nu'}$ are respectively the leading-order (LO) and the next-to-leading-order (NLO) coefficients of the $\mathcal{O}(a^n)$ expansion, and there is no implicit summation over n and ν. As described in the following, we performed both LO ($Y_{n',\nu'} \equiv 0$) and NLO fits[3]. The values of the indices n, n', ν, ν' depend upon the lattice action and the quantities used to set a, as better explained below. The variation of the coefficients $c_n(g_0^2)$ with g_0 is truncated to leading order, hence the presence of the g_0^{ν} and $g_0^{\nu'}$ terms. The values of ν and ν' will be discussed below. The $\mathcal{O}(a^n)$ terms are normalized so that for example $X_{n,\nu}$ is the fractional systematic effect coming from the $\mathcal{O}(a^n)$ term at some standard (i.e. convenient) value of g_0, G_{std}. The values of $\beta \equiv 2N/g_0^2$ corresponding to the standard values G_{std} for the different actions considered are listed in Table 3.1. For the Wilson action, sections 3.6 and 3.7 show an analysis of $SU(N)$ data for N number of colours different from 3, so Table 3.1 also shows the β_{std} value for each N considered. These

---

[3] When we had enough data, we also performed NNLO fits, as a test for the convergence of the series (see section 3.4).

Action	N	$\beta_{std} = 2N/G_{std}^2$
Wilson	2	2.45
Wilson	3	6.0
Wilson	4	11.0
Wilson	5	17.45
Wilson	6	25.2
Wilson	8	45.5
Iwasaki	3	2.6
DBW2	3	1.04

Table 3.1: Values for the "standard" coupling, G_{std}, expressed in terms of $\beta_{std} = 2N/G_{std}^2$, for the different actions and number of colours considered in this work.

values for G_{std} were chosen in order to have the lattice spacing $a^{-1} \sim 2$ GeV at $g_0 = G_{std}$.

3.3 Setting the Scale and Data Sets

Lattice calculations set the scale a^{-1} by calculating some (dimensionless) quantity on the lattice, Ω^L, and comparing it with its experimental (dimensionful) value, Ω^{exp}:

$$a^{-1} = \frac{\Omega^{exp}}{\Omega^L}. \tag{3.9}$$

Once one dimensionful low energy observable is specified, all other dimensionful quantities can be expressed in terms of it. We consider different physical quantities to set the scale a, listed in the first column of Table 3.2: the hadronic scale r_0 [28], the string tension σ and the critical temperature T_c. The method of lattice planes also provides an alternative way to set the scale a [33]. The length scale r_c is an additional reference scale analogous to (but smaller than) r_0, defined through the force $F(r)$ between static quarks. The range where one has the best information

	Gauge Action		
	Wilson	Iwasaki	DBW2
r_0, r_c	$\mathcal{O}(g^2a^2)+\mathcal{O}(g^2a^4)$	$\mathcal{O}(g^2a^2)+\mathcal{O}(g^2a^4)$	$\mathcal{O}(g^2a^2)+\mathcal{O}(g^2a^4)$
σ, T_c	$\mathcal{O}(a^2)+\mathcal{O}(a^4)$	$\mathcal{O}(a^2)+\mathcal{O}(a^4)$	$\mathcal{O}(a^2)+\mathcal{O}(a^4)$
Method of Planes	Fermionic action		
	$\mathcal{O}(g^2a)+\mathcal{O}(a^2)$		

Table 3.2: LO and NLO correction terms in the fitting function (3.8) for each lattice quantity and each action used.

on $F(r)$ is at distance of around 0.5 fm [28]. One then calculates $r(c)$ satisfying the equation

$$r^2F(r)|_{r=r(c)} = c, \qquad r_0 = r(1.65) \approx 0.5fm. \tag{3.10}$$

When one is interested in short distance properties of the theory, it is convenient to choose a smaller reference length scale [29],

$$r_c^2F(r_c) = 0.65, \tag{3.11}$$

related to r_0 through $r_c/r_0 = 0.5133(24)$ [29]. This smaller length scale allows one to work with larger beta values without being constrained by finite volume effects.

In Table 3.2, the values for n, n', ν, ν' in eq.(3.8) for both the LO and the NLO terms are listed. As already mentioned, these different values for n, n', ν, ν' are due to the different discretization errors associated with the different actions considered. Note that the behaviour of the scale obtained from the method of planes is different from the other cases with the Iwasaki action. This is because it is derived from the meson masses and thus the quark part of the action has to be included. The leading scaling violation of the quark clover action considered in [30] is $\mathcal{O}(g^2a)$.

Our sources of $SU(3)$ data are [29], [30] and [31]. In [29] the quantities r_0 and r_c are considered. In particular, the ratio r_0/a is evaluated for the usual Wilson plaquette action, as well as for the Iwasaki and DBW2 actions. [29] also defines the additional reference scale r_c for $\beta \geq 6.57$ only. Since we wish to use r_c values over the entire β range, we evaluate r_c for $\beta < 6.57$, by locally interpolating the force $F(r)$ between static quarks using data taken from [32]. The results for the full β range are listed in Table 3.3. Tables 3.4 and 3.5 show the r_0/a values used for the Iwasaki and DBW2 actions respectively.

The string tension data used for the Wilson and Iwasaki actions are listed in Tables 3.3 and 3.4 respectively. The string tension σ is commonly defined through the static quark potential

$$V(r) = const. + \sigma r + \frac{\gamma}{r} + \mathcal{O}(\frac{1}{r^2}), \tag{3.12}$$

where γ is an universal factor depending only on the dimensions of the system.

The physical temperature for a given lattice spacing a, is related to the time extent of the lattice N_t by

$$\frac{1}{T} = N_t a(\beta), \tag{3.13}$$

thus the temperature can be varied by either changing N_t or by varying the lattice spacing (which can be achieved by changing the coupling). To determine the critical temperature at a phase transition[4] one usually studies the temperature dependence of an order parameter, like for example the Polyakov loop. The general idea consists of fixing N_t, while varying the gauge coupling β or g, and therefore implicitly the lattice spacing, and, via eq.(3.13), the temperature. In this way one

---

[4] The phase transition is characterized by the fact that for $T < T_c$ the confining string tension is non-zero, $\sigma \neq 0$, while for $T > T_c$ we have $\sigma = 0$.

moves the lattice system through the phase transition obtaining

$$\frac{1}{T_c} = N_t a(\beta_c), \tag{3.14}$$

where β_c is the critical coupling. Tables 3.3, 3.4 and 3.5 show the values of β_c at given N_t for the Wilson, Iwasaki and DBW2 actions respectively.

The last column in Table 3.4 contains the values for a^{-1} using the method of lattice planes [33] obtained by [34] using the meson masses from [30]. In this method, lattice physical planes for masses and decay constants are defined in order to set the scale and to determine physical quantities, without relying on chiral extrapolations. Specifically on the plane $(M_V a, (M_{PS} a)^2)$, the intercept of the curve $M_V a = M_{K*}/M_K \sqrt{(M_{PS} a)^2}$ with the linear fit of the lattice data defines $M_K a$ and $M_{K*} a$. The lattice spacing a can then be set by comparing one of the values found with its well determined experimental value.

Finally, Table 3.6 shows all the values for a^{-1} we will use in our fits to eq.(3.8). These a^{-1} were obtained from Tables 3.3, 3.4 and 3.5 using the following values[5]:

$$\begin{aligned} r_0 &= 0.49\ fm \qquad r_c = 0.49 \times 0.5133\ fm \\ T_c &= 300\ MeV \qquad \sigma = (440\ MeV)^2. \end{aligned} \tag{3.15}$$

All the tables of data show the references from where the data are taken.

---

[5] Note that those are the correct values for $SU(3)$. For $N \neq 3$, if we fix one of the above quantities to its SU(3) value, the others are expected to differ from their respective quoted values by an $\mathcal{O}(1/N^2)$ correction.

3.3.1 Data

β Ref	β_c [35]	r_c/a	$a\sqrt{\sigma}$ [31]	N_t [35]
5.6925			0.3970(19)	
	5.6925(2)			4
5.6993			0.3933(16)	
5.7995			0.3148(12)	
5.8			0.3133(13)	
	5.8941(5)			6
5.8945			0.2607(11)	
5.95		2.53(1)		
	6.0624(12)			8
6.0625			0.19466(73)	
6.07		3.09(1)		
6.2		3.79(2)		
6.3380			0.12930(69)	
	6.3380(23)			12
6.4		5.02(2)		
6.57		6.25(4)		
6.69		7.29(5)		
6.81		8.49(5)		
6.92		9.82(6)		

Table 3.3: SU(3) Wilson data used to set the scale, a. r_c/a values for $\beta \geq 6.57$ are taken directly from [29], and those for $\beta < 6.57$ are obtained using force data from [32] as described in the text.

β	β_c	r_0/a	σa^2	N_t	a^{-1} [GeV] method of lattice planes
Ref	[36]		[30]	[36]	[30, 34]
	2.1551(12)	2.320(11)		3	
2.187		2.494(35)	0.2157(32)		1.0238(116)
2.214		2.621(43)	0.1949(25)		1.0769(132)
2.247		2.801(28)	0.1713(18)		1.1314(141)
2.281		3.001(36)	0.1487(17)		1.1643(158)
	2.2879(11)	3.026(5)		4	
2.334		3.289(23)	0.1241(14)		1.2587(147)
2.416		3.824(13)	0.0921(10)		1.4228(202)
2.456		4.080(16)	0.0800(16)		1.5410(160)
2.487		4.286(15)	0.0725(11)		1.5971(202)
	2.5206(24)	4.511(8)		6	
2.528		4.570(21)	0.0637(11)		1.6989(212)
2.575		4.887(16)	0.0561(7)		1.8119(220)
	2.7124(34)	5.999(24)		8	

Table 3.4: SU(3) Iwasaki data used to set the scale, a. The r_0/a data come from two sources: [29] for the critical β values, [30] for the other β values.

β, β_c	r_0/a	N_t
Ref	[29]	[37]
0.75696(98)	2.225(12)	3
0.82430(95)	3.036(17)	4
0.9636(25)	4.556(26)	6
1.04	5.452(27)	

Table 3.5: SU(3) DBW2 data used to set the scale, a.

3.4 Details of the Fit and Results

We perform a simple least chi squared fit of the data for a^{-1} in each column of Table 3.6 to eq.(3.8).

Both LO and NLO fits were performed as a test of the convergence properties of the lattice distorted perturbation theory approach. As a check, for those quantities

	a^{-1} [GeV] from						
β	r_c	r_0	$\sqrt{\sigma}$	T_c	$K-K^*$	Action	Ref.
5.6925				1.2000(3)		Wilson	[29]
5.6925			1.108(5)			Wilson	[31]
5.6993			1.119(5)			Wilson	[31]
5.7995			1.398(5)			Wilson	[31]
5.8			1.404(6)			Wilson	[31]
5.8941				1.8000(11)		Wilson	[29]
5.8945			1.688(7)			Wilson	[31]
5.95	1.985(8)					Wilson	[29]
6.0624				2.4000(34)		Wilson	[29]
6.0625			2.260(8)			Wilson	[31]
6.07	2.424(8)					Wilson	[29]
6.2	2.973(16)					Wilson	[29]
6.3380				3.6000(99)		Wilson	[29]
6.3380			3.403(18)			Wilson	[31]
6.4	3.938(16)					Wilson	[29]
6.57	4.903(31)					Wilson	[29]
6.69	5.719(39)					Wilson	[29]
6.81	6.661(39)					Wilson	[29]
6.92	7.704(55)					Wilson	[29]
2.1551		0.934(4)		0.9000(13)		Iwasaki	[29]
2.187		1.004(14)	0.947(7)		1.024(12)	Iwasaki	[30]
2.214		1.056(17)	0.997(6)		1.077(13)	Iwasaki	[30]
2.247		1.128(11)	1.063(6)		1.131(14)	Iwasaki	[30]
2.281		1.209(15)	1.141(7)		1.164(16)	Iwasaki	[30]
2.2879		1.219(2)		1.2000(16)		Iwasaki	[29]
2.334		1.325(9)	1.249(7)		1.259(15)	Iwasaki	[30]
2.416		1.540(5)	1.450(8)		1.423(20)	Iwasaki	[30]
2.456		1.643(6)	1.556(16)		1.541(16)	Iwasaki	[30]
2.487		1.726(6)	1.634(12)		1.597(20)	Iwasaki	[30]
2.5206		1.817(3)		1.8000(52)		Iwasaki	[29]
2.528		1.840(8)	1.743(15)		1.699(21)	Iwasaki	[30]
2.575		1.968(6)	1.858(12)		1.812(22)	Iwasaki	[30]
2.7124		2.416(10)		2.4000(98)		Iwasaki	[29]
0.75696		0.896(5)		0.9000(11)		DBW2	[29]
0.82430		1.223(7)		1.2000(14)		DBW2	[29]
0.9636		1.835(10)		1.8000(54)		DBW2	[29]
1.04		2.196(11)				DBW2	[29]

Table 3.6: Values for a^{-1} obtained from data in Tables 3.3, 3.4 and 3.5 by using the constants in eq.(3.15).

with enough data points, we included the *next-to-next-leading* term in the fit, but the results were entirely consistent with the NLO fits. Values for Λ_L, the coefficients X and, in the NLO case, Y, with corresponding χ^2, are listed in Tables 3.7, 3.8 and 3.9 for the Wilson, Iwasaki and DBW2 data respectively. The second column of these tables specifies the form of the scaling function f_{PT}, eq.(3.5), used in the fit, i.e. if the 3-loop term d_2^L is included or not. Notice that the 3-loop coefficient is not known for the Iwasaki and DBW2 actions, so d_2^L was left as a free parameter in the 3-loop fits to data from these actions.

3.4.1 Comments

Some comments about the results in Tables 3.7, 3.8 and 3.9 are necessary. The X parameters from the NLO fits are compatible with those from the LO fits. Furthermore in the NLO fit, the coefficient Y is an order of magnitude smaller than the coefficient X. This suggests that the expansion in f_{PT} forms a convergent series, with most of the cut-off effects being due to the leading order term at these β values. Note also that the size of the cut-off effects for the Wilson data at the "standard" coupling $\beta_{std} = 6.0$ is around 20-25%, very compatible with what was found previously [26].

It is interesting to note that the X coefficients for the Iwasaki action for r_0 are significantly smaller than the 20-25% values obtained in the Wilson case. This suggests that the Iwasaki action is optimized to reduce the lattice artefacts in this quantity. It is difficult to draw similar conclusions for the DBW2 case since there are too few data points available.

From the χ^2 values in Tables 3.7, 3.8 and 3.9, the quality of the LO and NLO fits is generally excellent. Note also that the χ^2 values for the NLO fits are smaller than for the LO ones (with the single exception of the DBW2 action where there are a very small number of data points).

Let's notice that if

$$g'^2 = g^2 + r_1 g^4 + r_2 g^6 + ... \tag{3.16}$$

is the relation between the running couplings in two different schemes, the lambda parameters in those two schemes are related by

$$\Lambda' = \Lambda e^{r_1/2b_0}, \quad b_2' = b_2 - b_1 r_1 + b_0(r_2 - r_1^2) \tag{3.17}$$

where the second expression is the relation between the 3-loop coefficients, which will be useful later in this chapter.

We can convert Λ_L to the generally used $\overline{MS}$ scheme, $\Lambda_{\overline{MS}}$. In the Wilson case, the known conversion factor [40] is

$$\left(\frac{\Lambda_{\overline{MS}}}{\Lambda_L}\right) = 38.852704\ exp\left(-\frac{3\pi^2}{11N^2}\right) \tag{3.18}$$

with N number of colours. For SU(3) this gives the value listed in Table 3.10. As can be seen from Table 3.7, the $\Lambda_{\overline{MS}}$ values for the three quantities considered in the Wilson case are consistent to within ~5% for the 3-loop NLO case. These differences are, at some level, due to the uncertainty in the physical values used, eq.(3.15). Also, since the data studied here is quenched, we cannot expect perfect agreement for all lattice quantities.

The $\Lambda_{\overline{MS}}$ values from the 2-loop NLO case are ~15% lower than the 3-loop case, in agreement with what expected due to the addition of the $d_2^L g_0^2$ term in the definition of the 3-loop f_{PT}, eq.(3.5). Since the range of g_0^2 is very modest, this 3-loop term is essentially a constant for the data considered, and in the SU(3) Wilson case we have $d_2^L = 0.1896$.

Due to the very good agreement between them, we take our best estimate of $\Lambda_{\overline{MS}}$ using r_c and T_c data in the 3-loop NLO case. We assign an error of $\sim 10\%$ to this value due to uncertainties in the physical estimate of r_c and T_c, and to allow for the small discrepancy between the $\Lambda_{\overline{MS}}$ values obtained from the string tension σ and from r_c and T_c. We therefore have (using eq.(3.18)):

$$\Lambda_{\overline{MS}}^{N_f=0} = 217 \pm 21 \ \ MeV, \tag{3.19}$$

similar to previous lattice determinations in quenched QCD [26], [38].

Using the conversion factors in Table 3.10 for the Iwasaki and DBW2 data unfortunately does not produce sensible values for $\Lambda_{\overline{MS}}$. Moreover, previous calculations of $\Lambda_{\overline{MS}}$ from improved actions found similar problems [39]. However despite this concern, the 2-loop Iwasaki Λ_L values are compatible for all the physical quantities considered, allowing for some additional uncertainties in the values in eq.(3.15). Introducing the 3-loop term in the fit with a free coefficient spoils this agreement. Note however, that the coefficient of this term, d_2^L, should be scheme-dependent and *not* quantity dependent. From Table 3.8 it is clear that d_2^L is highly unstable, and we therefore discount these 3-loop fits.

Table 3.9 shows the results obtained from the DBW2 data. In this case, the small amount of data points available did not allow an accurate investigation. However, the NLO 2-loop fit performed in the r_0 case confirms the validity of our approach.

We plot the data and the fits for a^{-1} versus β in figures 3.1 and 3.3 for the Wilson and the Iwasaki actions respectively. In order to show the high level of agreement between the data and the lattice distorted perturbation theory fits, we plot the ratio of the data to these fits in figures 3.2 and 3.4: they show that the

$\mathcal{O}(a)$	-loop	Quantity	Λ_L	X	Y	χ^2/dof	$\Lambda_{\overline{MS}}$
LO	2	r_c	6.41(2)	0.210(4)	-	2.2	184.8(6)
LO	2	T_c	6.163(7)	0.1776(4)	-	55	177.6(2)
LO	2	σ	5.94(2)	0.194(2)	-	2.1	171.1(7)
LO	3	r_c	7.48(2)	0.193(4)	-	1.2	215.5(7)
LO	3	T_c	7.250(8)	0.1683(4)	-	41	208.9(2)
LO	3	σ	6.97(3)	0.184(2)	-	1.5	200.9(8)
NLO	2	r_c	6.50(3)	0.27(2)	-0.047(16)	0.87	187(1)
NLO	2	T_c	6.44(3)	0.231(5)	-0.020(2)	0.44	185.6(8)
NLO	2	σ	6.09(6)	0.23(1)	-0.016(5)	0.40	175(2)
NLO	3	r_c	7.54(4)	0.23(2)	-0.031(16)	0.69	217(1)
NLO	3	T_c	7.53(3)	0.213(5)	-0.016(2)	0.87	216.8(9)
NLO	3	σ	7.12(7)	0.21(1)	-0.012(5)	0.42	205(2)

Table 3.7: Fit results for the SU(3) Wilson data using both LO and NLO and both 2- and 3-loop perturbation theory. All the Λ values are in MeV.

agreement is at the sub-percent level.

$\mathcal{O}(a)$	-loop	Quantity	Λ_L	X	Y	d_2^L	χ^2/dof
LO	2	r_0	225.6(5)	0.0563(4)	-	-	5.4
LO	2	T_c	235.5(7)	0.1704(9)	-	-	5.1
LO	2	σ	222(1)	0.163(3)	-	-	0.63
LO	2	$K-K^*$	216(3)	0.073(4)	-	-	0.98
LO	3	r_0	490(80)	0.040(2)	-	0.5(2)	0.6
LO	3	T_c	290(20)	0.158(4)	-	0.10(4)	0.5
LO	3	σ	350(140)	0.13(2)	-	0.3(3)	0.4
LO	3	$K-K^*$	$2(2)\times10^3$	0.006(6)	-	$4(5)\times10^3$	0.69
NLO	2	r_0	238(2)	0.083(3)	-0.0099(12)	-	0.44
NLO	2	T_c	241(2)	0.193(7)	-0.007(2)	-	0.97
NLO	2	σ	231(7)	0.21(3)	-0.02(1)	-	0.39
NLO	2	$K-K^*$	300(50)	0.35(11)	-0.4(2)	-	0.59
NLO	3	r_0	260(70)	0.08(2)	-0.008(4)	0.05±0.14	0.47
NLO	3	σ	110(30)	0.4(1)	-0.06(2)	-0.27(6)	0.3
NLO	3	$K-K^*$	160(50)	0.50(9)	-0.57(11)	-0.28(9)	0.67

Table 3.8: Fit results for the SU(3) Iwasaki data using both LO and NLO and both 2- and 3-loop perturbation theory. No NLO fit for the T_c data is possible due to the small number of data points available. All the Λ values are in MeV.

$\mathcal{O}(a)$	-loop	Quantity	Λ_L	X	Y	d_2^L	χ^2/dof
LO	2	r_0	1352(8)	0.0550(3)	-	-	2
LO	2	T_c	1894(7)	0.4995(7)	-	-	141
LO	3	r_0	1500(200)	0.053(2)	-	0.02(2)	3
NLO	2	r_0	1420(60)	0.07(1)	-0.008(7)	-	2.9

Table 3.9: Fit results for the SU(3) DBW2 data using both LO and NLO and both 2- and 3-loop perturbation theory. Due to the small number of data points available in this case, no LO 3-loop fit for T_c was possible, and the only NLO fit possible is the 2-loop r_0 case. All the Λ values are in MeV.

Action	$\Lambda_{\overline{MS}}/\Lambda_L$	Ref.
Wilson	28.81	[40]
Iwasaki	28.81/59.05	[40],[41]
DBW2	1/45.4	[42]

Table 3.10: Conversion factors for the Λ values between the $\overline{MS}$ and lattice schemes in SU(3) case.

3.5 Renormalized Coupling Fits

As already mentioned, performing the fit to Lattice-Distorted PT with a renormalized coupling constant instead of g_0, means fitting the data to the fitting function in eq.(3.7) with g_R replacing g_0.

The point of using a renormalized coupling is to enhance the convergence of the g_0 series, i.e. to *re-sum* the higher order terms by using a Monte Carlo quantity whose perturbative expansion is known and can therefore be used to define a *renormalized* coupling. For example, the coupling constant in the so called *energy scheme* [43], g_E, is defined as

$$g_E^2 = \frac{1}{c_1}\langle 1 - \frac{1}{N} Tr U_{plaq} \rangle = g_0^2 + \frac{c_2}{c_1} g_0^4 + \frac{c_3}{c_1} g_0^6 + \ldots, \qquad (3.20)$$

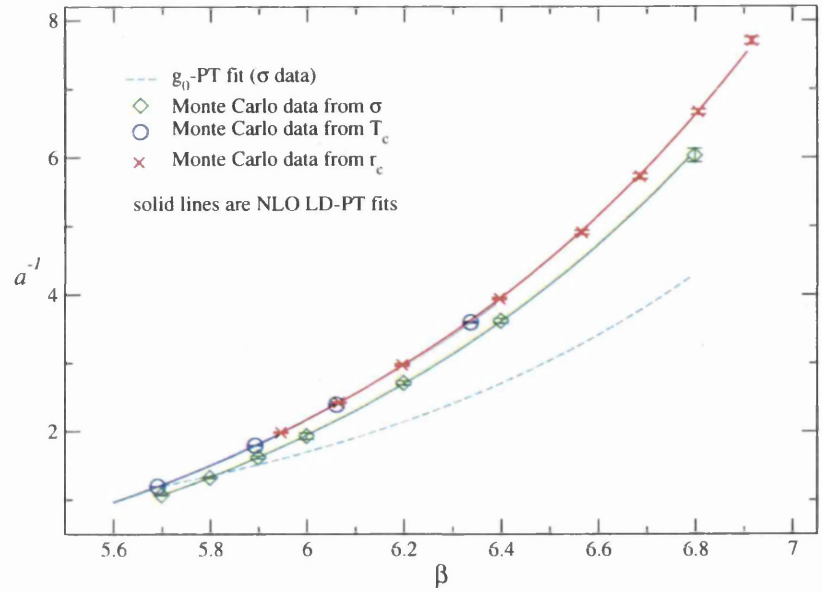

Figure 3.1: Plot of the SU(3) Monte Carlo data a^{-1} obtained from observables with the Wilson action together with the NLO 3-loop fits (using the parameters in Table 3.7).

using the weak expansion of the average plaquette [46, 47], [25],

$$\langle 1 - \frac{1}{N} Tr U_{plaq} \rangle = c_1 g_0^2 + c_2 g_0^4 + c_3 g_0^6 + ... \tag{3.21}$$

where

$$\begin{aligned} c_1 &= \frac{N^2-1}{8N} \qquad c_2 = \frac{N^2-1}{4}(0.02043 - \frac{1}{32N^2}) \\ c_3 &= \frac{N(N^2-1)}{8}(0.006354 - \frac{0.01812}{N^2} + \frac{0.01852}{N^4}). \end{aligned} \tag{3.22}$$

Many other possibilities for renormalized schemes have been used, i.e. g_{E2} [38], $g_{\overline{MS}}$ [44], g_{VI} and g_{VII} [24]. The idea of the g_{E2} scheme, for example, is to introduce a coupling by inverting the relation

$$\langle 1 - \frac{1}{N} Tr U_{plaq} \rangle = c_1 g_{E2}^2 + c_2 g_{E2}^4, \tag{3.23}$$

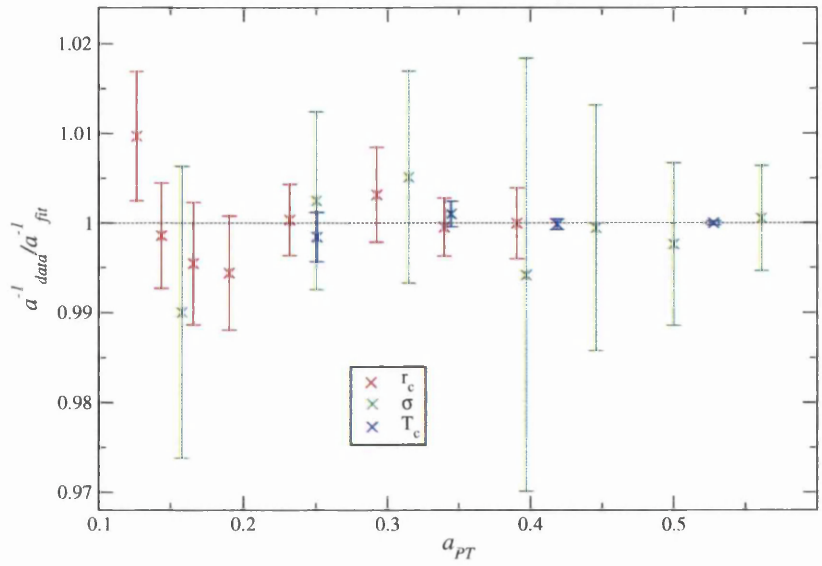

Figure 3.2: Plot of $a^{-1}_{data}/a^{-1}_{fit}$ versus a_{PT} for all SU(3) data in the Wilson case, where $a^{-1}_{PT} = \Lambda_L/f_{PT}(g_0^2)$, using the NLO 3-loop fit.

corresponding to truncating the weak expansion (3.21) after the second term. For the $\overline{MS}$ coupling we have:

$$\frac{1}{g^2_{\overline{MS}}(\frac{\pi}{a})} = \frac{1}{g_0^2}\langle 1 - \frac{1}{N}TrU_{plaq}\rangle + 0.025. \tag{3.24}$$

The definitions of g_{VI} and g_{VII} are related to the strength of the static quark-antiquark potential. If $\alpha_i(q)$ is the coupling strength of a gluon with momentum q, where $i = VI, VII$, its relation with the bare lattice coupling α_L[6] is given by:

$$\alpha_{VI}(\pi/a) = \frac{\alpha_L}{\langle 1 - \frac{1}{N}TrU_{plaq}\rangle}(1 + 0.513\alpha_{VI}), \tag{3.25}$$

and

$$-ln\langle 1 - \frac{1}{N}TrU_{plaq}\rangle = \frac{4\pi}{3}\alpha_{VII}(3.41/a)(1 - 1.19\alpha_{VII}). \tag{3.26}$$

---

[6] Note that $\alpha \equiv g^2/4\pi$.

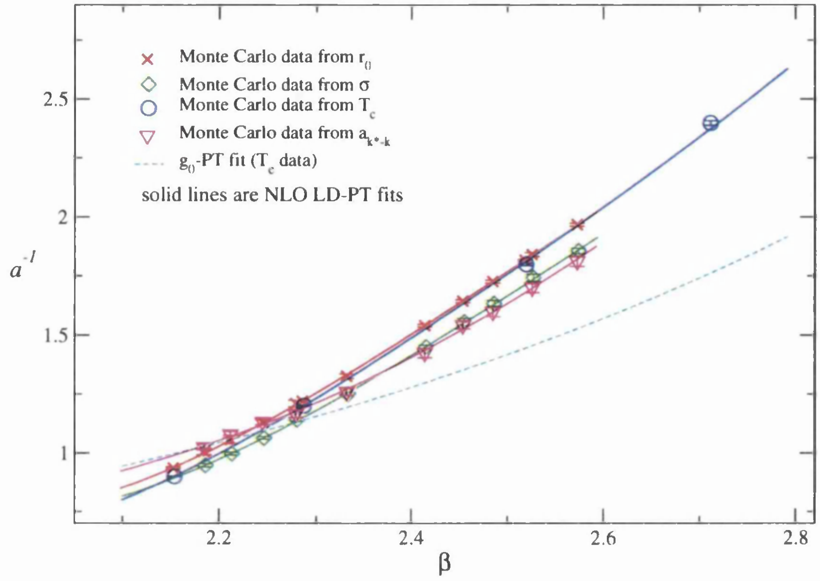

Figure 3.3: Plot of the SU(3) Monte Carlo data a^{-1} obtained from observables with the Iwasaki action together with the NLO 2-loop fits (using the parameters in Table 3.8).

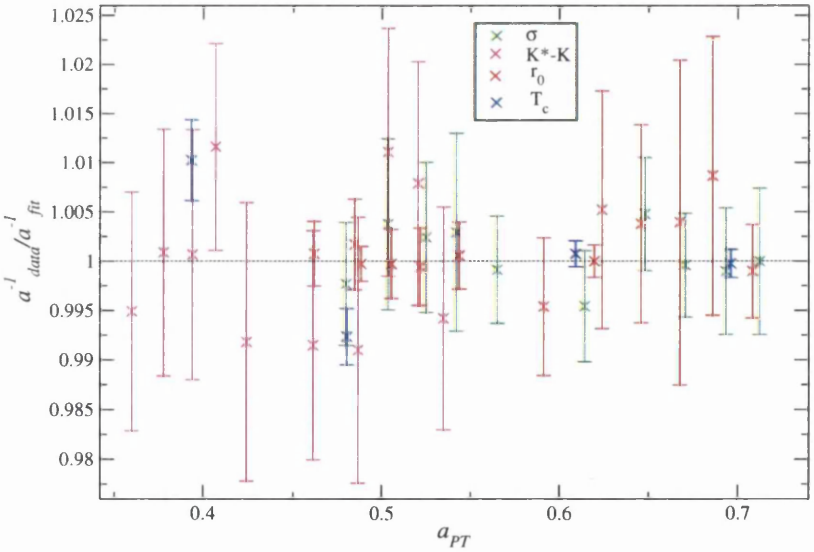

Figure 3.4: Plot of $a_{data}^{-1}/a_{fit}^{-1}$ versus a_{PT} for all SU(3) data in the Iwasaki case, where $a_{PT}^{-1} = \Lambda_L / f_{PT}(g_0^2)$, using the NLO 2-loop fit.

We included these schemes in our analysis, but it will be clear in the following why the g_E scheme became our favourite choice. Note that the plaquette values used here for SU(3) are from [45].

Before going on to describe our analysis, we should specify that the lattice coupling scheme is expected to have large higher order perturbative corrections, as we can see from the large ratio between Λ_L and $\Lambda_{\overline{MS}}$ (Table 3.10). This implies that the coefficient r_1 in the relation between the two couplings, eq.(3.16), must be also large, as one can easily see from eq.(3.17). So if $g^2_{\overline{MS}}$ is a 'good' scheme with modest higher order terms in the β-function, this will not probably be the case for the lattice coupling g_0^2. Since we only know the lattice β-function to 3-loops at most, it would be wise then to seek a lattice coupling scheme where there is less reason to expect large higher order corrections.

Figures 3.5, 3.6 and 3.7 show the χ^2/dof obtained in our different fits for the r_c, T_c and σ Wilson data respectively, using 3-loop perturbation theory. Note that g_E is the only renormalized coupling considered known to 3-loops, so the fits in the other renormalized schemes have always one extra fit parameter compared to the g_E and the g_0 schemes. In these figures, the expansion in g_0 and in a renormalized scheme with no $\mathcal{O}(a)$ terms, are labelled simply g_0 and g_R respectively. Clearly the χ^2/dof values for the g_0 scheme with no $\mathcal{O}(a)$ terms are extremely poor, as expected. Furthermore, while the renormalized schemes considered improve upon this situation, they still have unacceptably large χ^2/dof. Thus to obtain reasonable χ^2/dof values, one needs to include $\mathcal{O}(a)$ terms.

The g_0 scheme at LO and NLO of LDPT, give $\chi^2/dof \sim 1$, with the exception of the T_c fits, as shown in figure 3.6. In this case, the errors in the Monte Carlo data are so small (see Table 3.6), that NLO fits are required to obtain sensible fits.

Comparing g_R and g_0 fits at LO and NLO with the *same* number of fit parameters[7], we conclude that the LDPT g_0 fits are at least as good as the g_R fits augmented by $\mathcal{O}(a)$ terms.

We introduce some criteria which the fits should satisfy in order that a renormalized scheme successfully reproduces the data (we initially restrict attention to renormalized coupling fits without any $\mathcal{O}(a)$ terms). These criteria are:

(i) The 3-loop coefficient, d_2^L, should be smaller than the d_2^L value in the g_0 scheme for all quantities fitted, i.e. $d_2^L \leq 0.20$. This is an important feature since the main idea of the renormalized schemes is that perturbation expansions are better convergent than in the g_0 scheme.

As we can see in Table 3.11, this constraint leaves only two renormalized schemes, the g_E and g_{VII}.

(ii) The $\Lambda_{\overline{MS}}$ value should be in a sensible range:

$$200MeV \leq \Lambda_{\overline{MS}} \leq 250MeV.$$

(iii) Since the 3-loop coefficient, d_2^L, is scheme dependent, but *not* quantity dependent, we check that d_2^L is consistent for fits to the r_c, T_c and σ data.

Both these two criteria are satisfied only from the g_E scheme.[8]

(iv) Finally we demand that a sensible fit should have a χ^2/dof value less than 10.

This leaves no renormalized coupling scheme (at zeroth order in $\mathcal{O}(a)$) which satisfies the above four criteria. The clear implication of this is that the addition

---

[7] As commented above, the 3-loop coefficient is unknown for all the g_R schemes but the g_E one, so comparing fits with the same number of parameters means, for example, looking at g_0 at NLO and g_{VI} at LO.

[8] In fact, for the g_E scheme, the d_2^L value is known [25]. For $N = 3$, $d_2^E = \frac{1}{2b_0^3}(b_1^2 - b_2^E b_0) = 0.01163$.

of $\mathcal{O}(a)$ terms is crucial for there to be agreement between the fitting functions and the data.

Quantity	Λ	d_2^L	χ^2/dof	$\Lambda_{\overline{MS}}$
g_0-PT				
r_c	5.512(9)	0.1896	370	159
T_c	4.891(1)	0.1896	30000	141
σ	5.007(8)	0.1896	900	144
g_E-PT				
r_c	17.65(3)	0.01163	29	245
T_c	16.691(4)	0.01163	632	232
σ	15.74(3)	0.01163	68	218
g_{E2}-PT				
r_c	12.9(5)	0.357(48)	4.7	372
T_c	11.2(1)	0.207(9)	142	323
σ	18(1)	1.01(13)	3.4	519
$g_{\overline{MS}}$-PT				
r_c	136(5)	0.686(52)	7.7	136
T_c	370(12)	3.0(1)	18	370
σ	1200(450)	12(5)	3.6	1200
g_{VI}-PT				
r_c	206(7)	0.60(4)	7.4	129
T_c	438(10)	1.93(6)	17	274
σ	845(156)	4.6(9)	3.3	528
g_{VII}-PT				
r_c	141(3)	0.10(1)	3.6	88
T_c	122.0(5)	0.021(2)	183	76
σ	143(3)	0.15(1)	5.3	89

Table 3.11: Results from the zeroth order in $\mathcal{O}(a)$ fits for the SU(3) Wilson data, using 3-loop PT with different renormalized coupling constants. Note that for the g_0 and g_E schemes, the d_2^L coefficients are known, whereas they are fit parameters in the other schemes. All the lambda values are in MeV.

As we can see from Table 3.12, the quality of the fit improves drastically going from the g_E-PT without $\mathcal{O}(a^n)$ to the one with Lattice-Distorted PT terms. Also, a comparison between values from Table 3.12 and Table 3.7 in section 3.4.1

is further support for the validity of the Lattice-Distorted Perturbation Theory approach: the lattice artefacts provide the mismatch between Monte Carlo data and asymptotic scaling, without resorting to the use of a renormalized coupling.

To convert the lambda in the g_E scheme's Λ_E to $\Lambda_{\overline{MS}}$, we use

$$\frac{\Lambda_{\overline{MS}}}{\Lambda_E} = \frac{\Lambda_{\overline{MS}}}{\Lambda_L} \times \frac{\Lambda_L}{\Lambda_E} \tag{3.27}$$

with the formula for the ratio $\Lambda_{\overline{MS}}/\Lambda_L$ given in eq.(3.18) [40] and with

$$\frac{\Lambda_L}{\Lambda_E} = exp\left(-\frac{c_2}{2b_0c_1}\right), \tag{3.28}$$

from eqs.(3.17) and (3.20). The $\Lambda_{\overline{MS}}$ values obtained are listed in last column of Table 3.12.

As can be seen, the spread in the $\Lambda_{\overline{MS}}$ values obtained from different physical quantities, is greatest for the zero-th order fits: as we turn on the $\mathcal{O}(a)$ terms, $\Lambda_{\overline{MS}}$ becomes more stable.

We take our best estimate of $\Lambda_{\overline{MS}}$ using the 3-loop NLO fits. We assign an error of 10% to this estimate to allow for uncertainties in the physical estimate of r_c, T_c and σ, as we did in the g_0 case. From the g_E fits we therefore have:

$$\Lambda_{\overline{MS}}^{N_f=0} = 255 \pm 26 \ \ MeV. \tag{3.29}$$

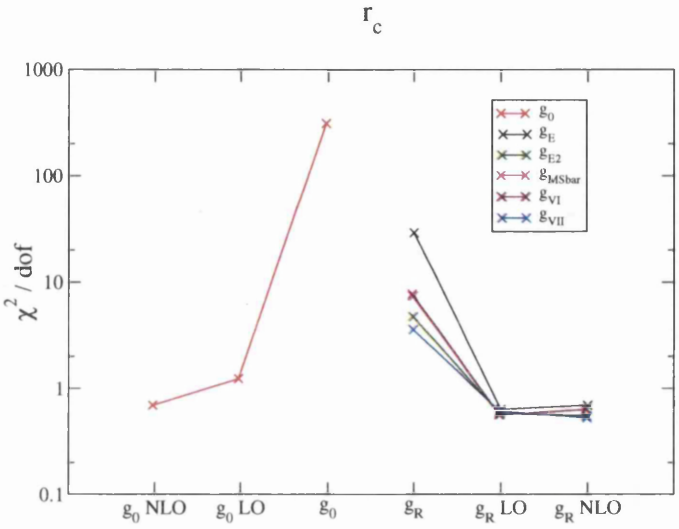

Figure 3.5: Plot of the χ^2/dof obtained in the SU(3) r_c data fits (Table 3.3) in different schemes, using 3-loop PT and up to NLO *Lattice Distorted PT*. The lines connecting the data points are guides for the eye.

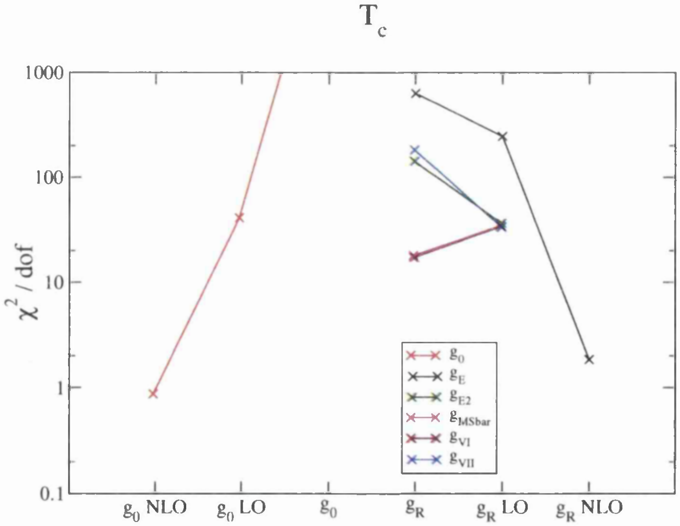

Figure 3.6: Plot of the χ^2/dof obtained in the SU(3) T_c data fits (Table 3.3) in different schemes, using 3-loop PT and up to NLO *Lattice Distorted PT*. The lines connecting the data points are guides for the eye.

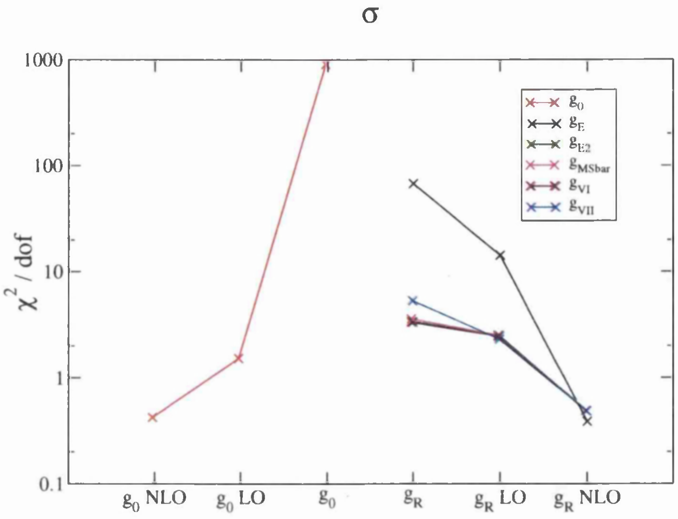

Figure 3.7: Plot of the χ^2/dof obtained in the SU(3) σ data fits (Table 3.3) in different schemes, using 3-loop PT and up to NLO *Lattice Distorted PT*. The lines connecting the data points are guides for the eye.

3.6 SU(N)

This section reports results of a first application of the Lattice-Distorted PT method to SU(N) data, when the number of colours N is different from 3. Our sources of data are [31], [48], [49], [50], [51] and [52] and their values are reproduced in Table 3.13 for the SU(2) case, and Table 3.14 for other SU(N) cases. All data is for the Wilson gauge action.

Looking at those tables of data, we can easily notice the short range of beta values, even for those sets with several data points. We will see how such a short range in a will constrain our fits and results. In the SU(2) case, there is more data available in [31] and [48] at smaller β values, but it corresponds to an inverse lattice spacing $a^{-1} < 0.9$ GeV. In order to be compatible with our SU(3) fits, we do not include this data in our fits. All the other SU(N) data have $a^{-1} > 0.9$ GeV.

$\mathcal{O}(a)$	-loop	Quantity	Λ_E	X	Y	χ^2/dof	$\Lambda_{\overline{MS}}$
zero	2	r_c	17.42(3)			31	241.8(4)
zero	2	T_c	16.435(4)			695	228.12(5)
zero	2	σ	15.51(2)			70	215.3(3)
zero	3	r_c	17.65(3)			29	245.0(4)
zero	3	T_c	16.693(4)			633	231.68(5)
zero	3	σ	15.75(3)			67	218.5(3)
LO	2	r_c	18.08(5)	0.050(3)		0.59	250.9(7)
LO	2	T_c	17.03(2)	0.0124(3)		266	236.3(2)
LO	2	σ	16.51(6)	0.033(2)		15	229.1(8)
LO	3	r_c	18.30(5)	0.049(3)		0.6	254.0(8)
LO	3	T_c	17.26(2)	0.0117(3)		259	239.5(2)
LO	3	σ	16.73(6)	0.032(2)		15	232.2(8)
NLO	2	r_c	18.05(8)	0.04(2)	0.005(12)	0.7	251(1)
NLO	2	T_c	18.35(6)	0.096(3)	-0.0199(8)	2.1	254.7(8)
NLO	2	σ	17.3(1)	0.097(7)	-0.018(2)	0.39	241(2)
NLO	3	r_c	18.26(8)	0.04(2)	0.007(12)	0.7	253(1)
NLO	3	T_c	18.58(6)	0.094(3)	-0.0196(8)	2.3	257.9(8)
NLO	3	σ	17.6(1)	0.096(7)	-.018(2)	0.39	244(2)

Table 3.12: Fits results for the SU(3) Wilson data using the g_E scheme at both 2- and 3-loops in perturbation theory. The zeroth order fits in $\mathcal{O}(a)$ expansion are included as well as LO and NLO ones. All the Λ values are in MeV.

β	β_c	$a\sqrt{\sigma}$	N_t
Ref	[48]	[31]	[48]
2.2986		0.3667(18)	
	2.2986(6)		4
	2.37136(54)		5
2.3715		0.2879(13)	
2.3726		0.2879(10)	
2.4265		0.2388(9)	
	2.4271(17)		6
	2.5090(6)		8
2.5115		0.1768(8)	

Table 3.13: SU(2) data used to set the scale a.

	β	β_c	$a\sqrt{\sigma}$	N_t	Ref.
SU(4)	10.550		0.3739(15)		[31]
	10.637		0.3254(6)		[31]
		10.63727(53)		5	[49]
	10.65		0.3225(11)		[51]
	10.68		0.3083(13)		[51]
	10.700		0.2977(13)		[31]
	10.75		0.2834(11)		[51]
	10.789		0.2706(8)		[31]
		10.7898(16)		6	[49]
	10.83		0.2566(10)		[51]
	10.870		0.2467(11)		[31]
	10.95		0.2285(7)		[51]
	11.05		0.2077(7)		[51]
	11.085		0.19868(83)		[31]
		11.0880(22)		8	[49]
	11.20		0.1819 (6)		[51]
	11.400		0.15277(72)		[31]
	11.50		0.1417(7)		[51]
SU(5)	16.755		0.3844(21)		[50]
	16.975		0.3034(20)		[50]
	17.27		0.2452(15)		[50]
	17.45		0.2221(17)		[50]
SU(6)	24.350		0.3886(18)		[31]
	24.500		0.3416(18)		[31]
		24.5139(24)		5	[49]
	24.515		0.3385(15)		[31]
	24.670		0.3075(14)		[31]
	24.845		0.2798(11)		[52]
		24.8467(30)		6	[49]
	25.050		0.2520(5)		[52]
	25.452		0.2097(7)		[52]
		25.4782(64)		8	[49]
SU(8)	43.78		0.3758(16)		[52]
	43.85		0.3614(14)		[52]
		43.982(14)		5	[49]
	44.00		0.3413(13)		[52]
	44.35		0.3014(13)		[52]
		44.535(37)		6	[49]
	44.85		0.2597(10)		[52]
		45.654(32)		8	[49]
	45.70		0.2086(8)		[52]

Table 3.14: SU(4), SU(5), SU(6), SU(8) data used to set the scale a.

Also, let's notice the fact that while for $SU(3)$ there is a smooth cross-over between strong and weak coupling, so one would not really know a priori from which value of β a weak coupling expansion in g^2 and a is appropriate, for $SU(N \geq 5)$ there is a first order transition [50] clearly separating the two regimes. This removes the ambiguity of where one might expect a weak coupling expansion to be applicable, and enables us to quantify the importance of $\mathcal{O}(a^2)$ lattice corrections in the large N case.

This data are fitted to eq.(3.8), as in SU(3) case, with all the dependence on N coming from the coefficients of the β-function (eqs.(3.2 & 3.3)). Studying this in detail, we have (at 3-loops and zero-th order in $\mathcal{O}(a)$) from eqs.(3.4 & 3.5),

$$\Lambda_L a(g_0^2) = f_{PT}(g_0^2) = e^{-\frac{1}{2b_0 g_0^2}} \left(b_0 g_0^2\right)^{-\frac{b_1}{2b_0^2}} \left(1 + \frac{1}{2b_0^3}(b_1^2 - b_2^L b_0) g_0^2\right) \tag{3.30}$$

$$\begin{aligned} b_0 &\sim \mathcal{O}(N) \\ b_1 &\sim \mathcal{O}(N^2) \\ b_2^L &\sim \mathcal{O}(N^3). \end{aligned}$$

We can rewrite eq.(3.30) in terms of β as follows:

$$\Lambda a(\beta) \sim e^{-h_0 \beta} \, (\beta/N^2)^{h_1} (1 + \frac{h_2^L}{\beta}) \tag{3.31}$$

where

$$\begin{aligned} h_0 &\sim \mathcal{O}(1/N^2) \\ h_1 &\sim \mathcal{O}(1) \neq f(N) \\ h_2^L &\sim \mathcal{O}(N^2). \end{aligned}$$

From this behaviour we would expect g_0-PT to get worse with N, since the higher loop coefficients grow with N^2. However, we note that β always occurs in eq.(3.31)

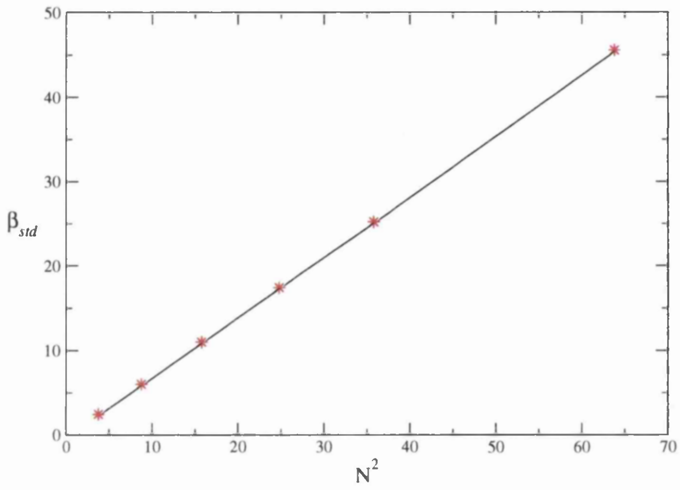

Figure 3.8: Plot of β_{std} against the square of the number of colours, N^2, where β_{std} is the β value where the inverse lattice spacing $a^{-1} \sim 2$ GeV.

with a factor of $1/N^2$. In order to maintain *fixed* lattice spacing then, we require $\beta \sim N^2$. This then means that the g_0-PT will *not* necessarily get worse with N. The relationship $\beta \sim N^2$ is confirmed by the values for β_{std} in Table 3.1. Recall that β_{std} is the β value such that the lattice spacing $a^{-1} \sim 2$ GeV. Plotting β_{std} against N^2 in figure 3.8 confirms to a very high precision the relationship $\beta_{std} \sim N^2$, in accord with what expected for the t'Hooft coupling[9].

We list our results from the fits in Table 3.15 for $N = 2$, and in Table 3.16 for $N = 4, 5, 6, 8$. Where possible, also the NLO fit in $\mathcal{O}(a^n)$ was performed, but sometimes the coefficients and their large errors, made these fits unreliable (see Table 3.16). To convert the lambda in the g_0 scheme's Λ_L to $\Lambda_{\overline{MS}}$, eq.(3.18) has

---

[9] As N varies, we expect [53] that we will need to keep constant the t'Hooft coupling, λ, and its inverse, γ:

$$\lambda(a) \equiv g^2(a)N; \qquad \gamma \equiv \frac{1}{\lambda} = \frac{\beta}{2N^2} \tag{3.32}$$

for a smooth large N limit. Therefore $\beta \sim N^2$.

been used for different N.

In the SU(2) case the best fits were obtained with the NLO (rather than LO) functions. The values for the LO coefficient, $X_{n,\nu}$ and $\Lambda_{\overline{MS}}$ are very similar for both quantities considered.

In the SU(N) case (N>3), the best fits are from LO rather than NLO, since the coefficient $X_{n,\nu}$ generally has a very large error in the NLO fits. This somewhat disappointing fact can be explained by the small range of a^{-1} for these data sets, as mentioned at the beginning of this section. With such a small lever arm, it is natural to assume that it is hard to obtain sensible fits at higher order in the $\mathcal{O}(a^n)$ expansion.

For the best fit results for *all* N, we notice the remarkable fact that the coefficient, $X_{n,\nu}$, is always $\sim 20-25\%$. Also the $\Lambda_{\overline{MS}}$ is very consistently independent of the quantity being considered: for the 3-loop case $\Lambda_{\overline{MS}} \sim 180 - 230\ MeV$. These two facts add weight to the argument that the LDPT fits are correctly reproducing the data.

We graphically depict the quality of the string tension fits in figure 3.9, where the χ^2/dof is plotted for all values of N. The χ^2/dof value for the zero-th order g_0 fit is shown near the middle of the graph, and to the left of this the LO and NLO (g_0) χ^2/dof values are also shown. As can be seen, increasing the number of terms in the a expansion decreases the χ^2/dof value to $\sim \mathcal{O}(1)$. Note that $SU(5)$ is not included in the plot since the small amount of data points available in this case did not allow a reliable investigation (see also table 3.16).

$\mathcal{O}(a)$	-loop	Quantity	Λ_L	X	Y	χ^2/dof	$\Lambda_{\overline{MS}}$
LO	2	T_c	8.89(2)	.098(1)	-	243	176.3(4)
LO	2	σ	9.16(5)	.112(3)	-	29	182(1)
LO	3	T_c	10.04(2)	.093(1)	-	225	198.9(5)
LO	3	σ	10.31(6)	.104(3)	-	28	204(1)
NLO	2	T_c	10.05(6)	.269(7)	-.062(3)	3.9	199(1)
NLO	2	σ	10.4(1)	.27(2)	-.059(6)	1.2	206(3)
NLO	3	T_c	11.30(6)	.260(7)	-.061(3)	3.6	224(1)
NLO	3	σ	11.6(2)	.26(2)	-.056(6)	1.1	230(3)

Table 3.15: Fit results for the SU(2) data in the g_0 scheme, using both LO and NLO in the $\mathcal{O}(a)$ expansion and both 2- and 3-loop perturbation theory. All the Λ values are in MeV.

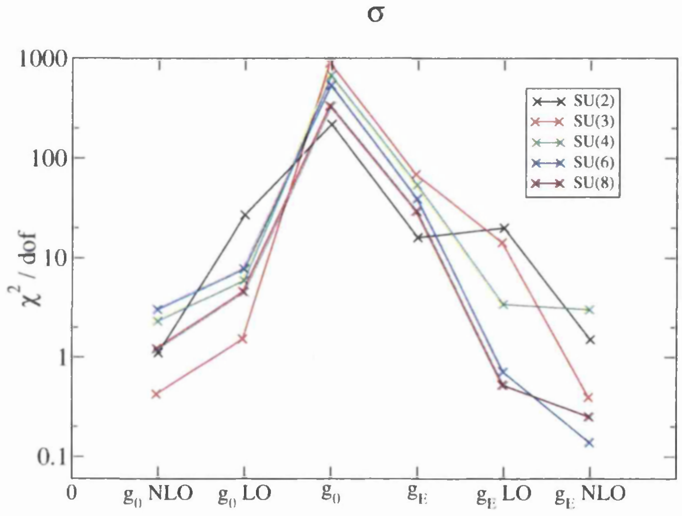

Figure 3.9: Plot of the χ^2/dof obtained in the σ SU(N) data fits in different schemes, using 3-loop PT and up to NLO *Lattice Distorted PT*. The lines connecting the data points are guides for the eye.

3.7 SU(N) in g_E Scheme

Finally, we repeat the g_E scheme analysis performed for the SU(3) data in section 3.5 with the $N \neq 3$ data. Tables 3.17 and 3.18 contain results for the $SU(2)$ and

$\mathcal{O}(a)$	-loop	Quantity	Λ_L	X	Y	χ^2/dof	$\Lambda_{\overline{MS}}$
SU(4)							
LO	2	T_c	5.29(1)	.204(1)	-	32	173.8(4)
LO	2	σ	4.90(1)	.215(1)	-	4.9	160.8(4)
LO	3	T_c	6.41(2)	.198(1)	-	40	210.4(5)
LO	3	σ	5.88(2)	.204(1)	-	5.4	193.1(5)
NLO	2	σ	4.66(4)	.13(1)	.039(7)	2.4	153(1)
NLO	3	σ	5.58(5)	.12(1)	.041(7)	2.3	183(2)
SU(5)							
LO	2	σ	4.55(5)	.242(5)	-	12	159(2)
LO	3	σ	5.54(6)	.231(5)	-	12	193(2)
NLO	2	σ	3.0(3)	-.41(21)	.28(9)	$.6 \times 10^{-5}$	104(11)
NLO	3	σ	3.7(4)	-.40(20)	.26(8)	$.4 \times 10^{-3}$	128(13)
SU(6)							
LO	2	T_c	4.65(2)	.235(2)	-	4.0	167.8(5)
LO	2	σ	4.26(2)	.262(3)	-	7.0	153.7(7)
LO	3	T_c	5.75(2)	.229(2)	-	6.4	207.1(7)
LO	3	σ	5.22(3)	.251(3)	-	7.3	188.2(9)
NLO	2	σ	3.7(1)	.06(5)	.10(2)	3.1	134(4)
NLO	3	σ	4.6(1)	.05(5)	.09(2)	3.0	164(5)
SU(8)							
LO	2	T_c	4.45(5)	.221(4)	-	2.0	166(2)
LO	2	σ	3.97(2)	.239(3)	-	4.0	147.8(9)
LO	3	T_c	5.53(6)	.215(5)	-	2.4	206(2)
LO	3	σ	4.89(3)	.228(3)	-	4.2	182(1)
NLO	2	σ	3.5(1)	.07(5)	.07(2)	1.2	131(5)
NLO	3	σ	4.3(2)	.06(5)	.07(2)	1.2	162(6)

Table 3.16: Fit results for the SU(N) data in the g_0 scheme, using both LO and NLO in the $\mathcal{O}(a)$ expansion and both 2- and 3-loop perturbation theory. All the Λ values are in MeV.

$SU(4), SU(5), SU(6), SU(8)$ fits, respectively. The plaquette values used are from [50] for SU(2) and SU(5), from [50] and [51] for SU(4), and from [52] for SU(6) and SU(8). To convert the lambda in the g_E scheme's Λ_E to $\Lambda_{\overline{MS}}$, eqs.(3.18 & 3.28) have been used as in section 3.5.

As in the g_0 fits (see section 3.6), we concentrate on the LO rather than NLO fits, except for the SU(2) case where we have more data. For all the fits, the $\Lambda_{\overline{MS}}$ values are very stable and no considerable dependence on N is observed.

Again, we graphically depict the quality of the fits in figure 3.9 where the χ^2/dof is plotted for all values of N. The χ^2/dof value for the zero-th order g_E fit is shown near the middle of the graph, and, to the right of this the LO and NLO (g_E) χ^2/dof values are also shown. As can be seen, increasing the number of terms in the a expansion decreases the χ^2/dof value to $\sim \mathcal{O}(1)$ for all N (except for $N = 2$ LO case). This again shows the necessity of introducing $\mathcal{O}(a^n)$ terms in order to obtain sensible fits.

$\mathcal{O}(a)$	-loop	Quantity	Λ_E	X	Y	χ^2/dof	$\Lambda_{\overline{MS}}$
zero	2	T_c	19.70(2)			129	226.8(2)
zero	2	σ	19.85(4)			16	228.5(4)
zero	3	T_c	19.84(2)			130	228.4(2)
zero	3	σ	19.98(4)			16	230.1(4)
LO	2	T_c	19.44(4)	-.008(1)		167	223.8(5)
LO	2	σ	20.0(1)	-.005(3)		21	230(1)
LO	3	T_c	19.56(4)	-.008(1)		166	225.2(5)
LO	3	σ	20.1(1)	-.004(3)		20	232(1)
NLO	2	T_c	20.88(9)	.091(5)	-.027(1)	5	240(1)
NLO	2	σ	21.6(2)	.10(1)	-.027(3)	1.6	248(3)
NLO	3	T_c	21.00(1)	.090(5)	-.027(1)	5	242(1)
NLO	3	σ	21.7(2)	.10(1)	-.026(3)	1.5	250(3)

Table 3.17: Fits results for the SU(2) data using the g_E scheme at both 2- and 3-loops in perturbation theory. These fits were obtained by including various terms in the $\mathcal{O}(a)$ expansion. All the Λ values are in MeV.

3.8 Conclusions

In this chapter, the running coupling on the lattice was discussed. We emphasized how the dependence of the lattice spacing a on the lattice coupling $g_0^2(a)$ needs to incorporate lattice spacing corrections in addition to the perturbative expression that one obtains in the continuum. The simple perturbative interpolation will not fit the Monte Carlo data without these $\mathcal{O}(a^n)$ lattice corrections. This has been shown fitting quenched data to the expression of the running coupling (3.4) with and without $\mathcal{O}(a^n)$ terms.

In the $SU(3)$ case, different observables have been considered, as well as different gauge actions. We drew similar conclusions in all the cases where enough data were available. We gave an estimate of the $SU(3)$ $\Lambda_{\overline{MS}}$ from the fit of Wilson data to the fitting function at NLO in the $\mathcal{O}(a^n)$ expansion, using the 3-loop expression of the β-function:

$$\Lambda_{\overline{MS}}^{N_f=0} = 217 \pm 21 \ \ MeV.$$

For the Wilson case, in order to improve the convergence of the series in g_0, we also considered the case when the lattice coupling is replaced by different choices of renormalized coupling, with particular focus on the g_E renormalized scheme. We observed a reduction of the discrepancy between Monte Carlo data and perturbative scaling, but the quality of the fit is reasonably good only after including $\mathcal{O}(a^n)$ terms.

Finally, we extended our analysis to $SU(N)$ Wilson data for $N \neq 3$, performing again fits for different observables and at different order in the lattice spacing expansion. From the comparison of the results obtained in the lattice scheme g_0 and in the g_E scheme, we drew similar conclusions to the $SU(3)$ case. Also, the $\Lambda_{\overline{MS}}$ values obtained at different N are consistent and hardly dependent on the quantity and the N value considered.

The fact that the SU(N) fits match so well with lattice distorted perturbation theory for all values of N is not surprising given the similarity of the data. This can be seen in figure 3.10, where we plot a^{-1} obtained from the string tension against $3^2(\beta/N^2)$ for all N values, i.e. the ratio β/N^2 normalized relative to the SU(3) data (note: the inverse of the t'Hooft coupling is $\gamma = 1/g^2N = \beta/2N^2$). As can be seen the data lie on curves which run parallel to each other at different N values and the curves represent the LDPT fits at NLO for $SU(2)$ and $SU(3)$ and LO for other N, i.e. our best fits, as previously motivated.

Another way of picturing the success of this approach is displayed in figure 3.11. Here is the plot of the ratio $a_\sigma^{-1}/a_{PT}^{-1}$ for all values of N against a_{PT}^2. a_σ^{-1} is defined from the Monte Carlo data for the string tension as before, a_{PT} is defined in eq.(3.4), $a_{PT}^{-1} = \Lambda_L / f_{PT}(g_0^2)$, and the 3-loop formula for f_{PT} has been used here. Clearly, if Monte Carlo data were well described by the 3-loop asymptotic scaling formula, eq.(3.4), the ratio here plotted would be equal to 1. The deviation from one is precisely the discrepancy being studied in this work: moreover the plot shows that this discrepancy agrees well with $\mathcal{O}(a^2)$, as expected.

In conclusion, all our investigations support the validity of the Lattice-Distorted Perturbation Theory method. This approach leads to a remarkable consistency both in the fitted Λ parameters and in the size of the $\mathcal{O}(a^n)$ corrections.

The lack of perturbative scaling is probably due to a mixture of the two effects here considered, the poor convergence of the g_0 perturbative series and the presence of cut-off effects due to the finiteness of the lattice spacing. However, we have given strong arguments to support the claim that the lattice artefacts represent the dominant effect.

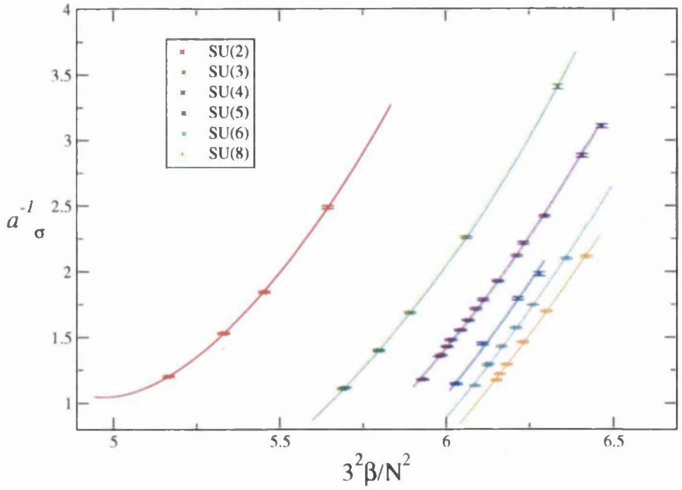

Figure 3.10: Plot of the SU(N) a^{-1} from the string tension for all values of N against the inverse of the t'Hooft coupling (note $\gamma \equiv= \frac{1}{\lambda} = \beta/2N^2$), normalised relative to the SU(3) data. The curves represent the LDPT fits at NLO for $SU(2)$ and $SU(3)$ and LO for other N, i.e. our best fits, as motivated in the text.

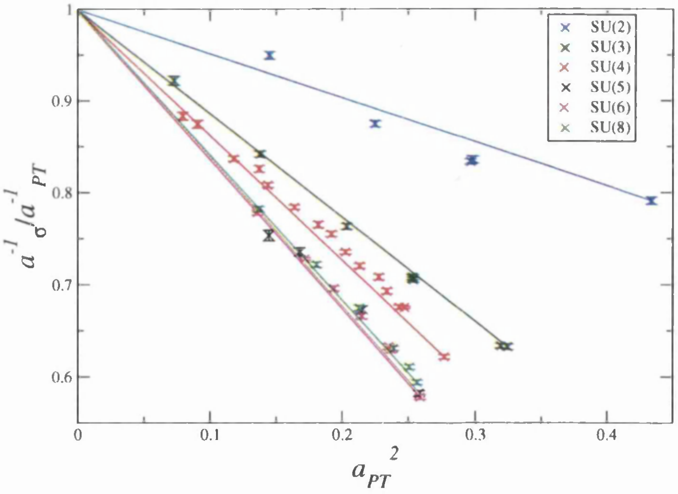

Figure 3.11: Plot of the ratio $a_\sigma^{-1}/a_{PT}^{-1}$ for all values of N against a_{PT}^2, where $a_{PT}^{-1} = \Lambda_L/f_{PT}(g_0^2)$, and the 3-loop expression of f_{PT} has been used. The straight lines, connecting the point (0,1) with the last data point, represent a guide for the eye.

$\mathcal{O}(a)$	-loop	Quantity	Λ_L	X	Y	χ^2/dof	$\Lambda_{\overline{MS}}$
			SU(4)				
zero	2	T_c	15.755(5)	-	-	245	233.45(7)
zero	2	σ	14.44(1)	-	-	58	213.9(2)
zero	3	T_c	16.139(5)	-	-	217	239.14(7)
zero	3	σ	14.78(1)	-	-	54	219.0(2)
LO	2	T_c	16.48(3)	.022(1)	-	41	244.1(5)
LO	2	σ	15.39(4)	.040(1)	-	3.5	228.0(5)
LO	3	T_c	16.83(4)	.021(1)	-	40	249.4(5)
LO	3	σ	15.71(4)	.039(1)	-	3.4	232.8(6)
NLO	2	σ	15.59(8)	.061(7)	-.007(3)	3	231(1)
NLO	3	σ	15.91(8)	.058(7)	-.007(3)	3	236(1)
			SU(5)				
zero	2	σ	13.67(4)	-	-	26	208.7(7)
zero	3	σ	14.07(4)	-	-	24	214.9(7)
LO	2	σ	14.7(1)	.038(4)	-	1.8	224(2)
LO	3	σ	15.1(1)	.036(4)	-	1.9	230(2)
NLO	2	σ	13.8(5)	-.03(5)	.019(12)	.90	211(8)
NLO	3	σ	14.2(5)	-.04(5)	.020(12)	.91	217(8)
			SU(6)				
zero	2	T_c	15.317(8)	-	-	127	237.8(1)
zero	2	σ	13.52(2)	-	-	43	209.9(3)
zero	3	T_c	15.820(9)	-	-	108	245.6(1)
zero	3	σ	13.95(2)	-	-	39	216.6(3)
LO	2	T_c	15.98(4)	.024(2)	-	12	248.1(7)
LO	2	σ	14.36(6)	.042(2)	-	.79	222.9(9)
LO	3	T_c	16.45(5)	.022(2)	-	11	255.4(7)
LO	3	σ	14.78(6)	.040(3)	-	.71	229.5(9)
NLO	2	σ	14.7(2)	.07(2)	-.010(5)	.15	228(3)
NLO	3	σ	15.1(2)	.07(2)	-.010(5)	.14	235(3)
			SU(8)				
zero	2	T_c	15.23(3)	-	-	14	240.3(5)
zero	2	σ	13.09(2)	-	-	33	206.7(3)
zero	3	T_c	15.78(4)	-	-	12	249.0(6)
zero	3	σ	13.57(2)	-	-	29	214.1(3)
LO	2	T_c	16.0(1)	.023(4)	-	.02	252(2)
LO	2	σ	13.94(7)	.032(2)	-	.57	220(1)
LO	3	T_c	16.5(1)	.021(4)	-	.01	260(2)
LO	3	σ	14.39(7)	.030(2)	-	.52	227(1)
NLO	2	σ	14.2(2)	.06(2)	-.007(5)	.25	224(4)
NLO	3	σ	14.6(2)	.05(2)	-.006(5)	.25	231(4)

Table 3.18: Fits results for the SU(N) data using the g_E scheme at both 2- and 3-loops in perturbation theory. These fits were obtained by including various terms in the $\mathcal{O}(a)$ expansion. All the Λ values are in MeV.

Chapter 4

Nucleons from 2+1 DWF

4.1 Baryons

The baryon spectrum is a good place to test lattice gauge theory, in particular for those lowest lying states very well determined by experiments. Furthermore, LGT can be a powerful predictive tool for those baryonic states whose experimental values are not known very accurately.

Baryons are sufficiently complex states to reveal physics hidden in the mesonic sector, but at the same time they are simple systems of three quarks, obeying the Pauli exclusion principle and giving the so called baryon octet and decuplet. Their total state function is anti-symmetric under interchange of any two equal-mass quarks (up and down quarks in the commonly considered limit of isospin symmetry). We can then write the baryon state function as

$$|qqq>_A = |colour>_A \times |space>_S \times |spin, flavour>_S, \tag{4.1}$$

where the subscripts S and A indicate symmetry or antisymmetry under interchange of two equal-mass quarks. The colour part of the baryon state function is an $SU(3)$ singlet, a completely antisymmetric state of the three colours; the space part is symmetric when considering lowest lying states at $L = 0$, and consequently the product of spin and flavour parts has to be symmetric too. When the total spin of the baryon is $S = J = \frac{3}{2}$, then the spin part is clearly symmetric, and the flavour one must be symmetric too. There are 10 possible combinations of three quarks giving such a total state function: they form the baryon decuplet. When the total spin is $S = J = \frac{1}{2}$, then the product of spin and flavour state functions has to be symmetric, but they are not necessarily separately symmetric (mixed symmetry): in this case we have the baryon octet.

The nucleons, proton and neutron, are members of the ground state octet of spin= $\frac{1}{2}$ baryons. The calculation of the nucleon mass is a particularly good test for lattice gauge theory since its value can be compared with the one very accurately determined by experiments.

In this chapter we present preliminary results of the lowest lying, valence degenerate states with $J^P = \frac{1}{2}^{\pm}$, N and N^*, on two different volumes at a single lattice spacing with $2+1$ dynamical flavours. The good chiral properties of the domain wall fermions formulation are used in order to reproduce the large mass splitting between the nucleon $N(939)$ and its parity partner $N(1535)$. As discussed previously, domain wall fermions have only mild chiral symmetry breaking, which, in particular for masses $\mathcal{O}(1)$ GeV in the chiral limit, can be approximated by a constant mass term. This study of nucleon masses is part of the ongoing baryon physics project by the RBC-UKQCD collaboration.

4.2 Calculation Details

In this work we consider nucleon correlators with different smeared operators in order to improve statistical accuracy and systematics. The correlators can also differ in the interpolating operators used to reproduce the desired baryonic state. Before giving details of our analysis then, we classify these correlators.

We can essentially divide our data into *type A* and *type B*, due to the different methods used to produce them. The type A correlators were generated in the UK using both the interpolating operators in eq.(2.102). In this case, only the positive parity state was produced: this means that both the masses of the positive and negative parity partners, N and N^*, were determined by a fit to the first correlator in eq.(2.105) which, in our case of anti-periodic boundary conditions, becomes

$$C_N^+(t) = A_+ e^{M_N t} + A_- e^{-M_{N^*}(T-t)}. \tag{4.2}$$

The type B correlators were generated in the US. The interpolating operators used to produce them are $N_1 = N_1^+$ in the first line of (2.102) and (dropping the Dirac indices) $N'^+(x) = \epsilon_{abc}(u^{T,a}(x)\mathcal{C}d^b(x))\gamma_5 u^c(x)$. As previously mentioned, this second operator has a poor overlap with the nucleon ground state, so for the nucleon only the N_1 actually contributes. For the N^* instead, the corresponding negative-parity interpolating operators of both N_1 and N' are considered[1]:

$$\begin{aligned} N_1^-(x) &= \gamma_5 N_1^+(x) = \epsilon_{abc}(u^{T,a}(x)\mathcal{C}\gamma_5 d^b(x))\gamma_5 u^c(x), \\ N'^-(x) &= \gamma_5 N'^+(x) = \epsilon_{abc}(u^{T,a}(x)\mathcal{C}d^b(x))u^c(x). \end{aligned} \tag{4.4}$$

The type B data have both the positive- and negative-parity parts. Therefore, the mass of both N and N^* are determined by a simultaneous fit to both the

---

[1] Note that for instance

$$\mathcal{P}N_1^-(x_4,\vec{x})\mathcal{P} = -\gamma_4 N_1^-(x_4,-\vec{x}). \tag{4.3}$$

correlators in eq.(2.105) which, for anti-periodic boundary conditions, become

$$\begin{aligned} C_i^+(t) &= A_+e^{-M_N t} + A_-e^{-M_{N^*}(T-t)} \\ C_i^-(t) &= -A_-e^{-M_{N^*}t} - A_+e^{-M_N(T-t)}. \end{aligned} \tag{4.5}$$

Note that the subscript i corresponds to the N_1 operator for the nucleon and to both N_1, N' for the N^*. Note also that according to eq.(2.91), the amplitude A in eqs.(4.2) and (4.5) will be given for instance by

$$A_{LL} = A_L \dot{A}_L \tag{4.6}$$

in the LL correlator case, or

$$A_{GL} = A_G \dot{A}_L \tag{4.7}$$

in the GL correlator case.

4.3 Simulation Parameters

The analysis was performed on $2+1$ flavours DWF ensembles generated jointly by the RBC and UKQCD collaborations. Two lattice volumes were studied, $16^3 \times 32$ and $24^3 \times 64$. The simulations used the Iwasaki gauge action with $\beta = 2.13$ and the domain wall fermion quark action with the fifth dimension fixed to $L_s = 16$ and the domain wall height set to $M_5 = 1.8$. The fixed lattice spacing of $a^{-1} = 1.62(4)$ GeV gives a corresponding spatial volume of $(1.9\ fm)^3$ and $(2.9\ fm)^3$ for the small and large volume respectively. We first check the possible finite volume effects on the nucleon and N^* states by comparing the results obtained from the two different volumes. For the sake of reproducing the nucleon states, it is more advantageous for us to obtain results from the larger volume simulations, as we will show in the following. At each volume, three sets of configurations were generated with a light isodoublet with masses $m_{ud} = m_{sea} = 0.01, 0.02, 0.03$, and a fixed approximate strange quark mass, $m_s = 0.04$. All masses are in dimensionless lattice units. The ensembles were generated using the RHMC algorithm and its implementations [19]. More details of the ensembles can be found in [54] and [55].

4.4 Setting the Lattice Scale

The determination of the lattice scale is not part of this work. Therefore in this section we will only recall the different methods that have been used to set the lattice scale. The small lattice calculations can be found in [54]. Here is a summary of the values obtained.

The determination of the lattice scale from the mass of the vector meson ρ is one of the methods employed. A partially quenched linear fit to the values of m_V was performed, using the following phenomenological form:

$$m_V = A(m_{sea} + m_{res}) + B(m_1 + m_2 + 2m_{res}) + C, \tag{4.8}$$

where m_1 and m_2 denote the masses of the two valence quarks that make up the mesons. Setting $m_1 = m_2 = m_{sea} = -m_{res}$ gives the ρ mass in the chiral limit, from which the lattice scale was found to be

$$a^{-1}|_\rho = 1.61(3)\ GeV. \tag{4.9}$$

The lattice scale was also determined from the static quark potential using the Coulomb gauge method [56]. Taking $r_0 = 0.5\ fm$, the lattice scale was determined to be

$$a^{-1}|_{r_0} = 1.63(5)\ GeV. \tag{4.10}$$

A preliminary analysis of this calculation was reported in [57] and a more detailed analysis is the subject of another paper in progress. The third method used for determining the lattice scale is the "method of lattice planes" [33], already briefly described in section 3.3. Here a chiral interpolation in the valence quark sector rather than extrapolation is required. Then a linear extrapolation in the sea quark mass to the chiral limit, $m_{sea} = -m_{res}$, gave

$$a^{-1}|_{latticeplane} = 1.62(5)\ GeV. \tag{4.11}$$

All these methods gave consistent results for the lattice scale. The same approach as in the small volume simulations was adopted in the large volume case, and several methods were used to determine the lattice scale. More details will appear in the outcoming paper [55]: the updated values of the lattice scale from the different methods are consistent with the results from the small volume analysis. Therefore the average of the above values was taken as central value, and an average of their statistical errors as the error. This gives

$$a^{-1} = 1.62(4)\ GeV \tag{4.12}$$

which will be used whenever a lattice scale is needed through this work, and the errors will be propagated accordingly by quadrature. In physical units, it implies a lattice spacing of $a = 0.122(4)\ fm$.

4.5 Data and Analysis

This work considers degenerate nucleons, with all three valence quarks having the same mass. In some cases only unitary data points are available, i.e. only correlators composed of valence quarks with masses equal to the quark mass in the sea[2], $m_{val} = m_{sea}$; for other correlators several valence masses are available for the same sea quark, and we have both unitary and partially quenched points. To improve statistics, correlators were oversampled and averaged into bins whose size depends on the Monte Carlo time separation between measurements. Multiple sources per configuration on different time-planes are used in order to increase statistics and reduce the fluctuations within the gauge configurations. The correlation functions are averaged over the different source locations before the analysis is performed. As already mentioned, several different types of smearing are also used to improve the signal. Note that a baryon correlator composed of just quark propagators with a (hydrogen-like) wall source and a local sink will be denoted as (HL) WL for brevity, instead of (HL-HL-HL) WL-WL-WL. When the correlator is Gaussian smeared at source we will write GL, when both source and sink are Gaussian smeared we will have a GG correlator. Finally a nucleon composed of only local, unsmeared quark fields is denoted simply as LL. For all the measurements, anti-periodic boundary conditions were applied to obtain the quark propagators.

Table 4.1 lists all the data used for both the volumes, specifying the correlator type, as explained in the previous section, the smearing, the range of measurements and the number of sources. Note the wider range of type A measurements for the $am_{sea} = 0.03$ ensemble in the small volume, $16^3 \times 32$: it comes from a subsequent extension of the ensemble performed using an implementation of RHMC algorithm. The two RHMC versions were compared and studied in detail in [54]. Here we performed tests to see how the nucleon mass varies when the original ensemble,

---

[2] Note that in our case of $2 + 1$ flavours, the dynamical quark can also have the mass of the strange quark, so that unitary points include the $m_{val} = 0.04$ case.

$500-4020$, or the extended one, $500-7600$, were considered. In Table 4.2, the masses from a simultaneous fit to the correlator LL, GL, GG are shown for the different cases: the original ensemble is indicated as $RHMC1$, while the extended one as $RHMC1+RHMC2$. We concluded that the data generated from the two algorithms can be combined and considered as a unique set of data. However, for our purpose of performing simultaneous fits to all the available correlators, we will consider the range of measurements common to the WL correlator, i.e the original ensemble $RHMC1$.

m_{sea}	type	V	m_{val}	N_{traj}	Δ	N_{meas}	N_{src}	smearing
0.01	A	$16^3 \times 32$	0.01 0.04	500-4015	10	352	4	LL GL GG
	B	$16^3 \times 32$	0.01 0.02 0.03 0.04	500-4015	5	704	2	WL
0.02	A	$16^3 \times 32$	0.02 0.04	500-4045	10	355	4	LL GL GG
	B	$16^3 \times 32$	0.01 0.02 0.03 0.04	500-4045	5	710	2	WL
0.03	A	$16^3 \times 32$	0.03 0.04	500-7600	10	710	2	LL GL GG
	B	$16^3 \times 32$	0.01 0.02 0.03 0.04	500-4015	5	704	2	WL
0.01	A	$24^3 \times 64$	0.01 0.04	800-4060	10	327	2	LL GL GG
	B	$24^3 \times 64$	0.005 0.01 0.02 0.03 0.04	1500-3860	40	60	2	BL
	B	$24^3 \times 64$	0.01	1500-3860	40	60	4	GL GG
0.02	A	$24^3 \times 64$	0.02 0.04	1600-3610	20	101	2	LL HL
	B	$24^3 \times 64$	0.005 0.01 0.02 0.03 0.04	1520-3600	40	53	2	BL
	B	$24^3 \times 64$	0.02	1800-3600	40	46	4	GL GG
0.03	A	$24^3 \times 64$	0.03 0.04	1000-3060	20	104	2	LL HL
	B	$24^3 \times 64$	0.005 0.01 0.02 0.03 0.04	900-3060	40	55	2	BL
	B	$24^3 \times 64$	0.03	1020-3060	40	52	4	GL GG

Table 4.1: Measurement parameters for all the correlation functions used for the three ensembles in each of the lattice volumes. V is the space-time volume of the lattice, N_{traj} is the lowest to highest trajectory analysed with Δ the separation between measurements in molecular dynamics time unit. N_{src} is the number of different sources used for each set of measurements.

As we will see from the effective masses plots in next sections, different source operators have different degrees of overlap with excited states, and hence the mini-

Data	N_{meas}	M_N	bin size
RHMC1	70	.910(9)	10
RHMC1+RHMC2	70	.907(7)	20
RHMC1+RHMC2	140	.907(6)	10

Table 4.2: Nucleon masses for the $m_{sea} = m_{val} = 0.03$ small volume case, obtained by a simultaneous fit to the LL, GL and GG data. Shown are the values obtained by considering the original set of measurements, $500-4020$, indicated as $RHMC1$, and the extended one, $500-7600$, indicated as $RHMC1 + RHMC2$, where the second part is obtained using an implementation of the original algorithm. The second and third rows differ in the bin size.

mum time slice that should be included in each fit may differ. In order to determine a proper fit range, $[t_{min}, t_{max}]$, for the nucleon and its parity partner N^*, we first look at the effective masses, eq.(2.106), and choose the minimum time slice in the fit range to be the onset of the plateau. Once a first choice of the fit range is set, the more rigorous test to determine the best fit range is to check how the mass obtained from the fit and the resulting χ^2/dof vary with the fit range. Since the fits are less sensitive to the maximum time slice used, we fixed the upper bound, t_{max}, and investigated the variations with respect the lower bound, t_{min}. Normally, we repeated the fits moving t_{min} a time slice closer to the origin (i.e. $[8, 11] \to [7, 11]$), then one farther (i.e. $[8, 11] \to [9, 11]$). In this way, we checked that shifting the fit ranges in either direction by one time slice does not change either mass or χ^2/dof significantly. However, our final choice of time ranges is the one which minimizes the uncorrelated χ^2/dof, where the χ^2 is simply weighted by the statistical errors on the data points.

Since the χ^2 from the uncorrelated fits cannot serve as the measure of goodness of the fits, as a check, we also performed correlated fits to each individual correlator separately to obtain a fit range which gives a reasonable χ^2/dof, based on the criteria explained above. We checked that for a single correlator the correlated and uncorrelated fits give consistent results. However, due to the small number of configurations, in order to better estimate the parameters, we have to fit to multiple correlators (see section 4.9.1). For such simultaneous fits, typically to ten or twelve correlators, the number of data to fit and the number of parameters in the fit increase, so that the relation $N_{params} << N_{data} << N_{cfgs}$ cannot be satisfied. Note N_{data} gives the dimension of the covariance matrix and our typical number of measurements, N_{cfgs}, is not large enough to resolve a covariance matrix of this size. Therefore, all the simultaneous fits we performed were uncorrelated.

4.6 $24^3 \times 64$: fits

Tables 4.3, 4.4 and 4.5 show the nucleon masses obtained from fits to each correlation function available in the large volume case for the $m_{sea} = 0.01,\ 0.02,\ 0.03$ ensembles respectively. The symmetric error quoted is the jackknife error (section 2.13.1). The fit range, chosen as explained in the previous section, is quoted for each fit, as well as the corresponding uncorrelated χ^2/dof. In the third column the correlator type is specified: $g5$ and $g45$ correspond to the $\Gamma = \gamma_5$ and $\Gamma = \gamma_4\gamma_5$ interpolating operators respectively, while the $+$ and $-$ indicate the positive- and negative-parity part of the corresponding correlator. Since the spatial extent of the source in the wall smeared operators is 16^3, so that it covers only a portion of the spatial volume of the larger lattice, it is more appropriate now referring to the correlator as 'box-local', BL, instead of wall-local. Note also that we called $GL2$ and $GG2$ the type B correlators because they have a different smearing radius compared to the type A correlators, which are called simply GL and GG.

Figures 4.1, 4.2 and 4.3 show the effective masses obtained for each ensemble for the unitary points $m_{val} = m_{sea}^{light}$. Note that the larger variety of data is available when the valence is equal to the light dynamical quarks, i.e. $m_{val} = 0.01, 0.02, 0.03$ for the three ensembles respectively: this is why in the following our analysis will focus on these sets of data. Note that the negative-parity part of the type B correlators were omitted in the plots for clarity.

In the same way we present the masses obtained for N^* for the three different ensembles in Tables 4.6, 4.7 and 4.8, and the effective mass plots corresponding to $m_{val} = m_{sea}^{light}$ are shown in figures 4.4, 4.5 and 4.6. The correlator indicated as BL' in the tables and plots corresponds to the interpolating operator N'^{-} in eq.(4.4). It is clear that the mass of the negative parity partner of the nucleon can be less well determined due to the poor signal. In particular for the type A correlators, where only the contribution from the backward mover of the positive parity correlator can be considered, the signal is sometimes very poor and only a very tiny fit range can be considered.

In general, the effective masses from LL correlators typically have later approaches to plateaus and, in particular in the N^* case, sometimes it is not even possible to set an onset, so we are left with fewer time slices to perform the fits. However, clear improvement is found going from the LL to the GG correlators for instance. The symbol × in the right-most column in Tables 4.6, 4.7 and 4.8 indicates the data which will not be included in the simultaneous fits, as explained in more detail in section 4.9.1.

m_{sea}	m_{val}	correlator	fit range	M_N	χ^2/dof
0.01	0.005	BL+	6-11	0.679(17)	0.09
0.01	0.005	BL-	53-58	0.684(16)	0.04
0.01	0.01	LL-g5	10-15	0.729(24)	0.03
0.01	0.01	LL-g45	10-15	0.731(30)	0.04
0.01	0.01	GL-g5	8-14	0.721(10)	0.03
0.01	0.01	GL-g45	8-14	0.729(15)	0.03
0.01	0.01	GG-g5	6-14	0.717(8)	0.08
0.01	0.01	GG-g45	5-13	0.727(10)	0.07
0.01	0.01	BL+	6-11	0.722(12)	0.12
0.01	0.01	BL-	53-58	0.718(10)	0.03
0.01	0.01	GL2+	5-12	0.726(10)	0.02
0.01	0.01	GL2-	52-59	0.717(10)	0.09
0.01	0.01	GG2+	4-14	0.720(10)	0.26
0.01	0.01	GG2-	50-60	0.721(13)	0.14
0.01	0.02	BL+	7-10	0.796(8)	0.03
0.01	0.02	BL-	54-57	0.790(9)	0.005
0.01	0.03	BL+	7-10	0.859(6)	0.03
0.01	0.03	BL-	54-57	0.854(9)	0.009
0.01	0.04	LL-g5	10-14	0.939(9)	0.04
0.01	0.04	LL-g45	10-14	0.935(9)	0.03
0.01	0.04	GL-g5	7-13	0.934(5)	0.03
0.01	0.04	GL-g45	7-13	0.936(6)	0.02
0.01	0.04	GG-g5	6-13	0.931(5)	0.03
0.01	0.04	GG-g45	6-13	0.937(5)	0.04
0.01	0.04	BL+	8-13	0.933(6)	0.05
0.01	0.04	BL-	51-56	0.910(8)	0.07

Table 4.3: Fit results for the nucleon mass from all the correlators in the 0.01 ensemble, $24^3 \times 64$ lattice. All the masses are in lattice units.

m_{sea}	m_{val}	correlator	fit range	M_N	χ^2/dof
0.02	0.005	BL+	6-12	0.702(23)	0.03
0.02	0.005	BL-	52-58	0.712(26)	0.01
0.02	0.01	BL+	6-12	0.745(15)	0.06
0.02	0.01	BL-	52-58	0.745(15)	0.04
0.02	0.02	LL-g5	8-11	0.828(18)	0.002
0.02	0.02	LL-g45	8-11	0.820(20)	0.008
0.02	0.02	HL-g5	6-12	0.814(7)	0.02
0.02	0.02	HL-g45	6-12	0.798(7)	0.01
0.02	0.02	BL+	5-12	0.816(8)	0.11
0.02	0.02	BL-	52-59	0.813(8)	0.03
0.02	0.02	GL2+	5-12	0.802(6)	0.02
0.02	0.02	GL2-	52-59	0.806(9)	0.11
0.02	0.02	GG2+	5-12	0.788(9)	0.05
0.02	0.02	GG2-	52-59	0.802(12)	0.15
0.02	0.03	BL+	6-12	0.883(8)	0.05
0.02	0.03	BL-	52-58	0.876(8)	0.02
0.02	0.04	LL-g5	9-11	0.956(15)	0.006
0.02	0.04	LL-g45	9-11	0.951(17)	0.02
0.02	0.04	HL-g5	7-12	0.940(6)	0.01
0.02	0.04	HL-g45	8-12	0.932(8)	0.008
0.02	0.04	BL+	6-12	0.942(7)	0.03
0.02	0.04	BL-	52-58	0.937(7)	0.01

Table 4.4: Fit results for the nucleon mass from all the correlators in the 0.02 ensemble, $24^3 \times 64$ lattice. All the masses are in lattice units.

m_{sea}	m_{val}	correlator	fit range	M_N	χ^2/dof
0.03	0.005	BL+	5-10	0.720(16)	0.19
0.03	0.005	BL-	54-59	0.733(19)	0.11
0.03	0.01	BL+	5-10	0.755(10)	0.14
0.03	0.01	BL-	54-59	0.768(12)	0.05
0.03	0.02	BL+	8-14	0.815(15)	0.08
0.03	0.02	BL-	50-56	0.839(17)	0.03
0.03	0.03	LL-g5	9-17	0.882(11)	0.03
0.03	0.03	LL-g45	9-17	0.884(13)	0.06
0.03	0.03	HL-g5	6-15	0.886(6)	0.17
0.03	0.03	HL-g45	6-14	0.887(7)	0.04
0.03	0.03	BL+	5-14	0.884(7)	0.03
0.03	0.03	BL-	50-57	0.906(8)	0.05
0.03	0.03	GL2+	6-13	0.907(9)	0.04
0.03	0.03	GL2-	51-58	0.903(11)	0.02
0.03	0.03	GG2+	6-14	0.890(10)	0.28
0.03	0.03	GG2-	50-58	0.894(17)	0.07
0.03	0.04	LL-g5	10-17	0.940(11)	0.05
0.03	0.04	LL-g45	10-17	0.946(12)	0.02
0.03	0.04	HL-g5	7-15	0.950(6)	0.06
0.03	0.04	HL-g45	7-14	0.952(7)	0.04
0.03	0.04	BL+	5-11	0.944(6)	0.02
0.03	0.04	BL-	53-59	0.966(7)	0.11

Table 4.5: Fit results for the nucleon mass from all the correlators in the 0.03 ensemble, $24^3 \times 64$ lattice. All the masses are in lattice units.

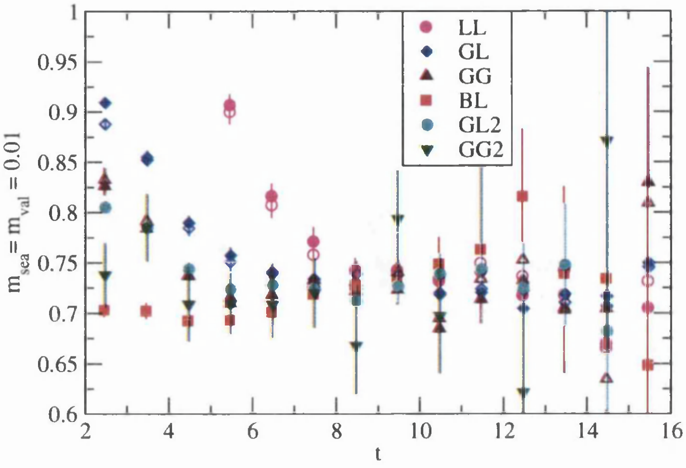

Figure 4.1: Effective masses for the nucleon obtained from the fits to the $m_{sea} = m_{val} = 0.01$ correlators, in the $24^3 \times 64$ volume case. Note that the full symbols for the LL, GL and GG correlators correspond to the γ_5 interpolating operator, while the empty symbols correspond to $\gamma_4\gamma_5$.

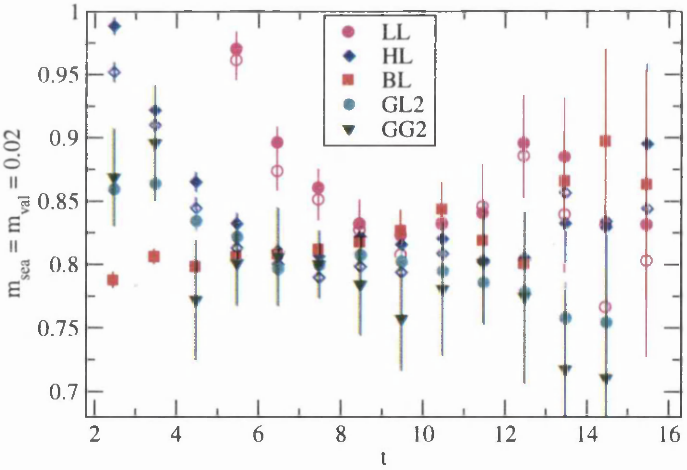

Figure 4.2: Effective masses for the nucleon obtained from the fits to the $m_{sea} = m_{val} = 0.02$ correlators, in the $24^3 \times 64$ volume case. Note that the full symbols for the LL and HL correlators correspond to the γ_5 interpolating operator, while the empty symbols correspond to $\gamma_4\gamma_5$.

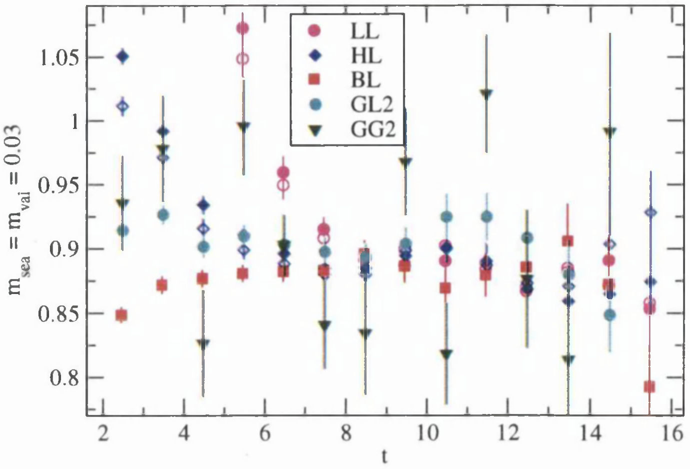

Figure 4.3: Effective masses obtained for the nucleon from the fits to the $m_{sea} = m_{val} = 0.03$ correlators, in the $24^3 \times 64$ volume case. Note that the full symbols for the LL and HL correlators correspond to the γ_5 interpolating operator, while the empty symbols correspond to $\gamma_4\gamma_5$.

4.7 $16^3 \times 32$: fits

The same kind of analysis was performed for the small volume ensembles in order to be able to estimate finite volume effects, as explained in more detail in section 4.8.

Tables 4.9, 4.10 and 4.11 show the nucleon masses obtained from fits to each correlation function available in the small volume case, for the $m_{sea} = 0.01,\ 0.02,\ 0.03$ ensembles respectively. The symmetric error quoted is the jackknife error. The tables have the same structure as explained in section 4.6.

Figures 4.7, 4.8 and 4.9 show the effective masses plots obtained for each ensemble for $m_{val} = m_{sea}^{light}$.

In the same way we present the masses obtained for N^* for the three different ensembles in Tables 4.12, 4.13 and 4.14, and the corresponding effective masses in

m_{sea}	m_{val}	correlator	fit range	M_{N^*}	χ^2/dof	
0.01	0.005	BL-	4-7	0.927(62)	0.23	
0.01	0.005	BL+	57-60	0.935(66)	0.12	
0.01	0.005	*BL′*	3-7	1.108(71)	0.11	
0.01	0.01	LL-g5	55-57	1.033(95)	0.06	×
0.01	0.01	LL-g45	56-57	1.086(106)	-	×
0.01	0.01	GL-g5	55-58	0.978(41)	0.36	
0.01	0.01	GL-g45	55-57	1.080(160)	0.002	
0.01	0.01	GG-g5	56-60	1.043(27)	0.03	
0.01	0.01	GG-g45	57-60	1.114(41)	0.04	
0.01	0.01	BL-	4-7	0.985(37)	0.16	
0.01	0.01	BL+	57-60	0.975(41)	0.11	
0.01	0.01	*BL′*	3-7	1.033(33)	0.01	
0.01	0.01	GL2-	4-7	1.028(33)	0.06	
0.01	0.01	GL2+	57-60	1.099(84)	0.01	
0.01	0.01	GG2-	6-8	0.974(106)	0.01	
0.01	0.01	GG2+	56-58	0.977(177)	0.99	
0.01	0.02	BL-	4-7	1.061(23)	0.06	
0.01	0.02	BL+	57-60	1.048(24)	0.06	
0.01	0.02	*BL′*	4-7	1.046(23)	0.005	
0.01	0.03	BL-	4-7	1.124(17)	0.04	
0.01	0.03	BL+	57-60	1.111(18)	0.05	
0.01	0.03	*BL′*	4-8	1.101(18)	0.03	
0.01	0.04	LL-g5	54-56	1.232(40)	0.005	×
0.01	0.04	LL-g45	54-56	1.221(48)	0.005	×
0.01	0.04	GL-g5	53-56	1.181(34)	0.15	
0.01	0.04	GL-g45	54-56	1.158(36)	0.001	
0.01	0.04	GG-g5	54-57	1.167(27)	0.07	
0.01	0.04	GG-g45	54-56	1.175(54)	0.06	
0.01	0.04	BL-	4-7	1.181(15)	0.02	
0.01	0.04	BL+	57-60	1.168(14)	0.05	
0.01	0.04	*BL′*	4-8	1.156(15)	0.08	

Table 4.6: Fit results for the N^* mass from all the correlators in the 0.01 ensemble, $24^3 \times 64$ lattice. All the masses are in lattice units.

figures 4.10, 4.11 and 4.12. Again, the correlator indicated as WL' in tables and plots corresponds to the interpolating operator N'^- in eq.(4.4), which contributes

m_{sea}	m_{val}	correlator	fit range	M_{N^*}	χ^2/dof	
0.02	0.005	BL-	3-7	1.220(54)	1.5	
0.02	0.005	BL+	57-61	1.072(55)	0.13	
0.02	0.005	BL'	3-7	1.211(115)	0.18	
0.02	0.01	BL-	3-5	1.131(24)	0.03	
0.02	0.01	BL+	59-61	1.116(28)	0.05	
0.02	0.01	BL'	3-7	1.130(55)	0.03	
0.02	0.02	LL-g5	54-58	1.226(71)	0.05	×
0.02	0.02	LL-g45	56-58	1.456(82)	0.07	×
0.02	0.02	HL-g5	55-59	1.094(32)	0.25	
0.02	0.02	HL-g45	56-59	1.137(41)	0.006	
0.02	0.02	BL-	3-7	1.144(19)	0.08	
0.02	0.02	BL+	57-61	1.158(23)	0.08	
0.02	0.02	BL'	3-7	1.132(29)	0.01	
0.02	0.02	GL2-	4-8	1.128(31)	0.20	
0.02	0.02	GL2+	56-60	1.144(32)	0.16	
0.02	0.02	GG2-	4-8	1.077(44)	0.15	
0.02	0.02	GG2+	56-60	1.156(64)	1.22	
0.02	0.03	BL-	4-8	1.174(22)	0.12	
0.02	0.03	BL+	56-60	1.196(28)	0.008	
0.02	0.03	BL'	3-7	1.168(22)	0.008	
0.02	0.04	LL-g5	54-56	1.353(102)	0.01	×
0.02	0.04	LL-g45	54-56	1.371(122)	0.05	×
0.02	0.04	HL-g5	54-56	1.218(62)	0.006	
0.02	0.04	HL-g45	54-56	1.237(73)	0.11	
0.02	0.04	BL-	4-8	1.220(18)	0.18	
0.02	0.04	BL+	56-60	1.242(22)	0.003	
0.02	0.04	BL'	3-7	1.211(18)	0.003	

Table 4.7: Fit results for the N^* mass from all the correlators in the 0.02 ensemble, $24^3 \times 64$ lattice. All the masses are in lattice units.

to N^*. There is no clear signal for the N^* from the WL data in the $m_{sea} = 0.01$ case, so only the WL' data are considered. We already commented in the previous section on the difficulties in the determination of the mass of the negative parity partner of the nucleon. Note also that the small volume suffers from the fact

m_{sea}	m_{val}	correlator	fit range	M_{N^*}	χ^2/dof	
0.03	0.005	BL-	3-6	1.233(82)	0.44	
0.03	0.005	BL+	58-61	1.274(105)	0.43	
0.03	0.005	BL'	3-7	1.678(277)	1.4	×
0.03	0.01	BL-	3-5	1.175(37)	0.004	
0.03	0.01	BL+	59-61	1.193(46)	0.09	
0.03	0.01	BL'	3-7	1.314(98)	0.60	×
0.03	0.02	BL-	3-7	1.192(24)	0.07	
0.03	0.02	BL+	57-61	1.195(28)	0.004	
0.03	0.02	BL'	3-6	1.204(36)	0.04	
0.03	0.03	LL-g5	56-58	1.388(7)	0.12	×
0.03	0.03	LL-g45	55-57	1.287(147)	0.03	×
0.03	0.03	HL-g5	55-59	1.281(33)	0.09	
0.03	0.03	HL-g45	56-59	1.271(38)	0.03	
0.03	0.03	BL-	5-9	1.210(50)	0.07	
0.03	0.03	BL+	55-59	1.230(51)	0.02	
0.03	0.03	BL'	3-6	1.216(23)	0.02	
0.03	0.03	GL2-	4-8	1.195(27)	0.02	
0.03	0.03	GL2+	56-60	1.274(41)	0.09	
0.03	0.03	GG2-	4-7	1.240(41)	0.69	
0.03	0.03	GG2+	57-60	1.251(60)	0.04	
0.03	0.04	LL-g5	53-55	1.206(207)	0.04	×
0.03	0.04	LL-g45	53-56	1.246(131)	0.04	×
0.03	0.04	HL-g5	53-57	1.269(60)	0.04	
0.03	0.04	HL-g45	54-57	1.284(67)	0.01	
0.03	0.04	BL-	4-9	1.245(23)	0.04	
0.03	0.04	BL+	55-60	1.267(25)	0.08	
0.03	0.04	BL'	3-7	1.248(18)	0.02	

Table 4.8: Fit results for the N^* mass from all the correlators in the 0.03 ensemble, $24^3 \times 64$ lattice. All the masses are in lattice units.

that the sum in (2.90) is over 16^3 terms only compared to the 24^3 in the larger volume. Therefore the main objective here is using the small volume analysis in combination with the larger volume one to estimate the size of finite volume effects.

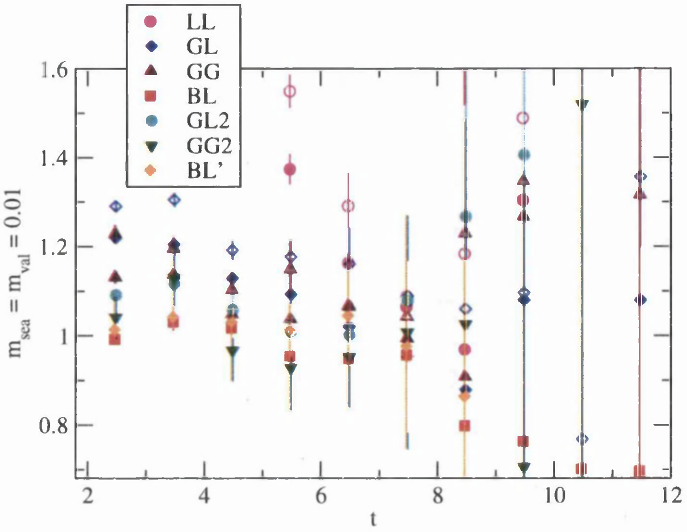

Figure 4.4: Effective masses obtained for the N^* from the fits to the $m_{sea} = m_{val} = 0.01$ correlators, in the $24^3 \times 64$ volume case. Note that the full symbols for the LL, GL and GG correlators correspond to the γ_5 interpolating operator, while the empty symbols correspond to $\gamma_4\gamma_5$.

4.8 Finite Volume Effects

An investigation of possible finite volume effects on the nucleon and the N^* was conducted by comparing the results from the small and large volume ensembles. For completeness we showed all our results in the tables in sections 4.6 and 4.7. Even if sometimes the same correlator types are not available in both volumes for the same quark combinations (different smearing for instance), in most cases we can compare like for like. To make comparison easier for the reader, we list in Table 4.15 the mass values obtained from simultaneous fits to the unitary points $m_{val} = m_{sea}^{light}$ in both cases (more details on the simultaneous fits are in section 4.9.1). Also, in figure 4.13 the effective masses of the nucleon and the N^* with valence and dynamical light quarks equal to 0.01, from both the $16^3 \times 32$ and

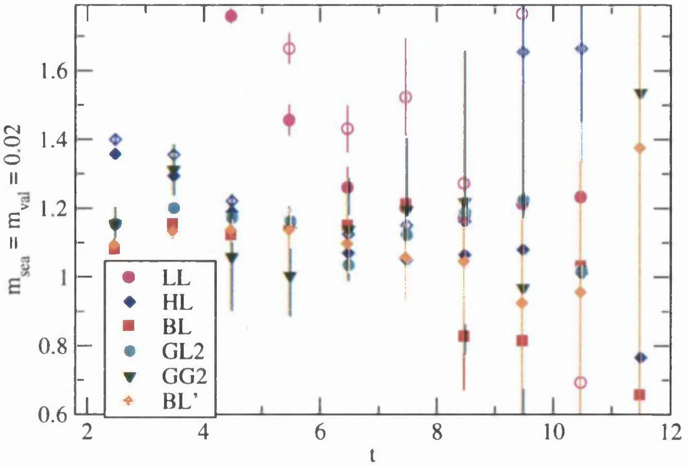

Figure 4.5: Effective masses obtained for the N^* from the fits to the $m_{sea} = m_{val} = 0.02$ correlators, in the $24^3 \times 64$ volume case. Note that the full symbols for the LL and HL correlators correspond to the γ_5 interpolating operator, while the empty symbols correspond to $\gamma_4\gamma_5$.

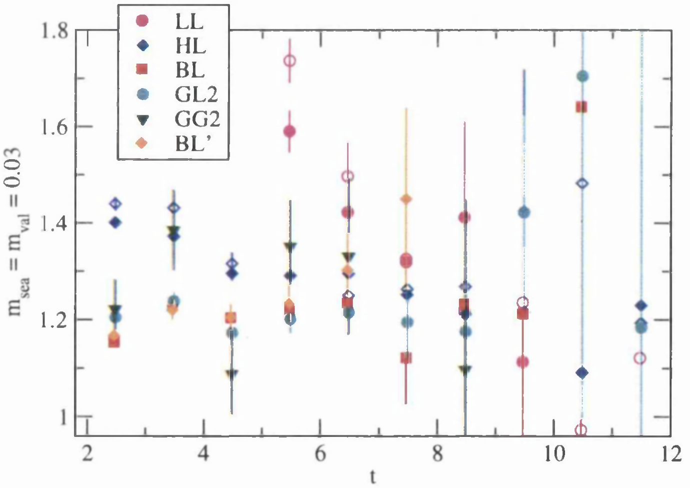

Figure 4.6: Effective masses obtained for the N^* from the fits to the $m_{sea} = m_{val} = 0.03$ correlators, in the $24^3 \times 64$ volume case. Note that the full symbols for the LL and HL correlators correspond to the γ_5 interpolating operator, while the empty symbols correspond to $\gamma_4\gamma_5$.

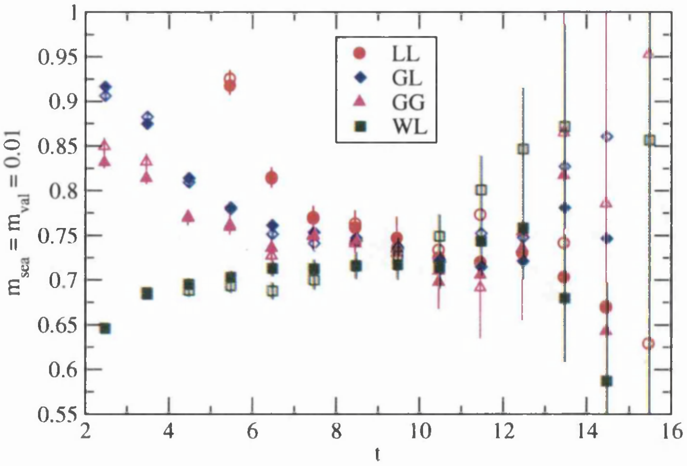

Figure 4.7: Effective masses for the nucleon obtained from the fits to the $m_{sea} = m_{val} = 0.01$ correlators in the $16^3 \times 32$ case. Note that the full symbols for the LL, GL and GG correlators correspond to the γ_5 interpolating operator, while the empty symbols correspond to $\gamma_4\gamma_5$. For the WL correlator, the full and empty symbols correspond to the positive- and negative-parity parts respectively.

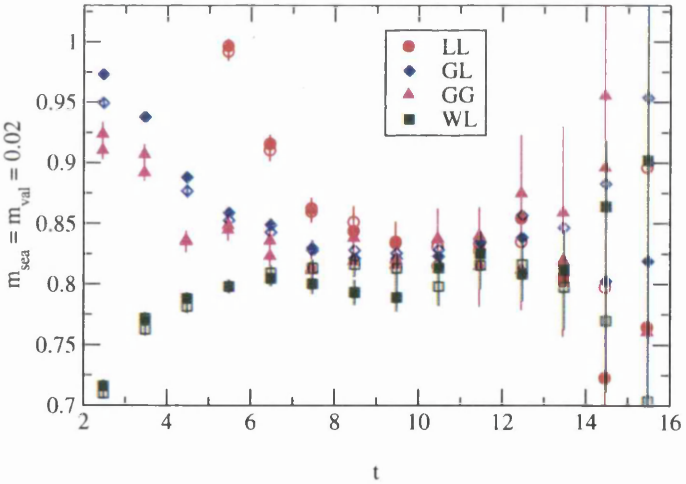

Figure 4.8: Effective masses for the nucleon obtained from the fits to the $m_{sea} = m_{val} = 0.02$ correlators in the $16^3 \times 32$ case. Note that the full symbols for the LL, GL and GG correlators correspond to the γ_5 interpolating operator, while the empty symbols correspond to $\gamma_4\gamma_5$. For the WL correlator, the full and empty symbols correspond to the positive- and negative-parity parts respectively.

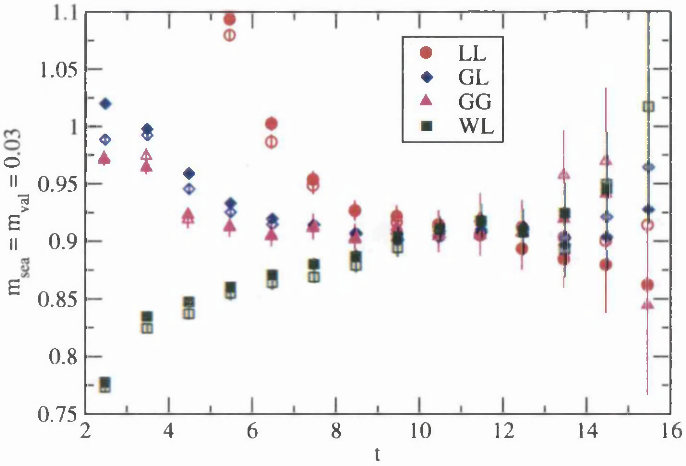

Figure 4.9: Effective masses obtained for the nucleon from the fits to the $m_{sea} = m_{val} = 0.03$ correlators in the $16^3 \times 32$ case. Note that the full symbols for the LL, GL and GG correlators correspond to the γ_5 interpolating operator, while the empty symbols correspond to $\gamma_4\gamma_5$. For the WL correlator, the full and empty symbols correspond to the positive- and negative-parity parts respectively.

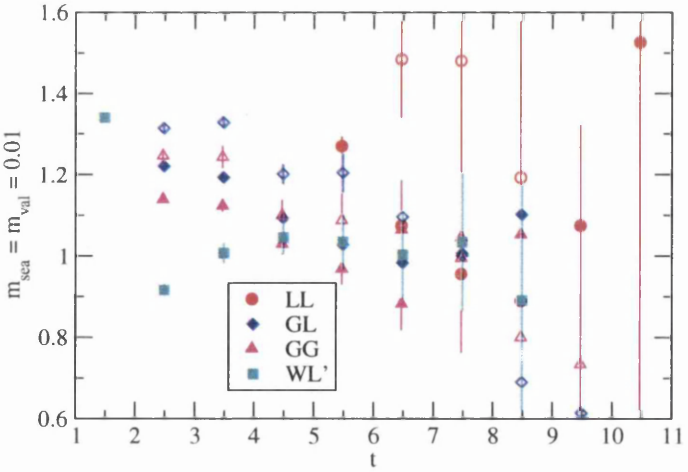

Figure 4.10: Effective masses obtained for the N^* from the fits to the $m_{sea} = m_{val} = 0.01$ correlators, in the $16^3 \times 32$ volume case. Note that the full symbols for the LL, GL and GG correlators correspond to the γ_5 interpolating operator, while the empty symbols correspond to $\gamma_4\gamma_5$.

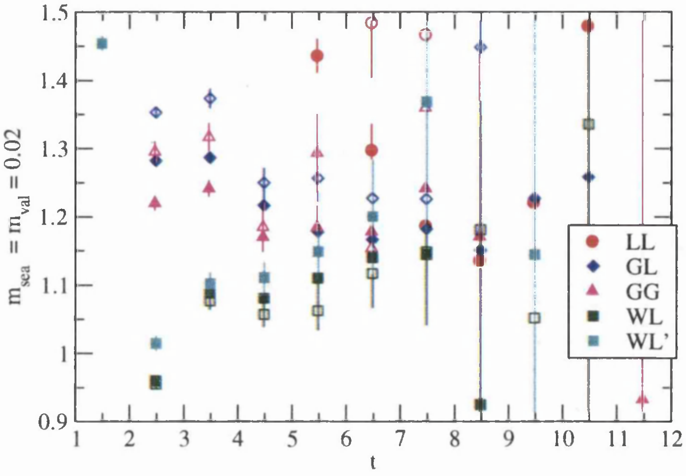

Figure 4.11: Effective masses obtained for the N^* from the fits to the $m_{sea} = m_{val} = 0.02$ correlators, in the $16^3 \times 32$ volume case. Note that the full symbols for the LL, GL and GG correlators correspond to the γ_5 interpolating operator, while the empty symbols correspond to $\gamma_4\gamma_5$.

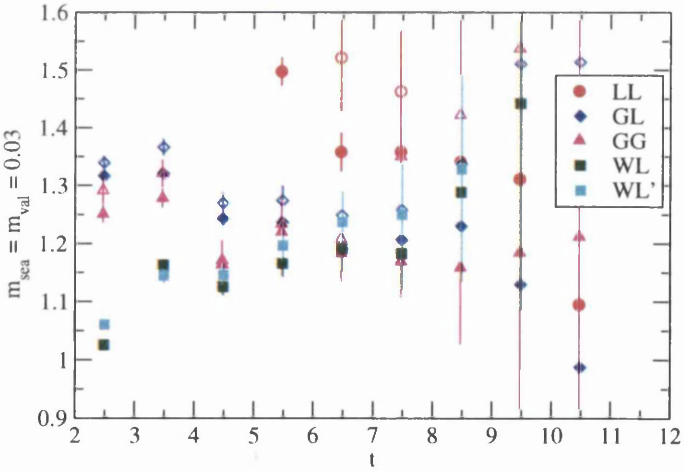

Figure 4.12: Effective masses obtained for the N^* from the fits to the $m_{sea} = m_{val} = 0.03$ correlators, in the $16^3 \times 32$ volume case. Note that the full symbols for the LL, GL and GG correlators correspond to the γ_5 interpolating operator, while the empty symbols correspond to $\gamma_4\gamma_5$.

m_{sea}	m_{val}	correlator	fit range	M_N	χ^2/dof
0.01	0.01	LL-g5	10-14	0.722(38)	0.002
0.01	0.01	LL-g45	9-14	0.743(29)	0.02
0.01	0.01	GL-g5	9-14	0.727(23)	0.03
0.01	0.01	GL-g45	8-12	0.736(15)	0.02
0.01	0.01	GG-g5	6-11	0.739(11)	0.13
0.01	0.01	GG-g45	6-11	0.737(11)	0.05
0.01	0.01	WL+	8-13	0.722(16)	0.06
0.01	0.01	WL-	19-24	0.748(20)	0.41
0.01	0.02	WL+	8-13	0.790(9)	0.003
0.01	0.02	WL-	19-24	0.809(10)	0.39
0.01	0.03	WL+	8-13	0.857(6)	0.001
0.01	0.03	WL-	19-24	0.867(8)	0.20
0.01	0.04	LL-g5	10-14	0.943(9)	0.003
0.01	0.04	LL-g45	9-14	0.947(7)	0.007
0.01	0.04	GL-g5	9-15	0.939(5)	0.03
0.01	0.04	GL-g45	8-13	0.935(5)	0.02
0.01	0.04	GG-g5	6-11	0.936(5)	0.11
0.01	0.04	GG-g45	6-11	0.932(5)	0.08
0.01	0.04	WL+	8-13	0.921(5)	0.006
0.01	0.04	WL-	19-24	0.925(6)	0.11

Table 4.9: Fit results for the nucleon mass from all the correlators in the 0.01 ensemble, $16^3 \times 32$ lattice. All the masses are in lattice units.

$24^3 \times 64$ ensembles are plotted. The top and bottom panels are for the LL and the $WL = BL$ correlator respectively, common to both the lattices. The effective masses for N have very good agreement between the two volumes in both cases. Although the effective masses for N^* show some differences, the large statistical errors make it hard to draw a final conclusion. The same kind of comparison was performed for the other ensembles. Note that the most appropriate comparison is the one between correlators of the same type in the two volumes, i.e. between Tables 4.3 and 4.9. From this comparison we conclude that no significant finite volume effects are observed for both the N and N^*. However, from the values

m_{sea}	m_{val}	correlator	fit range	M_N	χ^2/dof
0.02	0.01	WL+	5-11	0.731(10)	0.09
0.02	0.01	WL-	21-27	0.742(10)	0.05
0.02	0.02	LL-g5	10-14	0.828(17)	0.06
0.02	0.02	LL-g45	9-14	0.830(19)	0.01
0.02	0.02	GL-g5	9-15	0.826(13)	0.03
0.02	0.02	GL-g45	8-13	0.830(11)	0.04
0.02	0.02	GG-g5	7-13	0.821(10)	0.08
0.02	0.02	GG-g45	6-11	0.824(10)	0.04
0.02	0.02	WL+	10-14	0.815(15)	0.007
0.02	0.02	WL-	18-22	0.808(16)	0.01
0.02	0.03	WL+	6-12	0.866(6)	0.04
0.02	0.03	WL-	20-26	0.876(6)	0.009
0.02	0.04	LL-g5	10-14	0.952(8)	0.009
0.02	0.04	LL-g45	10-14	0.960(10)	0.003
0.02	0.04	GL-g5	9-13	0.951(7)	0.002
0.02	0.04	GL-g45	8-14	0.954(7)	0.007
0.02	0.04	GG-g5	7-13	0.949(6)	0.01
0.02	0.04	GG-g45	6-11	0.950(7)	0.02
0.02	0.04	WL+	7-13	0.931(6)	0.06
0.02	0.04	WL-	19-25	0.939(6)	0.07

Table 4.10: Fit results for the nucleon mass from all the correlators in the 0.02 ensemble, $16^3 \times 32$ lattice. All the masses are in lattice units.

m_{sea}	m_{val}	correlator	fit range	M_N	χ^2/dof
0.03	0.01	WL+	8-13	0.794(21)	0.31
0.03	0.01	WL-	19-24	0.757(19)	0.06
0.03	0.02	WL+	9-13	0.858(14)	0.05
0.03	0.02	WL-	19-23	0.844(14)	0.03
0.03	0.03	LL-g5	10-14	0.913(19)	0.003
0.03	0.03	LL-g45	10-14	0.922(18)	0.002
0.03	0.03	GL-g5	8-14	0.908(9)	0.01
0.03	0.03	GL-g45	8-14	0.910(10)	0.02
0.03	0.03	GG-g5	6-13	0.908(9)	0.02
0.03	0.03	GG-g45	6-12	0.914(10)	0.08
0.03	0.03	WL+	9-13	0.910(10)	0.02
0.03	0.03	WL-	19-23	0.908(10)	0.05
0.03	0.04	LL-g5	10-14	0.969(13)	0.02
0.03	0.04	LL-g45	10-14	0.976(14)	0.01
0.03	0.04	GL-g5	8-14	0.966(7)	0.006
0.03	0.04	GL-g45	8-14	0.969(9)	0.01
0.03	0.04	GG-g5	6-13	0.966(8)	0.02
0.03	0.04	GG-g45	6-12	0.972(9)	0.05
0.03	0.04	WL+	9-13	0.965(8)	0.007
0.03	0.04	WL-	19-23	0.965(8)	0.05

Table 4.11: Fit results for the nucleon mass from all the correlators in the 0.03 ensemble, $16^3 \times 32$ lattice. All the masses are in lattice units.

m_{sea}	m_{val}	correlator	fit range	M_{N^*}	χ^2/dof
0.01	0.01	LL-g5	22-25	0.948(97)	0.01
0.01	0.01	LL-g45	22-24	1.310(534)	0.10
0.01	0.01	GL-g5	23-25	1.027(98)	0.07
0.01	0.01	GL-g45	24-26	1.065(84)	0.06
0.01	0.01	GG-g5	23-27	0.948(46)	0.16
0.01	0.01	GG-g45	23-27	1.057(83)	0.11
0.01	0.01	WL'	4-8	1.033(59)	0.01
0.01	0.02	WL'	4-8	1.027(24)	0.01
0.01	0.03	WL'	4-8	1.076(16)	0.01
0.01	0.04	LL-g5	22-24	1.219(38)	0.002
0.01	0.04	LL-g45	22-24	1.257(46)	0.10
0.01	0.04	GL-g5	22-25	1.206(19)	0.006
0.01	0.04	GL-g45	24-26	1.224(17)	0.15
0.01	0.04	GG-g5	24-27	1.183(14)	0.66
0.01	0.04	GG-g45	24-27	1.192(18)	0.41
0.01	0.04	WL'	4-8	1.129(13)	0.08

Table 4.12: Fit results for the N^* mass from all the correlators in the 0.01 ensemble, $16^3 \times 32$ lattice. All the masses are in lattice units.

m_{sea}	m_{val}	correlator	fit range	M_{N^*}	χ^2/dof
0.02	0.01	WL-	5-8	1.129(96)	0.04
0.02	0.01	WL+	24-27	1.102(93)	0.32
0.02	0.01	WL'	3-5	1.277(81)	0.08
0.02	0.02	LL-g5	23-25	1.169(68)	0.03
0.02	0.02	LL-g45	25-26	1.484(81)	-
0.02	0.02	GL-g5	23-26	1.169(44)	0.006
0.02	0.02	GL-g45	24-26	1.227(49)	0.00002
0.02	0.02	GG-g5	24-27	1.188(42)	0.03
0.02	0.02	GG-g45	25-27	1.244(57)	0.30
0.02	0.02	WL-	5-8	1.124(36)	0.04
0.02	0.02	WL+	24-27	1.092(40)	0.13
0.02	0.02	WL'	5-8	1.211(68)	0.40
0.02	0.03	WL-	5-8	1.156(22)	0.08
0.02	0.03	WL+	24-27	1.137(26)	0.07
0.02	0.03	WL'	4-8	1.191(33)	0.50
0.02	0.04	LL-g5	22-24	1.269(40)	0.0003
0.02	0.04	LL-g45	20-22	1.283(227)	0.002
0.02	0.04	GL-g5	22-25	1.231(27)	0.06
0.02	0.04	GL-g45	22-26	1.263(24)	0.03
0.02	0.04	GG-g5	24-27	1.257(22)	0.20
0.02	0.04	GG-g45	23-26	1.244(38)	0.005
0.02	0.04	WL-	5-9	1.194(18)	0.05
0.02	0.04	WL+	23-27	1.187(21)	0.04
0.02	0.04	WL'	5-8	1.199(20)	0.023

Table 4.13: Fit results for the N^* mass from all the correlators in the 0.02 ensemble, $16^3 \times 32$ lattice. All the masses are in lattice units.

m_{sea}	m_{val}	correlator	fit range	M_{N^*}	χ^2/dof
0.03	0.01	WL-	3-7	1.136(49)	0.46
0.03	0.01	WL+	25-29	1.070(46)	0.02
0.03	0.01	WL'		-	
0.03	0.02	WL-	3-7	1.114(20)	0.23
0.03	0.02	WL+	25-29	1.068(19)	0.21
0.03	0.02	WL'	3-5	1.142(26)	0.02
0.03	0.03	LL-g5	22-24	1.332(112)	0.004
0.03	0.03	LL-g45	24-26	1.499(93)	0.01
0.03	0.03	GL-g5	24-27	1.214(19)	0.11
0.03	0.03	GL-g45	24-27	1.262(34)	0.01
0.03	0.03	GG-g5	22-27	1.189(32)	0.06
0.03	0.03	GG-g45	25-27	1.223(40)	0.01
0.03	0.03	WL-	5-8	1.177(30)	0.02
0.03	0.03	WL+	24-27	1.108(24)	0.007
0.03	0.03	WL'	5-8	1.220(40)	0.05
0.03	0.04	LL-g5	22-24	1.334(70)	0.006
0.03	0.04	LL-g45	24-26	1.499(52)	0.05
0.03	0.04	GL-g5	24-27	1.264(15)	0.17
0.03	0.04	GL-g45	24-28	1.299(17)	0.04
0.03	0.04	GG-g5	23-27	1.245(23)	0.09
0.03	0.04	GG-g45	25-27	1.280(31)	0.006
0.03	0.04	WL-	5-8	1.214(21)	0.02
0.03	0.04	WL+	24-27	1.170(19)	0.009
0.03	0.04	WL'	5-8	1.233(25)	0.11

Table 4.14: Fit results for the N^* mass from all the correlators in the 0.03 ensemble, $16^3 \times 32$ lattice. Note that no signal was found for the N^* from the WL' correlators with $m_{val} = 0.01$. All the masses are in lattice units.

quoted in Table 4.15 from the simultaneous fits, we notice that the results for the N^* do not follow a particular trend, while some evidence for marginal finite size effects is present for the nucleon.

m_{sea}	m_{val}	N		N^*	
		mass	χ^2/dof	mass	χ^2/dof
0.01	0.01	0.738(9)	0.29	1.020(35)	0.38
0.01	0.01	0.722(5)	0.15	1.035(17)	0.71
0.02	0.02	0.825(9)	0.13	1.161(26)	0.65
0.02	0.02	0.808(4)	0.21	1.143(12)	0.68
0.03	0.03	0.910(8)	0.22	1.211(18)	0.32
0.03	0.03	0.890(5)	0.34	1.252(12)	0.76

Table 4.15: Comparison of N and N^* masses from a simultaneous fit to all correlator types for each ensemble in the unitary case $m_{val} = m_{sea}^{light}$. The first row of each set is from the $16^3 \times 32$ volume, the second from $24^3 \times 64$. The errors quoted are from a jackknife analysis. All the masses are in lattice units.

The origin of finite size effects is closely related to nuclear forces and it has been shown that for sufficiently large lattices of side L, the finite volume corrections in the mass M of a given state fall off as $e^{-m_{PS}L}$ [58]. A typical test to determine the lattice size needed for observables involving quark propagation uses the pseudoscalar meson as it is the lightest particle and thus it has the largest correlation length. It has been shown that the exponential suppression applies for $m_{PS}L \geq 4$, therefore finite size corrections are negligible in this case. For our lattices with $L = 1.95\ fm$ and $L = 2.9\ fm$, considering $m_{PS} \sim 390\ MeV$, we have $m_{PS}L \sim 3.85$ and 5.7 respectively. So the marginality of finite size effects is not surprising. As already mentioned, in order to fully satisfy the condition for negligible finite volume effects then, we consider the large volume simulations our source of physical results for the nucleon spectrum.

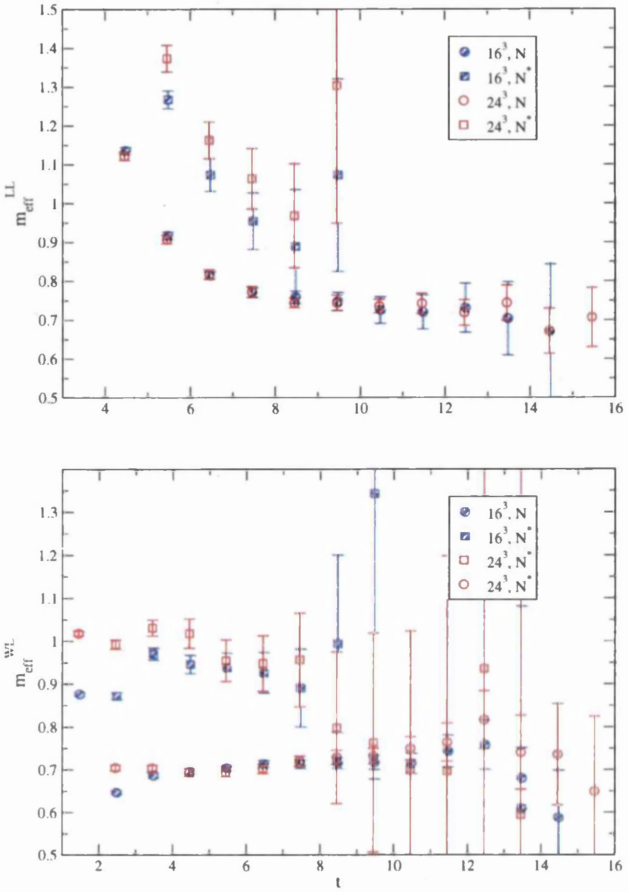

Figure 4.13: Comparison of the nucleon and the N^* effective masses from the small and large volume ensembles with the valence and light dynamical quark masses equal to 0.01. Top and bottom panels show the LL and WL correlators case respectively.

4.9 $24^3 \times 64$: results

4.9.1 Simultaneous Fits

From the tables and plots just seen, it is easy to realize that different correlators can have very different behaviours: for instance the plateaus start earlier or later, and the mass values obtained can sometimes differ somewhat. This is why fitting to a single smearing type is not a very reliable method of analysis. The availability of different correlators types for the same sea-valence combination allows us to perform a simultaneous fit to all the correlators and minimize systematic errors arising from different characteristics of the operators. Therefore a more detailed study was performed for the unitary data points of each ensemble, where the largest variety of correlators is available. The non-unitary data points were included in the analysis mainly in order to perform an extrapolation in the valence quarks as well as in the sea quarks.

Table 4.16 shows the results from a simultaneous fit to all the available correlators for each data set in each ensemble: a unique value for the mass is then obtained. Since the correlators are measured on the same gauge background, in principle we should take into account correlations among different correlators and different time slices of the same correlator. However we explained in section 4.5 that our statistics does not allow a reliable correlated fit, due to the poor resolution of the covariance matrix one gets when the number of data points is comparable to or greater than the number of independent configurations. The fit ranges used in the simultaneous fits (shown in the tables of fits) are the ones individually chosen as explained in section 4.5.

Some more comments regarding our results are necessary at this point. As already noticed, different correlators can have different behaviour. Also, a smeared type operator can be very effective in improving the signal for some valence (and sea) value, but become ineffective for a different value, corresponding to a different hadron size. The same applies for different interpolating operators. As we can see from Tables 4.3, 4.4 and 4.5, the signals for the nucleon state are very stable. However the considerations above often apply to its parity partner, see Tables 4.6, 4.7 and 4.8. This is why, when performing simultaneous fits, we decided to discard those correlators that show a very bad signal or do not show a signal for the state in study, giving a mass far from the other values or with very large error bars: these are the correlators ticked with a × in Tables 4.6, 4.7 and 4.8.

m_{sea}	m_{val}	N_{cfgs}	N		N^*	
			mass	χ^2/dof	mass	χ^2/dof
0.01	0.005	60	0.683^{+10}_{-12}	0.48	1.013^{+39}_{-34}	0.83
0.01	0.01	60	0.722^{+3}_{-3}	0.15	1.025^{+12}_{-11}	0.62
0.01	0.02	60	0.792^{+7}_{-6}	0.02	1.055^{+19}_{-14}	0.28
0.01	0.03	60	0.855^{+6}_{-5}	0.02	1.113^{+15}_{-11}	0.45
0.01	0.04	60	0.932^{+2}_{-2}	0.23	1.168^{+10}_{-7}	0.29
0.02	0.005	46	0.706^{+16}_{-18}	0.10	1.168^{+42}_{-41}	0.83
0.02	0.01	46	0.745^{+10}_{-11}	0.10	1.126^{+19}_{-19}	0.10
0.02	0.02	46	0.808^{+3}_{-3}	0.22	1.138^{+11}_{-12}	0.38
0.02	0.03	46	0.880^{+6}_{-4}	0.02	1.177^{+16}_{-13}	0.45
0.02	0.04	46	0.939^{+3}_{-3}	0.11	1.222^{+12}_{-11}	0.34
0.03	0.005	52	0.726^{+14}_{-10}	0.34	1.246^{+58}_{-72}	0.33
0.03	0.01	52	0.761^{+10}_{-8}	0.01	1.182^{+27}_{-31}	0.05
0.03	0.02	52	0.826^{+13}_{-9}	0.07	1.195^{+13}_{-19}	0.05
0.03	0.03	52	0.891^{+3}_{-3}	0.39	1.241^{+11}_{-13}	0.52
0.03	0.04	52	0.951^{+3}_{-3}	0.31	1.255^{+10}_{-13}	0.17

Table 4.16: Values of the N and N^* masses from a simultaneous fit to all correlator types for each ensemble. N_{cfgs} is the number of measurements considered in each simultaneous fit: the different N_{traj} ranges for each correlator type, Table 4.1, are restricted to a common range for each ensemble and accurately binned in order to have the same number of configurations for each set of correlators. The errors quoted are from a bootstrap analysis (section 2.13.2). All the masses are in lattice units.

4.9.2 Extrapolations

Once all the simultaneous fits for each combination $m_{sea} - m_{val}$ are performed, we are able to carry out an extrapolation in the valence quarks: for each ensemble we

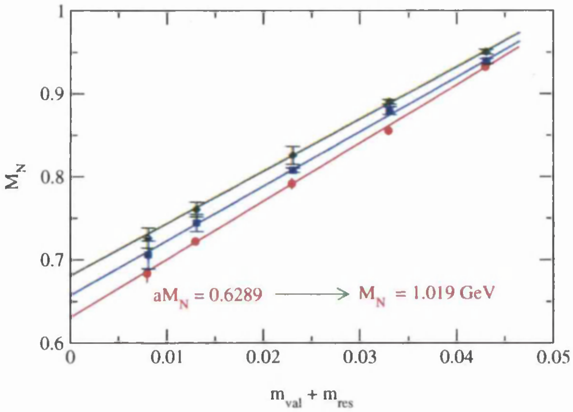

Figure 4.14: Valence extrapolation of the nucleon mass M_N for all three ensembles at $m_{val} = -m_{res}$. Also shown is the extrapolated value at the lowest sea and the corresponding value for the mass in physical units.

have 5 data points (all the possible valence available). Note that since we perform our simulations at quark masses heavier than the physical up and down quark masses, extrapolations are needed to obtain physical results for the hadronic observables of interest. In figure 4.14 the chiral valence extrapolation is shown for all three ensembles. Note that in the extrapolations the value of $m_{res} = 0.003147(12)$ [55] is used. Neglecting higher-order corrections, the chiral limit is defined at $m_f + m_{res} = 0$ or $m_f = -m_{res}$, where m_f is the input quark mass. In figure 4.14, as an indication for the reader, we also show the nucleon mass extrapolated at the lightest sea with the corresponding value in physical units obtained using the lattice spacing $a^{-1} = 1.62(4)\ GeV$.

A more rigorous value for the nucleon mass is obtained considering an extrapolation in both the valence and sea quarks. We perform different types of extrapolation as follows. We first consider all three ensembles, with 15 sea-valence combinations in total; then we include only the two lightest ensembles, $m_{sea} = 0.01, 0.02$, with a total of 10 sea-valence combinations. Finally, we only consider the two lightest sea as well as the two lightest valence. Table 4.17 quotes the values from each of these three methods for the nucleon mass in lattice units, aM_N, as well as the corresponding physical values in GeV estimated using $a^{-1} = 1.62(4)\ GeV$. Presumably, including only lighter quark masses gives a more reliable chiral extrapolation. In fact the nucleon mass decreases and gets closer to the physical value[3] when we consider the lightest quark combinations.

m_{sea}	m_{val}	aM_N	$M_N[GeV]$
0.01 0.02 0.03	0.005 0.01 0.02 0.03 0.04	0.619^{+4}_{-5}	1.003^{+25}_{-26}
0.01 0.02	0.005 0.01 0.02 0.03 0.04	0.615^{+6}_{-6}	0.996^{+26}_{-26}
0.01 0.02	0.005 0.01	0.591^{+24}_{-32}	0.957^{+46}_{-58}

Table 4.17: Value of the nucleon mass obtained from extrapolations in both the sea and the valence quark masses, as indicated in the first and second columns. Last column shows the corresponding physical values in GeV obtained using $a^{-1} = 1.62(4)\ GeV$.

A similar approach is used in the case of the N^*. We first performed an extrapolation in the valence quarks for each ensemble. From Table 4.16 we can see that the N^* masses obtained from the $m_{val} = 0.005$ correlators, in particular in the $m_{sea} = 0.02,\ 0.03$ cases, are not very consistent with the trend of growth of the other valence compositions and present larger errors. In the $m_{sea} = 0.02$ case, the value quoted is from a simultaneous fit to the BL and BL' correlators which show a very poor signal at this light valence value; for $m_{sea} = 0.03$ the BL' was not even included in the simultaneous fit and the value quoted comes from the

---

[3] From http://pdg.lbl.gov/2007:

$$M_p = (938.272029 \pm 0.000080)\ MeV \quad and \quad M_n = (939.565360 \pm 0.000081)\ MeV$$

for proton and nucleon respectively.

correlator BL. A better signal is present in the $m_{sea} = 0.01$ case, but no significant difference is found by including or not the $m_{val} = 0.005$ point in the extrapolation[4]. Therefore we exclude the lightest valence from all three extrapolations, as shown in the plot in figure 4.15.

For a better determination of the N^* mass, we then consider an extrapolation in both the valence and sea quarks. As for the nucleon case, we first consider all three ensembles, with 12 sea-valence combinations in total; then we exclude the heaviest ensemble, with a total of 8 sea-valence combinations in the $m_{sea} = 0.01,\ 0.02$ sector. Finally we only consider the two lightest sea values as well as the two lightest valence values. Table 4.18 quotes the three values obtained for the mass of N^* in lattice units, aM_{N^*}, as well as the corresponding values in GeV.

Note that we could have chosen to extrapolate at the physical point, corresponding to $M_{PS} = 140\ MeV$, instead of at quark mass equal to zero. The determination of the physical quark mass requires a well controlled chiral extrapolation in the light quark limit. Ideally the next-to-leading-order chiral perturbation theory (NLO χPT) should be used, but it has been shown [59] that our data can not be described by the NLO χPT, probably due to too heavy quark masses corresponding to pion masses of 390 to 630 MeV [59]. A linear extrapolation can be then considered, i.e.

$$M_{PS}^2 = B(m_{sea}^{light} + m_{res}). \tag{4.13}$$

The determination of the physical quark mass was not part of this work: using results in [59] we can qualitatively quote $M_N = 0.984^{+35}_{-46}\ GeV$ and $M_{N^*} = 1.452^{+56}_{-40}\ GeV$ as the masses we obtained through an extrapolation at the physical

---

[4] In fact, the N^* masses obtained in the $m_{val} = 0.005$ and 0.01 cases have very close values, see Table 4.16.

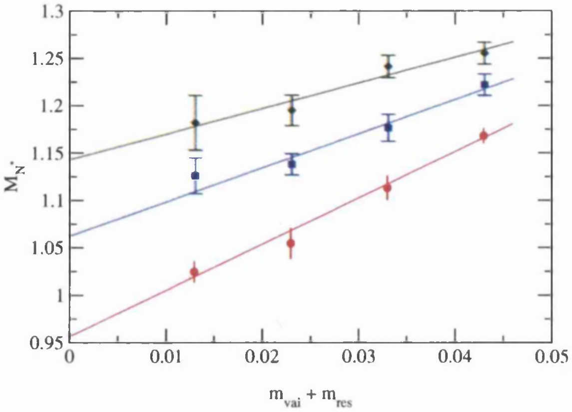

Figure 4.15: Valence extrapolation of the N^* mass for all three ensembles at $m_{val} = -m_{res}$. The $m_{val} = 0.005$ data points have been discarded, as explained in the text.

quark masses in the light quark limit.

m_{sea}	m_{val}	aM_{N^*}	$M_{N^*}[GeV]$
0.01 0.02 0.03	0.01 0.02 0.03 0.04	0.905^{+18}_{-13}	1.466^{+46}_{-42}
0.01 0.02	0.01 0.02 0.03 0.04	0.881^{+23}_{-21}	1.427^{+51}_{-49}
0.01 0.02	0.01 0.02	0.878^{+30}_{-28}	1.422^{+60}_{-57}

Table 4.18: Value of the N^* mass obtained from extrapolations in both the sea and the valence quark masses, as indicated in the first and second columns. Last column shows the corresponding physical values in GeV obtained using $a^{-1} = 1.62(4)\ GeV$.

4.10 Conclusions

We saw in Table 4.17 how the values for the nucleon mass obtained from chiral extrapolations approach the experimental value going to lighter quark masses. We can then quote our final result for the nucleon mass as

$$M_N = 957^{+46+46}_{-58-0}\ MeV, \tag{4.14}$$

where the first error is statistical and the second takes into account the other two values in Table 4.17, found when different (heavier) sea-valence combinations are considered.

Following the same arguments for the nucleon parity partner state, we can write

$$M_{N^*} = 1422^{+60+45}_{-57-0}\ MeV. \tag{4.15}$$

Despite the rather large uncertainties, the M_{N^*} value appear much lower than the experimental estimate, $1525 - 1545\ MeV$. Following [71], we explored a possible explanation for the apparently fast falling of the data with the quark mass. At sufficiently light quark masses, the decay channel $N^* \rightarrow N + \pi$ is open. In order to investigate the possibility of our N^* to decay into such a lighter state, we look at the $m_{sea} = 0.01$ ensemble, where more statistics are available and no data were discarded in the simultaneous fits. The data points in figure 4.16 are the M_{N^*} values from the simultaneous fits (Table 4.16), while the dashed line connects the values of the mass of the nucleon plus the pseudoscalar meson. All the masses are in physical units. We see from this plot that our data points do not follow the dashed line, even if the lightest point were discarded. Clearly the interpolating operators used to reproduce the N^* at our parameters values for our lattice size have a stronger overlap with the single-hadron state and we can conclude that the state studied in this work is actually the $N(1535)$.

In figure 4.17 we plot our values for N and N^*, as well as the corresponding experimental values, $N(939)$ and $N(1535)$. The nucleon state N is much better determined than the N^*. We already commented on the difficulties to determine the N^*. We conclude that our results for the nucleon mass are in good agreement

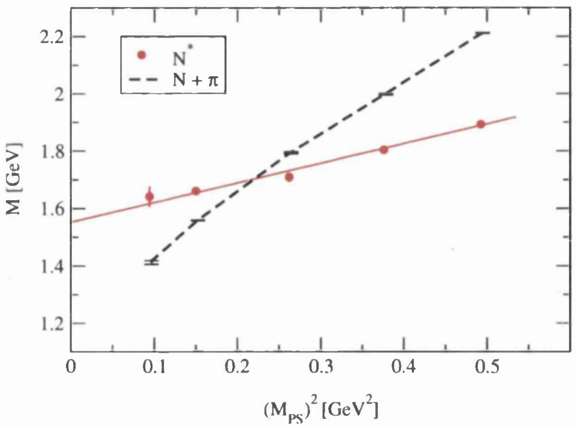

Figure 4.16: Chiral extrapolation of the N^* mass for the $m_{sea} = 0.01$ ensemble. The dashed line represents the nucleon mass plus the pseudoscalar meson mass.

with the experiments within the rather large statistical uncertainties.

A more comprehensive calculation of the nucleon and baryon spectrum is under active pursuit. The work in progress includes data from a lighter ensemble at $m_{sea} = 0.005$, which clearly will make more precise the chiral extrapolation of particles under study. Final results will appear in an upcoming paper [55] written jointly by the baryon group of the RBC and UKQCD collaborations.

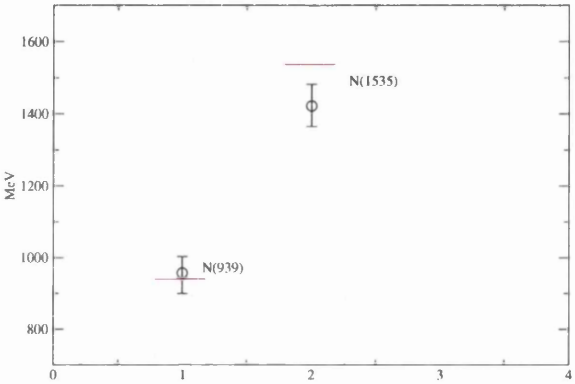

Figure 4.17: Comparison of the physical results obtained in this work (circles) with the experimental values (horizontal lines).

Chapter 5

D_S Mesons with Overlap

5.1 D_s Physics and LGT

The discoveries a few years ago of new resonances D_{sJ} have provoked much interest in heavy-light systems in general and in the D_s mesons in particular. The BaBar collaboration first reported [61] evidence for a new narrow resonance decaying to $D_s^+\pi^0$ at a mass near 2.32 GeV. The data were consistent with the identification of this state as one of the four lowest-lying members of the $c\bar{s}$ mesons system with orbital angular momentum $L = 1$. It was named $D_{sJ}^*(2317)$ and its characteristics suggest a $J^P = 0^+$ assignment. In the search for the $D_{sJ}^*(2317)$ meson and other possibly related states, the CLEO collaboration observed [62] another narrow resonance in the $D_s^{*+}\pi^0$ final state, with a mass near 2.46 GeV. They confirmed the consistency of the data with the possible interpretation of the two states at 2.32 and 2.46 GeV as $c\bar{s}$ mesons with $L = 1$ and spin-parity $J^P = 0^+$ and 1^+ respectively.

These observations were consistent with the theoretical prediction [63] in heavy-light meson systems of the existence of the heavy spin multiplet $\{0^+, 1^+\}$, parity partner of the ground state multiplet $\{0^-, 1^-\}$ (see next section for more details).

In this scenario, the D_s mesons (and D physics in general) clearly appear very interesting objects to be studied on the lattice. Not only does the spectrum offer several new possibilities of investigation, in particular after the discovery of the positive parity partners of the D_s and D_s^*, but also the recent determination by the charm factory of the leptonic decay constants f_D [64, 65] and f_{D_s} [66] produced new challenges and possible tests for lattice QCD: for instance, new determinations of the CKM matrix elements V_{cd} and V_{cs} and the amplitude ratio f_{D_s}/f_D.

In this work we focus on the D_s spectroscopy and on the experimentally determined quantities in D_s calculations: the parity and hyperfine splittings and their independence on the spin and the parity respectively. Many previous lattice calculations [67, 68, 69, 70, 71, 72] tried to reproduce the features of these heavy-light charm mesons: most of these consider a static or non-relativistic heavy charm quark, with the exception of [70] which uses the Fermilab approach and [72] which describes the charm quark as a domain wall fermion. All these works are in the quenched approximation.

Here we present preliminary results of the very first study with $2+1$ dynamical flavours. We also perform a quenched approximation calculation at a matching lattice spacing. The novelty of our work is considering the charm quark propagating as an overlap fermion, while the light strange quark is a domain wall fermion. We will see in more detail in next section how the chiral symmetry of the light quarks are important in the model for heavy-light systems: in fact we exploit the good chiral symmetry of DWF for the light strange quark. As far as the heavy quark is concerned, the charm quark has a mass of around $1.2 - 1.5\ GeV$, so it is not surprising that lattice actions develop rather severe discretization effects when $m_c \sim a^{-1}$. This is why when the quark mass is the same size as the cutoff, the study of the properties of heavy quark systems relies on effective field theories. The effective action for the heavy quark has the form of an expansion in powers of a small parameter: Heavy Quark Effective Theory (HQET), whose expansion parameter is the inverse of the heavy quark mass, is usually used in heavy-light systems. However, we might be interested in physical processes at scales not far below the cutoff, where effective theories become poor as well. As explained in section 2.8, overlap fermions, not only have good chiral properties, but can also alleviate some problems related to simulating heavy quarks, since they appear to be free from $\mathcal{O}(m_c a)$ errors, and have small $\mathcal{O}(m_c^2 a^2)$ corrections [75]. This is the principle reason why we implemented the charm as overlap.

This study is carried out in collaboration with RBC-UKQCD members.

5.2 The Parity Doubling Model

Heavy-light mesons, containing one heavy quark Q and one light quark q, are subject to powerful symmetry constraints [63]. In fact, the pseudoscalar and vector mesons containing one massive and one light quark become degenerate in the heavy quark limit, $m_Q \to \infty$, due to a heavy quark spin symmetry valid up to $\mathcal{O}(1/m_Q)$ [73]. While heavy quark (HQ) symmetry maintains the degeneracy within the $\{0^-, 1^-\}$ and $\{0^+, 1^+\}$ multiplets, i.e. spin degeneracy, implying vanishing hyperfine splitting effects, unbroken chiral symmetry of the light quark (LQ) would imply the degeneracy of the two multiplets themselves. In fact, in the LQ limit, $m_q \to 0$, with $q = (u, d, s)$, the Lagrangian must be invariant under $SU(3)_L \times SU(3)_R$ chiral symmetry. Therefore the breaking of the chiral symmetry leads to a mass gap between parity partners, with associate pionic transitions

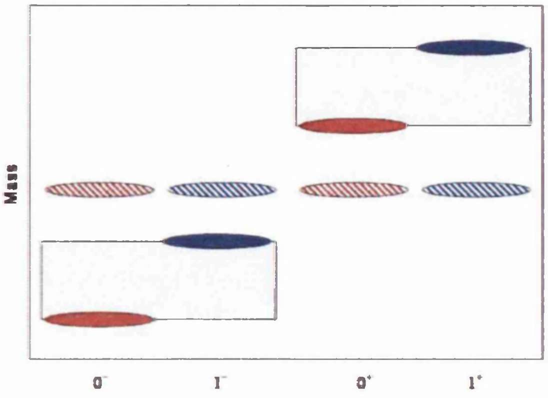

Figure 5.1: Schematic representation of the $\{0^-, 1^-\}$ and $\{0^+, 1^+\}$ multiplets, in the double limit of HQ and LQ symmetry, dashed symbols, and when both the symmetries are broken, full symbols.

$\{0^+, 1^+\} \rightarrow \{0^-, 1^-\} + \pi$, elevating the heavier $\{0^+, 1^+\}$ multiplet and depressing the lighter $\{0^-, 1^-\}$. These decay transitions are governed by a Goldberger-Treiman relation [74], $g_\pi = \Delta M/f_\pi$, where ΔM is the $0^+ - 0^-$ mass difference, g_π is the $0^+ \rightarrow 0^-\pi$ coupling constant and f_π the pion decay constant. More details on the parity doubling model of Bardeen, Eichten and Hill are found in [63, 73] and are not in the scope of this study. We just give a visualization in figure 5.1: in the double limit of heavy quark and chiral symmetry the multiplets appear totally degenerate, i.e. the dashed oval figures shown in a horizontal line. The full oval figures give an idea of the splitting due to both the HQ and LQ broken limits: the gap between the red and light ovals in each rectangular represents the hyperfine splitting, while the gap between the two red ovals, as well as between the two blue ones, represent the parity splitting.

5.3 Numerical Details

The dynamical analysis was performed on 2+1 flavours DWF ensembles generated jointly by the RBC and UKQCD collaborations. These were the 'small volume' ensembles used in chapter 4. Specifically, the simulations used the Iwasaki gauge action with $\beta = 2.13$ and the domain wall fermion quark action with the fifth dimension fixed to $L_s = 16$ and the domain wall height set to $M_5 = 1.8$. The volume size is $16^3 \times 32$ and a single lattice spacing of $a^{-1} = 1.62(4)\ GeV$[1] gives a corresponding spatial volume of $(1.9\ fm)^3$. Three sets of configurations were generated with a light isodoublet with masses $am_{ud} = am_{sea} = 0.01,\ 0.02,\ 0.03$, and a fixed approximate strange quark mass, $am_s = 0.04$. As mentioned in chapter 4, the ensembles were generated using the RHMC algorithm and its implementations [19], and they are described in more detail in [54].

The meson correlators were measured with sources on multiple time planes, in order to improve our statistics. Details of the three ensembles used are listed in Table 5.1. Note that momenta different from zero have been also considered in order to investigate higher mass states and mainly allow a dispersion relation analysis, as explained in section 5.4.1.

The D_s correlators were generated in this gauge background with the light strange quark as a domain wall fermion and the heavy charm as an overlap fermion. The main analysis of this work was performed on correlators generated at two different charm quark masses, $am_c \sim 0.72,\ 0.9$, producing two different heavy-light mesons for each ensemble, labelled H_3 and H_4 respectively. Recalling the

---

[1] See section 4.4 for the determination of the lattice scale.

m_{sea}	N_{traj}	Δ	N_{meas}	N_{src}	p^2_{max}	am_c	Meson
0.01	500-4000	50	282	4	4	0.72 0.9	H_3 H_4
0.02	1000-4025	50	122	2	4	0.72 0.9	H_3 H_4
0.03	1000-4000	50	121	2	2	0.72 0.9	H_3 H_4
0.02	1000-4040	10	305	1	4	0.36 0.54	H_1 H_2
quenched	10000-29200	200	97	1	4	0.36 0.54 0.72 0.9	H_1 H_2 H_3 H_4

Table 5.1: Measurement parameters for all the datasets used in this study. N_{traj} is the lowest to highest trajectory analysed with Δ the separation between measurements in molecular dynamics time unit. N_{src} is the number of different sources used for each set of measurements. In the last two columns, the charm quark mass considered and, for labels, the corresponding meson are specified for each set of data.

expression of the massive overlap operator, eq.(2.79), we write

$$aD_{ov} = \rho(1+\mu) + \rho(1-\mu)\gamma_5 sgn(\gamma_5(aD_W - \rho)), \tag{5.1}$$

where $\mu = \frac{am_q}{2\rho}$ and ρ is any mass parameter that can be added to the Dirac operator D_W without affecting the continuum limit: here it was chosen equal to 1.3 looking at the heavy-heavy pseudoscalar meson. The overlap operator was used to invert on hyp-smeared DWF gauge configurations for mass parameter $\mu \sim 0.277,\ 0.346$, corresponding to the two charm mass values above.

In later stages of this work, we ran a test with two lighter choices of the charm quark mass, $am_c \sim 0.36,\ 0.54$, obtaining two lighter heavy-light mesons, labelled H_1 and H_2 respectively: the new correlators were generated only on the $am_{sea} = 0.02$ ensemble. The fourth dataset in Table 5.1 is specific for this case. Therefore, we will indicate in the following with H_1, H_2, H_3, H_4 the four possible quark mass pairs, from the lightest to the heaviest. However, note that in the dynamical analysis for the $am_{sea} = 0.01$ and 0.03 ensembles, only the two heaviest combinations will be present, i.e. H_3, H_4.

After our unquenched analysis, we decided to investigate possible sea quark effects and performing a quenched analysis at the same lattice spacing, using the dataset listed in the last row in Table 5.1. Note that all four heavy-light mesons were produced in the quenched case.

5.4 Dynamical Analysis and Results

The same criteria explained in section 4.5 for the choice of the fit ranges and the acceptance of χ^2/dof were adopted for the D_s analysis.

Table 5.2 shows the values of the masses obtained from uncorrelated fits to the four channels we are interested in: $P(0^-)$, $V(1^-), S(0^+)$, $A(1^+)$ label the pseudoscalar, vector, scalar and pseudovector or axial channel respectively, with the spin-parity composition specified in brackets. In the table the heavy-light meson type, as well as the fit range is specified. Figure 5.2 shows the typical effective masses for these channels. The left panels correspond to the heavy-light meson containing the lighter charm quark $am_c \sim 0.72$, i.e. H_3, while in the right panels $am_c \sim 0.9$, corresponding to the meson H_4. For the pseudoscalar and vector channels similarly reasonable plateaus are found for higher momenta. From Table 5.2 we can see that the masses obtained for the H_3 and H_4 mesons are consistent among the different ensembles. In particular the pseudoscalar and vector masses show a statistical error of less than 1%. Considering an average of the three values from the three ensembles, and using $a^{-1} = 1.62(4)\ GeV$, we can qualitatively estimate the range spanned by our H_3 and H_4 values in physical units:

$$P(0^-) \to [1840 - 2130]\ MeV; \quad V(1^-) \to [2030 - 2320]\ MeV. \tag{5.2}$$

Therefore the experimental values of the corresponding mesons,

$$D_s \rightarrow 1968.2(5)\ MeV; \qquad D_s^* \rightarrow 2112.0(6)\ MeV, \tag{5.3}$$

clearly lie in between our two heavy-light states, H_3 and H_4.

5.4.1 Dispersion Relation

We computed the meson masses at different lattice momenta and fit them to the dispersion relation. The dispersion relation is defined such that the $\mathcal{O}(m^2a^2)$ error is reflected in the deviation of c, the effective speed of light, from unity. The commonly used continuum-like expression is linear in the square of the momentum,

$$(E(p)a)^2 = (E(0)a)^2 + c^2(pa)^2, \tag{5.4}$$

where $pa = p_L a$ is the discretized lattice momentum

$$p_L a = \frac{2\pi\sqrt{n}}{La}, \quad n = n_x^2 + n_y^2 + n_z^2, \quad n \in \mathbb{Z}^+. \tag{5.5}$$

However, we performed both linear and quadratic fits, i.e. to the eq.(5.4) and to

$$(E(p)a)^2 = (E(0)a)^2 + c^2(pa)^2 + K(pa)^4 \tag{5.6}$$

respectively. Note here the $\mathcal{O}(a^4)$ term corresponds to a lattice artefact, as explained below. Also, following [75], we considered the momentum equal to $pa = 2\sin(\pi\sqrt{n}/La)$ in addition to the expression in (5.5). We concluded that fitting the energies to a quadratic expression with the momenta as in eq.(5.5), is in our case the best approach, as explained below[2].

---

[2] Only three momenta are available for the $am_{sea} = 0.03$ ensemble, i.e. there are only three points in the plot of energies versus momenta, so we found the linear fit with $pa = 2\sin(\pi\sqrt{n}/La)$ is the best one in the 0.03 case.

	Meson	$P(0^-)$	$V(1^-)$	$S(0^+)$	$A(1^+)$
m_{sea}					
0.01	H_3	1.133(2)	1.241(5)	1.393(17)	1.490(20)
		[10-16]	[12-16]	[8-13]	[8-14]
	H_4	1.315(3)	1.424(8)	1.569(18)	1.663(20)
		[11-16]	[12-16]	[8-14]	[8-13]
0.02	H_1	0.771(1)	0.913(4)	1.060(24)	1.013(43)
		[9,15]	[10,16]	[8,13]	[10,16]
	H_2	0.955(2)	1.083(3)	1.211(28)	1.179(38)
		[9,16]	[9,16]	[9,16]	[10,16]
	H_3	1.134(4)	1.255(7)	1.336(54)	1.481(36)
		[10,16]	[12,16]	[9,16]	[8,16]
	H_4	1.318(5)	1.443(12)	1.544(58)	1.671(37)
		[10,16]	[12,16]	[9,16]	[8,16]
0.03	H_3	1.133(3)	1.264(6)	1.443(67)	1.494(43)
		[12,16]	[10,16]	[9,16]	[9,14]
	H_4	1.317(5)	1.427(14)	1.584(42)	1.683(34)
		[12,16]	[12,16]	[8,16]	[8,16]
quenched	H_1	0.767(3)	0.938(6)	0.935(134)	1.023(107)
		[10,16]	[9,16]	[9,15]	[10,16]
	H_2	0.952(3)	1.102(5)	1.111(82)	1.200(81)
		[10,16]	[8,16]	[9,15]	[10,16]
	H_3	1.136(4)	1.275(8)	1.357(49)	1.491(52)
		[11,16]	[10,16]	[8,14]	[8,16]
	H_4	1.324(6)	1.456(11)	1.539(39)	1.645(64)
		[11,16]	[10,16]	[8,13]	[9,16]

Table 5.2: Fit results for the meson masses in lattice units for all the heavy-light possibilities and ensembles. Below each mass value the corresponding fit range is specified.

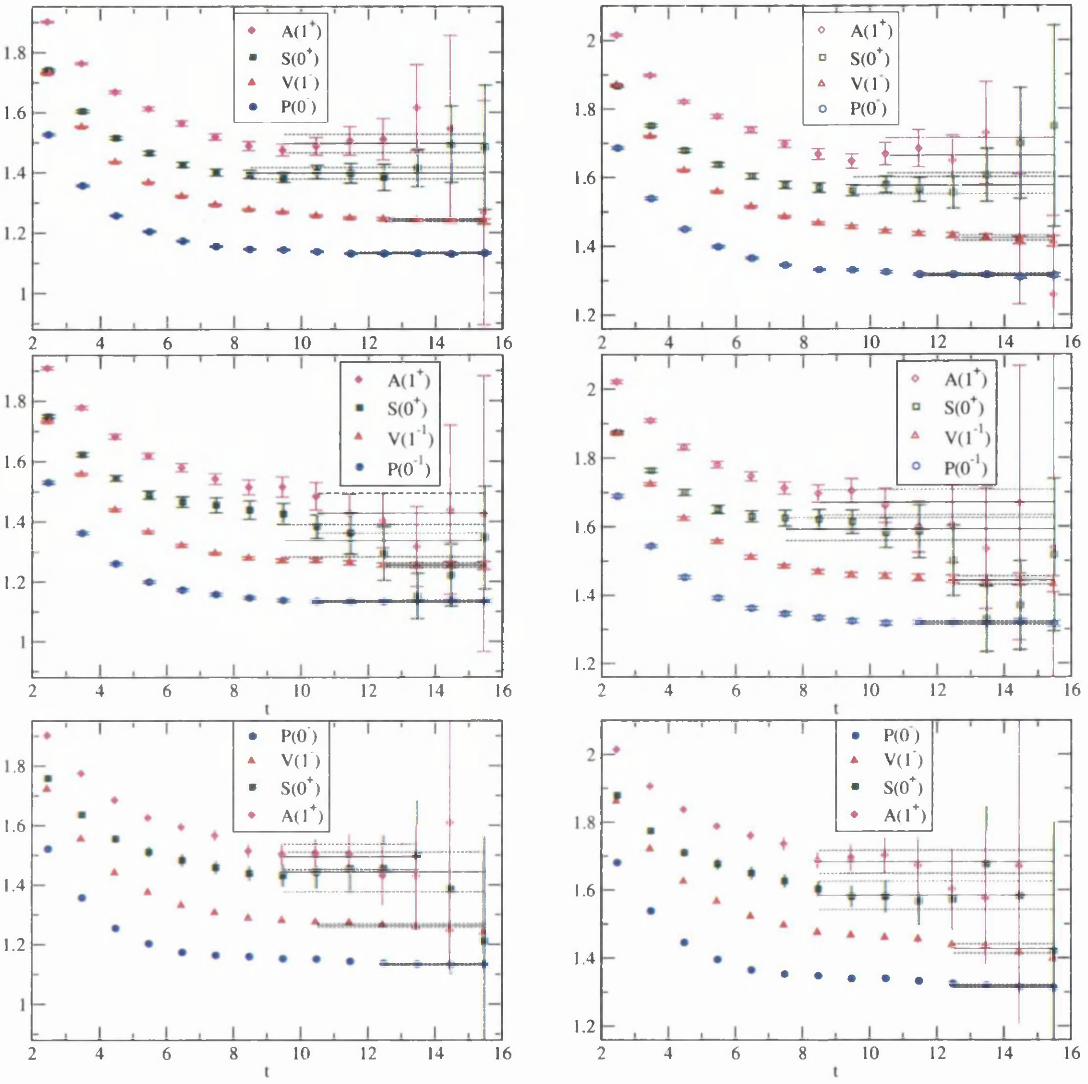

Figure 5.2: Effective masses for the heavy-light mesons with charm mass $am_c \sim 0.72$ on the left panels, corresponding to the H_3 meson, and $am_c \sim 0.9$ on the right panels, corresponding to the H_4 meson. From the top to the bottom: $am_{sea} = 0.01,\ 0.02,\ 0.03$.

Figure 5.3 is an example of our investigation: it shows the dispersion relation for the pseudoscalar channel, upper panel, and the vector channel, lower panel, for the meson H_3, the lightest of the two considered here, in the $am_{sea} = 0.01$ case, where five different momenta are available. We also show in the plot the values of the speed of light obtained from the fit to eq.(5.6), $c = 0.897(12)$ for the pseudoscalar and 0.833(29) for the vector, higher than one might expect from [75], considering our heavy charm. For completeness, we list in Table 5.3 the c values for the pseudoscalar and vector mesons obtained from all our sets of data. Clearly, the heavier the meson, the lower is the c value obtained. However, the fact that simulating quarks as heavy as charm can give rise to more difficulties, in terms of higher lattice artefacts for instance, is a well known problem. One of the methods trying to overcome the problems with heavy quarks (i.e. $am_Q \sim 1$) is the Fermilab or Relativistic Heavy Quark approach [76]. It gives us an alternative interpretation of the dispersion relation. Here we recall the basic idea.

Considering the expansion of the energy-momentum relation in powers of the (lattice) momentum pa, we can write

$$(Ea)^2 = (M_1 a)^2 + \frac{M_1}{M_2}(pa)^2 + K(pa)^4 + ... \tag{5.7}$$

where M_1 is the rest mass, $M_1 = E(0)$, and M_2 is the so-called kinetic mass, $M_2^{-1} = (2\frac{\partial E}{\partial p_i^2})_{\mathbf{p}=0}$. The relativistic mass shell will have $M_1 = M_2$, and the expression above in the relativistic limit becomes the well known

$$(Ea)^2 = (M_1 a)^2 + c^2(pa)^2 \tag{5.8}$$

with $c^2 = 1$. In practice, at our non-relativistic mass, we cannot truncate the expansion at p^2, but we have to consider higher order terms, which take into account lattice corrections. The form of these corrections is not in the scope of this study, so we will simply indicate them δE_{lat}:

$$(Ea)^2 = (m_Q a)^2 + c^2(pa)^2 + \delta E_{lat}. \tag{5.9}$$

The rest mass of non-relativistic particles decouples from the interesting dynamics, since in the $m_Q \to \infty$ limit the heavy quark is at rest relative to the hadron. The suggestion from the Fermilab approach [76] is then considering M_2 instead of M_1 and tuning the couplings in the Lagrangian so that M_2 takes the physical value. In this preliminary analysis we consider both M_1 and M_2 and look at the dependence of the mass splittings on them, as explained in the following.

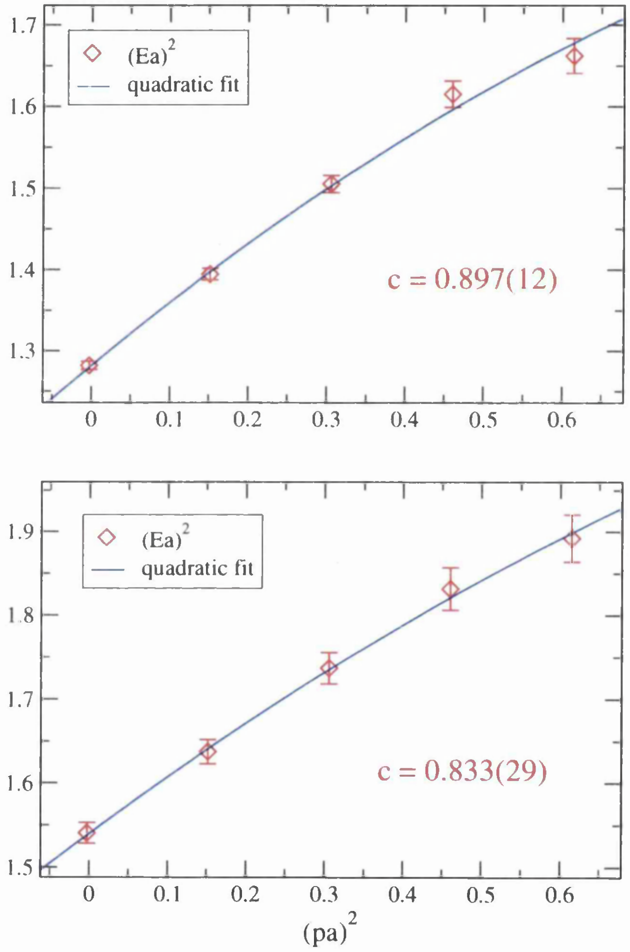

Figure 5.3: Dispersion relation plot for the pseudoscalar, upper panel, and vector channel, lower panel, of the H_3 meson in the $am_{sea} = 0.01$ case. A quadratic fit to eq.(5.6) was performed.

	Meson	$P(0^-)$	$V(1^-)$
am_{sea}			
0.01	H_3	0.897(12)	0.833(29)
	H_4	0.785(15)	0.720(37)
0.02	H_1	0.963(10)	1.001(26)
	H_2	0.940(9)	0.963(17)
	H_3	0.883(17)	0.850(44)
	H_4	0.808(21)	0.742(61)
0.03	H_3	0.862(22)	0.828(23)
	H_4	0.742(27)	0.647(47)
quenched	H_1	0.959(22)	0.964(45)
	H_2	0.900(18)	0.905(37)
	H_3	0.846(19)	0.826(35)
	H_4	0.763(22)	0.696(44)

Table 5.3: c values for all the pseudoscalar and vector mesons.

5.4.2 Mass Splittings

Our notation for the mass splittings considered the hyperfine and the scalar- and vector-parity splitting respectively, is as follows:

$$\begin{aligned} M_V - M_P &= 1^- - 0^- = \Delta H \\ M_S - M_P &= 0^+ - 0^- = \Delta S \\ M_A - M_V &= 1^+ - 1^- = \Delta V. \end{aligned} \tag{5.10}$$

In Table 5.4 the values of these splittings obtained for all the combinations of heavy-light mesons are listed in lattice units; in Table 5.5, the same values are in MeV, and the experimental values are also listed, as a guide for the reader. Figure 5.4 shows the splitting values obtained in the unquenched analysis versus am_{sea}. There is no discernible dependence on the sea quark mass, even for the hyperfine splitting, which has the smallest error bars[3]. However the hyperfine splitting is not well reproduced: our results are always overestimates compared with $\sim 144\ MeV$ from experiments. The values from the quenched calculation also overestimate the hyperfine splitting, contrary to what is previously found in literature.

Also, it is important to notice the larger statistics available for the $am_{sea} = 0.01$ ensemble, more than twice the $am_{sea} = 0.02,\ 0.03$ cases. So it is not surprising that the lightest ensemble gives results with sometimes smaller errors. In figure 5.4 we also inserted the values for the different splittings obtained for the H_1, H_2 mesons at $am_{sea} = 0.02$.

Following the considerations in section 5.4.1, we also performed some tests by computing the mass splittings defined in terms of M_2 instead of M_1. This means considering the masses equal to $M_2 = M_1/c^2$, where M_1 are the rest masses listed in Table 5.2 and the speed of light c values come from the dispersion relation fits, as explained in section 5.4.1. However, we often found bad signals at non-zero momenta, in particular in the scalar and axial cases. This meant that extracting c values was not always possible, so that we could not carry out a study of the mass splittings defined by the M_2 kinetic masses. In section 5.5 we consider using M_2 to determine the meson mass scale from the pseudoscalar channel.

---

[3] This clearly comes from the fact that the vector and pseudoscalar channels have good signals in all three ensembles, as the long plateaus in figure 5.2 show, while the axial and scalar ones become noisier going to higher mass, with larger error bars.

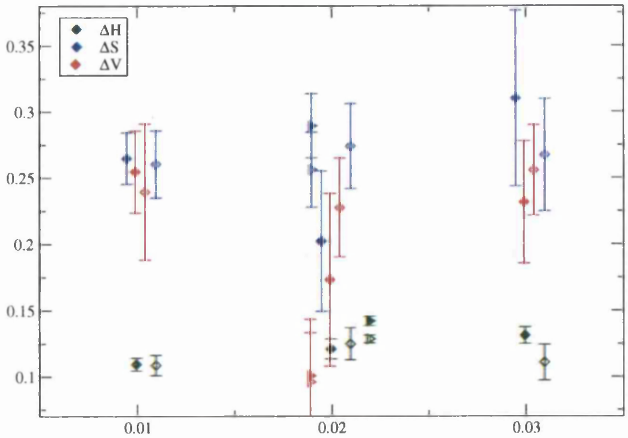

Figure 5.4: Mass splittings values in lattice units (Table 5.4) for H_3, full diamonds, and H_4, empty diamonds, plotted versus am_{sea}. The triangles, full and empty, represent values for H_1 and H_2 respectively, in the $am_{sea} = 0.02$ case. Note the shift in the x axis for clarity.

	Meson	ΔH	ΔS	ΔV
m_{sea}				
0.01	H_3	0.108(5)	0.260(17)	0.249(21)
	H_4	0.108(8)	0.254(18)	0.239(21)
0.02	H_1	0.142(4)	0.289(24)	0.100(43)
	H_2	0.128(3)	0.256(28)	0.096(37)
	H_3	0.121(8)	0.202(53)	0.227(36)
	H_4	0.125(12)	0.226(58)	0.228(37)
0.03	H_3	0.131(6)	0.310(67)	0.230(42)
	H_4	0.110(14)	0.267(43)	0.256(34)
quenched	H_1	0.171(6)	0.168(134)	0.084(106)
	H_2	0.150(5)	0.159(82)	0.098(80)
	H_3	0.139(7)	0.221(49)	0.217(50)
	H_4	0.131(10)	0.215(39)	0.189(62)

Table 5.4: Mass splittings values obtained in lattice units.

5.5 Dynamical plus Quenched

The values of the ground state masses obtained for all four heavy-light mesons generated from the quenched configurations are listed in Table 5.2. The corresponding mass splittings can be found in Tables 5.4 and 5.5, in lattice and physical units respectively.

In figures 5.5 the splittings in lattice units are plotted versus the inverse of the pseudoscalar mass $1/M_P$, where M_P is equal to M_1, the rest mass of the pseudoscalar meson, in the upper panel, and equal to M_2, the kinetic mass, in the lower one. The vertical dotted line corresponds to the experimental value of the D_S meson (using $a^{-1} = 1.62(4)$ GeV). As described in the previous section, our preliminary unquenched analysis shows a negligible dependence on the sea quark masses. Therefore we decide for clarity in these plots to show only one of the three ensembles studied, the $am_{sea} = 0.02$ one, since all four heavy-light mesons are present, as for the quenched case. The dynamical values are plotted as full symbols and the quenched values as empty symbols. We can see that quenched

	Meson	ΔH	ΔS	ΔV
m_{sea}				
0.01	H_3	175(8)	421(27)	403(34)
	H_4	176(13)	411(29)	387(34)
0.02	H_1	230(6)	469(39)	163(70)
	H_2	208(5)	415(46)	156(60)
	H_3	196(13)	327(86)	368(58)
	H_4	203(20)	366(94)	369(61)
0.03	H_3	212(10)	502(109)	373(68)
	H_4	179(22)	433(70)	415(56)
quenched	H_1	278(10)	273(217)	137(172)
	H_2	244(8)	258(132)	158(130)
	H_3	225(12)	358(79)	351(82)
	H_4	213(16)	348(63)	306(100)
Experiment		143.8(4)	349.1(6)	346.9(1.0)

Table 5.5: Mass splitting values in MeV, using $a^{-1} = 1.62\,GeV$. The experimental values are also showed.

and dynamical splitting values are consistent within the errors: therefore no sea quark effects are observed. The shift in the x axis in the second plot compared to the first reflects the deviation of the c values from unity (see also Table 5.3): this probably tells us that simulating the heavy charm quark as an overlap is not enough to get rid of $\mathcal{O}(a^2m_c^2)$ errors at our large lattice spacing without resorting to the M_2 definition of the meson mass.

Due to the spin degeneracy of the parity splitting, the ratio of the two parity splittings is expected to be equal to unity. From the experimental values in Table 5.5 we have in fact $\Delta V/\Delta S = 1^+ - 1^-/0^+ - 0^- \sim 0.994$. Figures 5.6 shows the values obtained for this ratio versus the inverse of the pseudoscalar meson mass $1/M_P$ in the upper plot, and versus the hyperfine splitting over the pseudoscalar meson mass $\Delta H/M_P$ in the lower one. In both plots $M_P = M_1$, the rest mass. As can be seen, the two heavier mesons, H_3 and H_4, have $\frac{\Delta V}{\Delta S} = 1$ within rather large errors. Going to lighter heavy quark masses, i.e. for the H_1 and H_2 mesons, the gap between the two parity splittings seems to increase in both quenched and unquenched.

5.6 Conclusions

In this chapter we described a preliminary study of D_s mesons. For the very first time these systems are studied in $2+1$ dynamical flavours, with the strange quark as a domain wall fermion and the charm quark as an overlap fermion. We found clear signals for all the four channels we were interested in, with the pseudoscalar and vector ones being the more stable. Very little if any dependence of the mass splittings on the sea quark mass is observed. However, the error bars in the parity

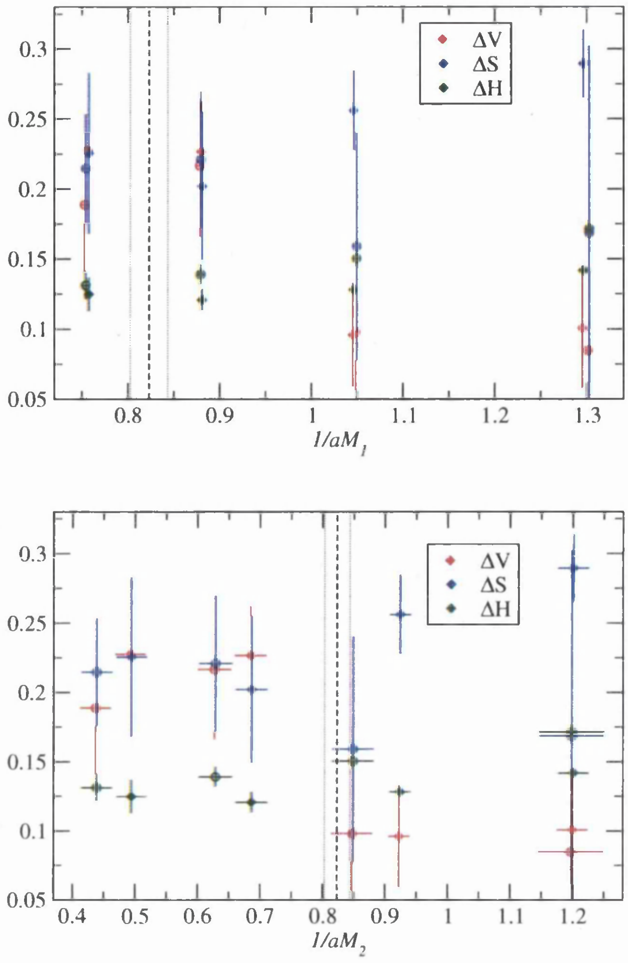

Figure 5.5: Mass splittings in lattice units versus the inverse of the pseudoscalar meson mass, equal to the rest mass M_1 in the upper panel and to the kinetic mass M_2 in the lower panel. The results for all the four mesons are plotted for both the $am_{sea} = 0.02$ ensemble, full symbols, and the quenched case, empty symbols.

splitting values are often very large, due to the fact that the scalar and axial channels are quite noisy. The hyperfine splitting always presents smaller errors, but the experimental value is not well reproduced: it is always overestimated, even in the quenched calculation. The ratio of the two parity splittings is close to the experimental value within the statistical errors, but we cannot draw any conclusion

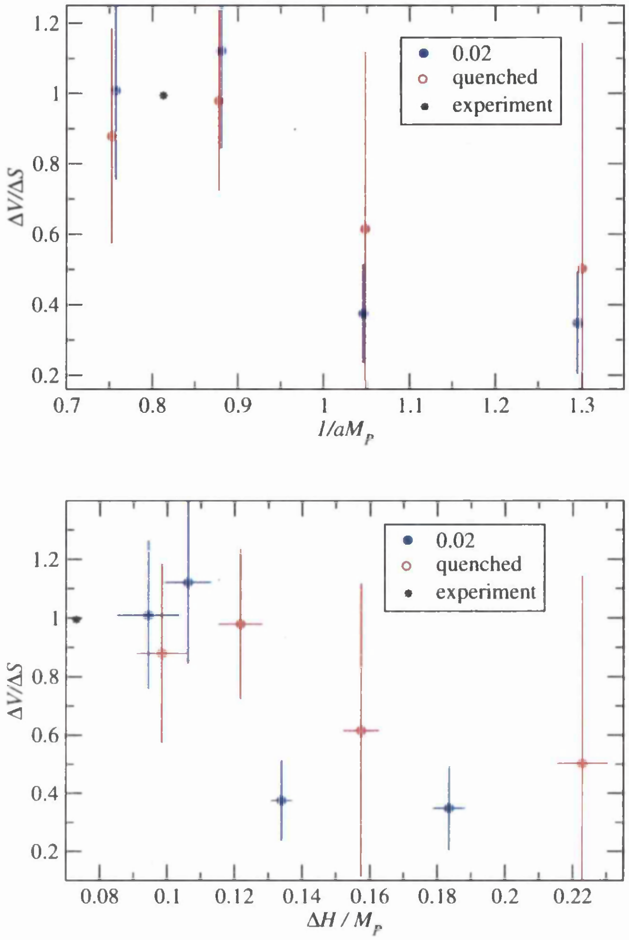

Figure 5.6: Here the ratio of the vector parity over scalar parity is plotted versus the inverse of the pseudoscalar mass in lattice units in the upper panel, and versus the ratio $\Delta H/M_P$ in the lower panel, with $M_P = M_1$, the rest mass, in both plots. The results for all the four mesons are plotted. The experimental values are also shown.

at this stage due to the very large error bars usually present. Better statistics is required for a more precise analysis. We tried to investigate possible sea quark effects comparing results from a quenched calculation, but we did not find the improvement we expected. We do not see significant difference in the two analysis, at least for the two heaviest heavy-light mesons, H_3 and H_4. Going to lighter heavy quark masses, we can see in both quenched and unquenched ($am_{sea} = 0.02$ case) that the gap between the two parity splittings tends to increase.

Following the suggestion from the Fermilab approach, we considered the kinetic meson mass $M_2 = M_1/c^2$ as alternative to the rest mass M_1 to determine the mass splittings, and tried to investigate possible dependence of the splittings themselves on these two masses. Unfortunately, the determination of the speed of light c from the dispersion relation was not always possible, due to the increased noise at higher momenta: therefore at this stage we could not carry out this kind of analysis. An appropriate choice of smearing operators, as well as increased statistics, may improve the signal in the scalar and axial channels and allow a more comprehensive study of the dispersion relation in terms of M_2. However, we used M_2 determined from the pseudoscalar channel and saw a shift on all the data to heavier masses (see figure 5.5): this means that by using M_2 instead of M_1 we could study D_s physics at charm mass values lighter than our initial choice.

At LO HQET, the hyperfine splitting for heavy-light mesons is expected to follow the inverse of the meson mass, $\Delta H \sim 1/M$ ($M \sim m_Q$). To test our lattice results, we plot in figure 5.7 the hyperfine splitting versus the inverse of the pseudoscalar meson mass, for all the four heavy-light mesons available in the quenched calculation. The diagonal line is a guide for the eye: we can see that our four points are not actually aligned, as we would expect. This probably tells us that the two heaviest of our mesons, on the left in the plot, are actually too heavy at our lattice spacing. It could be then that the effect of the $\mathcal{O}(a^2m_c^2)$ corrections is indeed significant. The RBC-UKQCD collaboration is now investigating these $\mathcal{O}(a^2m_c^2)$ errors: the generation of quenched configurations at a finer lattice spacing and larger volume is under progress.

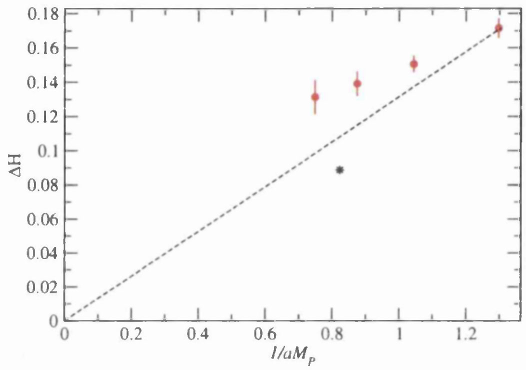

Figure 5.7: Hyperfine splitting versus the inverse of the pseudoscalar meson mass in quenched, with $M_P = M_1$, the rest mass (all in lattice units). The line is a guide for the eye, while the star symbol corresponds to the experimental value obtained by using $a^{-1} = 1.62(4)$ GeV.

Chapter 6

Conclusions

This thesis is composed of three self-standing projects, exploring different aspects of QCD and QCD-like theories through the lattice gauge formalism.

Chapter 1 and 2 introduce the background theory of this work.

Chapter 3 investigates the well known problem of the lack of asymptotic scaling in Monte Carlo simulations. We considered the improvement obtained by replacing the bare coupling constant in the perturbative expansion by some renormalized coupling, as pointed out in the past. However, the main purpose of our calculation was to emphasize how the lattice spacing corrections need to be included in the perturbative continuum-like expression of the lattice spacing in terms of the coupling $g_0^2(a)$. We fit quenched data to the running coupling expression based on these considerations. We also showed a first application of our approach to $SU(N)$ data, with the number of colours N different from 3 and checked its validity in particular at large N. By fitting the expression of the running coupling with and without $\mathcal{O}(a^n)$ terms, and using the bare lattice coupling as well as renormalized ones, our conclusions were that the lattice artefacts represent the dominant effect in the lack of asymptotic scaling. We also gave an estimate of the (pure-gauge)

$SU(3)$ $\Lambda_{\overline{MS}}$:

$$\Lambda_{\overline{MS}} = 217 \pm 21 \; MeV. \tag{6.1}$$

Chapter 4 presented an analysis of the nucleon state and its parity partner on 2 + 1 flavour domain wall gauge configurations generated by the RBC-UKQCD collaboration. Correlation functions at unitary and partially-quenched points, as well as with different types of smearing were included in this study. By performing multiple fits to different correlators we aimed to minimize the systematic errors arising from different features of the operators. We considered two different lattice volumes, $16^3 \times 32$ and $24^3 \times 64$, in order to estimate possible finite size effects for the observables of interest. This work is at fixed lattice spacing corresponding to $a^{-1} = 1.62(4)\; GeV$. After discarding the possibility of significant finite size effects, we extracted physical values for the masses of the $N(939)$ and $N(1535)$ states from the large volume. The value for the nucleon mass obtained from an extrapolation in both the lightest sea and valence quarks is

$$M_N = 957^{+46+46}_{-58-0} \; MeV, \tag{6.2}$$

where the first error is statistical and the second takes into account the shift in the value obtained considering different sea-valence extrapolations. Less clear signals were found for the nucleon parity partner N^*, resulting in a more difficult determination. From an extrapolation in both the lightest sea and valence quarks we quoted

$$M_{N^*} = 1422^{+60+45}_{-57-0} \; MeV, \tag{6.3}$$

with the errors as in (6.2). This value is much lower than the experimental one. However, after investigating the possibility of our N^* decaying in the lighter state

$N + \pi$ at sufficiently light quark masses, we concluded that the state isolated in this work is actually N^*.

In chapter 5 preliminary results of the first study of the D_s meson spectrum in 2 + 1 dynamical flavours were presented. The same domain wall gauge background as in chapter 4 was considered, on the small volume, $16^3 \times 32$, at a single lattice spacing. The strange quark was simulated as a domain wall fermion and the charm quark as an overlap fermion. A dispersion relation analysis was performed and the mass splittings between different J^P channels extracted, in order to compare them with their well determined experimental values. This study is a very preliminary investigation of possible $\mathcal{O}(a^n m_c^n)$ errors suppression, due to the implementation of the charm quark as an overlap fermion. Unfortunately, the rather large statistical error bars do not allow us to draw any conclusion in the comparison with experimental values. Increasing the statistics and implementing smeared operators may reduce the error bars substantially. At this preliminary stage, the effect of $\mathcal{O}(a^2 m_c^2)$ corrections may be significant. Further investigations at finer lattice spacing are in progress.

Appendix A

Gell-Mann Matrices

The standard basis for the fundamental representation of $SU(3)$ is:

$$\lambda_1 = \frac{1}{2}\begin{pmatrix} 0 & 1 & 0 \\ 1 & 0 & 0 \\ 0 & 0 & 0 \end{pmatrix} \qquad \lambda_2 = \frac{1}{2}\begin{pmatrix} 0 & -i & 0 \\ i & 0 & 0 \\ 0 & 0 & 0 \end{pmatrix}$$

$$\lambda_3 = \frac{1}{2}\begin{pmatrix} 1 & 0 & 0 \\ 0 & -1 & 0 \\ 0 & 0 & 0 \end{pmatrix} \qquad \lambda_4 = \frac{1}{2}\begin{pmatrix} 0 & 0 & 1 \\ 0 & 0 & 0 \\ 1 & 0 & 0 \end{pmatrix}$$

$$\lambda_5 = \frac{1}{2}\begin{pmatrix} 0 & 0 & -i \\ 0 & 0 & 0 \\ i & 0 & 0 \end{pmatrix} \qquad \lambda_6 = \frac{1}{2}\begin{pmatrix} 0 & 0 & 0 \\ 0 & 0 & 1 \\ 0 & 1 & 0 \end{pmatrix}$$

$$\lambda_7 = \frac{1}{2}\begin{pmatrix} 0 & 0 & 0 \\ 0 & 0 & -i \\ 0 & i & 0 \end{pmatrix} \qquad \lambda_8 = \frac{1}{2\sqrt{3}}\begin{pmatrix} 1 & 0 & 0 \\ 0 & 1 & 0 \\ 0 & 0 & -2 \end{pmatrix}.$$

Appendix B

Grassmann Variables

The fermionic fields are represented by anticommuting Grassmann variables, belonging to the fundamental representation of $SU(3)$. The path integral over fermionic fields will therefore involve the integration of these variables, as explained below. The generators of the Grassmann algebra, $\{\theta_i\}$, satisfy the anticommutation relation

$$\{\theta_i, \theta_j\} = \theta_i\theta_j + \theta_j\theta_i, \tag{B.1}$$

where $i, j = 1, ..., n$ for a n-dimensional Grassmann algebra. The basic rules for the Grassmann integration are

$$\int d\theta_i = 0, \qquad \int d\theta_i\theta_i = 1, \tag{B.2}$$

where for multiple integrals the integration measures $\{d\theta_i\}$ anti-commute with themselves and the $\{\theta_i\}$,

$$\{\theta_i, d\theta_j\} = \{d\theta_i, d\theta_j\} = 0 \ \forall i, j. \tag{B.3}$$

We want to show that

$$\int \prod_{i=1}^{n} d\bar{\theta}_i d\theta_i exp(-\sum_{i,j=1}^{n} \bar{\theta}_i M_{i,j}\theta_j) = detM, \tag{B.4}$$

which represents the main application of the Grassmann algebra in the integration of the partition function (eq.(2.83)).

We can write

$$exp(-\sum_{i,j=1}^{n} \bar{\theta}_i M_{i,j} \theta_j) = \prod_{i=1}^{n} exp(-\bar{\theta}_i \sum_{j=1}^{n} M_{i,j} \theta_j) \tag{B.5}$$

$$= \prod_{i=1}^{n} (1 - \bar{\theta}_i \sum_{j_i=1}^{n} M_{i,j_i} \theta_{j_i}), \tag{B.6}$$

since only the first two terms in the expansion of the exponential will contribute, due to $\theta_i^2 = 0$. Due to (B.1), only the terms proportional to $\bar{\theta}_i$ will contribute to the integral, in particular those terms that contains the product $\theta_1 \theta_2 \cdots \theta_n$ since repeated θ's give zero. They have the form[1]

$$\sum_{j_1 \cdots j_n} \theta_{j_1} \bar{\theta}_1 \cdots \theta_{j_n} \bar{\theta}_n M_{1 j_1} \cdots M_{n j_n}. \tag{B.7}$$

Since the product of Grassmann variables in (B.7) is antisymmetric under the exchange of any pair of indices j_i, we can rewrite eq.(B.7) as

$$\theta_1 \bar{\theta}_1 \cdots \theta_n \bar{\theta}_n \sum_{j_1 \cdots j_n} \epsilon_{j_1, \cdots, j_n} M_{1 j_1} \cdots M_{n j_n}, \tag{B.8}$$

where $\epsilon_{j_1, \cdots, j_n}$ is the ϵ tensor in n dimensions. Recalling the definition of the determinant of a matrix,

$$detM = \sum_{j_1 \cdots j_n} \epsilon_{j_1, \cdots, j_n} M_{1 j_1} \cdots M_{n j_n}, \tag{B.9}$$

we have

$$\int \prod_{i=1}^{n} d\bar{\theta}_i d\theta_i exp(-\sum_{i,j=1}^{n} \bar{\theta}_i M_{i,j} \theta_j) = detM (\prod_{i=1}^{n} \int d\bar{\theta}_i d\theta_i \bar{\theta}_i \theta_i) \tag{B.10}$$

$$= detM. \tag{B.11}$$

---

[1] Note $\bar{\theta}_1 \theta_{j_1} = -\theta_{j_1} \bar{\theta}_1$.

Bibliography

[1] K. G. Wilson, Phys. Rev. D **10** (1974) 2445.

[2] Y. Iwasaki, UTHEP-118.

[3] T. Takaishi, Phys. Rev. D **54** (1996) 1050.

[4] J. B. Kogut and L. Susskind, Phys. Rev. D **11** (1975) 395.
L. Susskind, Phys. Rev. D **16** (1977) 3031.

[5] H. B. Nielsen and M. Ninomiya, Nucl. Phys. B **185** (1981) 20 [Erratum-ibid. B **195** (1982) 541].

[6] R. Gupta, arXiv:hep-lat/9807028.

[7] P. H. Ginsparg and K. G. Wilson, Phys. Rev. D **25** (1982) 2649.

[8] R. Narayanan and H. Neuberger, Nucl. Phys. B **412** (1994) 574 [arXiv:hep-lat/9307006].

[9] For reviews, see for example,
H. Neuberger, Phys. Rev. Lett. **81**, 4060 (1998) [arXiv:hep-lat/9806025];
H. Neuberger, arXiv:hep-lat/9910040;
H. Neuberger, Chin. J. Phys. **38** (2000) 533 [arXiv:hep-lat/9911022].

[10] D. B. Kaplan, Phys. Lett. B **288**, 342 (1992) [arXiv:hep-lat/9206013].

[11] Y. Shamir, Nucl. Phys. B **406**, 90 (1993) [arXiv:hep-lat/9303005].

[12] V. Furman and Y. Shamir, Nucl. Phys. B **439**, 54 (1995) [arXiv:hep-lat/9405004].

[13] T. Blum, Nucl. Phys. Proc. Suppl. **73** (1999) 167 [arXiv:hep-lat/9810017].
S. Aoki, T. Izubuchi, Y. Kuramashi and Y. Taniguchi, Nucl. Phys. Proc. Suppl. **83**, 624 (2000) [arXiv:hep-lat/9909154].
S. Aoki, T. Izubuchi, Y. Kuramashi and Y. Taniguchi, Phys. Rev. D **62**, 094502 (2000) [arXiv:hep-lat/0004003].

[14] N. Metropolis, A. W. Rosenbluth, M. N. Rosenbluth, A. H. Teller and E. Teller, J. Chem. Phys. **21** (1953) 1087.

[15] S. Duane, A. D. Kennedy, B. J. Pendleton and D. Roweth, Phys. Lett. B **195**, 216 (1987).

[16] A. D. Kennedy, arXiv:hep-lat/0607038.

[17] M. A. Clark and A. D. Kennedy, Nucl. Phys. Proc. Suppl. **129** (2004) 850 [arXiv:hep-lat/0309084].

[18] M. A. Clark, Ph. de Forcrand and A. D. Kennedy, PoS **LAT2005** (2006) 115 [arXiv:hep-lat/0510004].

[19] M. A. Clark and A. D. Kennedy, Phys. Rev. Lett. **98** (2007) 051601 [arXiv:hep-lat/0608015].

[20] **RBC-UKQCD** Collaboration, D. J. Antonio *et. al., Production and properties of* $2+1$ *flavour DWF ensembles, PoS* **LAT2006** (2006) 188.

[21] P. Bacilieri *et al.* [Ape Collaboration], Nucl. Phys. B **317** (1989) 509.

[22] P. Boyle [UKQCD Collaboration], J. Comput. Phys. **179** (2002) 349 [arXiv:hep-lat/9903033].

P. Boyle *Heavy Meson Spectroscopy from the Lattice.* PhD thesis, University of Edinburgh, 1997.

[23] S. Gusken, Nucl. Phys. Proc. Suppl. **17** (1990) 361.

[24] G. P. Lepage and P. B. Mackenzie, Phys. Rev. D **48** (1993) 2250 [arXiv:hep-lat/9209022].

[25] B. Alles, A. Feo and H. Panagopoulos, Nucl. Phys. B **491** (1997) 498 [arXiv:hep-lat/9609025].

[26] C. R. Allton, arXiv:hep-lat/9610016.

[27] R. G. Edwards, U. M. Heller and T. R. Klassen, Nucl. Phys. B **517** (1998) 377 [arXiv:hep-lat/9711003].

[28] R. Sommer, Nucl. Phys. B **411** (1994) 839 [arXiv:hep-lat/9310022].

[29] S. Necco, arXiv:hep-lat/0306005.

[30] A. Ali Khan *et al.* [CP-PACS Collaboration], Phys. Rev. D **65** (2002) 054505 [Erratum-ibid. D **67** (2003) 059901] [arXiv:hep-lat/0105015].

[31] B. Lucini, M. Teper and U. Wenger, JHEP **0406** (2004) 012 [arXiv:hep-lat/0404008].

[32] M. Guagnelli, R. Sommer and H. Wittig [ALPHA collaboration], Nucl. Phys. B **535** (1998) 389 [arXiv:hep-lat/9806005].

[33] C. R. Allton, V. Gimenez, L. Giusti and F. Rapuano, Nucl. Phys. B **489** (1997) 427 [arXiv:hep-lat/9611021].

[34] C. R. Allton, W. Armour, D. B. Leinweber, A. W. Thomas and R. D. Young, Phys. Lett. B **628** (2005) 125 [arXiv:hep-lat/0504022].

[35] B. Beinlich, F. Karsch, E. Laermann and A. Peikert, Eur. Phys. J. C **6** (1999) 133 [arXiv:hep-lat/9707023].

[36] M. Okamoto *et al.* [CP-PACS Collaboration], Phys. Rev. D **60** (1999) 094510 [arXiv:hep-lat/9905005].

[37] P. de Forcrand *et al.* [QCD-TARO Collaboration], Nucl. Phys. B **577** (2000) 263 [arXiv:hep-lat/9911033].

[38] G. S. Bali and K. Schilling, Phys. Rev. D **47** (1993) 661 [arXiv:hep-lat/9208028].

[39] O. Hashimoto, private communication.

[40] R. F. Dashen and D. J. Gross, Phys. Rev. D **23** (1981) 2340.

[41] H. Iso and S. Sakai, Nucl. Phys. B **285** (1987) 295.

[42] R. Horsley, H. Perlt, P. E. L. Rakow, G. Schierholz and A. Schiller [QCDSF Collaboration], Nucl. Phys. B **693** (2004) 3 [Erratum-ibid. B **713** (2005) 601] [arXiv:hep-lat/0404007].

[43] G. Parisi, LNF-80/52-P Presented at 20th Int.Conf. on High Energy Physics, Madison, Wis., Jul 17-23, 1980.

[44] A. X. El-Khadra, G. Hockney, A. S. Kronfeld and P. B. Mackenzie, Phys. Rev. Lett. **69** (1992) 729.

[45] G. S. Bali, arXiv:hep-lat/9311009.

S. P. Booth, D. S. Henty, A. Hulsebos, A. C. Irving, C. Michael and

P. W. Stephenson [UKQCD Collaboration], Phys. Lett. B **294** (1992) 385 [arXiv:hep-lat/9209008].

[46] B. Alles, M. Campostrini, A. Feo and H. Panagopoulos, Phys. Lett. B **324** (1994) 433 [arXiv:hep-lat/9306001].

[47] A. Di Giacomo and G. C. Rossi, Phys. Lett. B **100** (1981) 481.

[48] B. Lucini, M. Teper and U. Wenger, JHEP **0401**, 061 (2004) [arXiv:hep-lat/0307017].

[49] B. Lucini, M. Teper and U. Wenger, JHEP **0502**, 033 (2005) [arXiv:hep-lat/0502003].

[50] B. Lucini and M. Teper, JHEP **0106**, 050 (2001) [arXiv:hep-lat/0103027].

[51] B. Lucini, private communication.

[52] M. Teper, private communication.

[53] G. 't Hooft, Nucl. Phys. B **72** (1974) 461.
E. Witten, Nucl. Phys. B **160**, 57 (1979).

[54] C. Allton *et al.* [RBC Collaboration], Phys. Rev. D **76** (2007) 014504 [arXiv:hep-lat/0701013].

[55] [RBC-UKQCD Collaboration] "2+1 flavor domain wall QCD on a (3-fm)**3 lattice: light meson spectrum, leptonic decays and neutral kaon mixing with L(s) = 16,". To be published.

[56] C. W. Bernard *et al.*, Phys. Rev. D **62** (2000) 034503 [arXiv:hep-lat/0002028].

[57] M. Li, PoS **LAT2006** (2006) 183 [arXiv:hep-lat/0610106].

[58] M. Luscher, "Selected Topics In Lattice Field Theory," Lectures at the 1988 Les Houches Summer School, North Holland, 1990.

[59] M. Lin "Hadron Physics with 2+1 Flavors of Domain Wall Fermions on the Lattice", Ph.D Thesis.

[60] C. M. Maynard *et al.* [RBC and UKQCD Collaborations], PoS **LAT2006** 189.

[61] B. Aubert *et al.* [BABAR Collaboration], Phys. Rev. Lett. **90** (2003) 242001 [arXiv:hep-ex/0304021].

[62] D. Besson *et al.* [CLEO Collaboration], AIP Conf. Proc. **698** (2004) 497 [arXiv:hep-ex/0305017].

[63] W. A. Bardeen, E. J. Eichten and C. T. Hill, Phys. Rev. D **68** (2003) 054024 [arXiv:hep-ph/0305049].

[64] G. Bonvicini *et al.* [CLEO Collaboration], Phys. Rev. D **70** (2004) 112004 [arXiv:hep-ex/0411050].

[65] M. Artuso *et al.* [CLEO Collaboration], Phys. Rev. Lett. **95** (2005) 251801 [arXiv:hep-ex/0508057].

[66] M. Artuso *et al.* [CLEO Collaboration], arXiv:0704.0629 [hep-ex].

[67] P. Boyle [UKQCD Collaboration], Nucl. Phys. Proc. Suppl. **63** (1998) 314 [arXiv:hep-lat/9710036].

[68] J. Hein *et al.*, Phys. Rev. D **62** (2000) 074503 [arXiv:hep-ph/0003130].

[69] G. S. Bali, Phys. Rev. D **68** (2003) 071501 [arXiv:hep-ph/0305209].

[70] M. di Pierro *et al.*, Nucl. Phys. Proc. Suppl. **129** (2004) 328 [arXiv:hep-lat/0310045].

[71] A. Dougall, R. D. Kenway, C. M. Maynard and C. McNeile [UKQCD Collaboration], Phys. Lett. B **569** (2003) 41 [arXiv:hep-lat/0307001].

[72] S. Ohta, H. Lin and N. Yamada [RBC Collaboration], PoS **LAT2005** (2006) 096 [arXiv:hep-lat/0510071].
H. W. Lin, S. Ohta and N. Yamada [RBC Collaboration], Nucl. Phys. Proc. Suppl. **153** (2006) 199.

[73] W. A. Bardeen and C. T. Hill, Phys. Rev. D **49** (1994) 409 [arXiv:hep-ph/9304265].

[74] M. L. Goldberger and S. B. Treiman, Phys. Rev. **110** (1958) 1178.

[75] K. F. Liu, Int. J. Mod. Phys. A **20** (2005) 7241 [arXiv:hep-lat/0206002].

[76] A. X. El-Khadra, A. S. Kronfeld and P. B. Mackenzie, Phys. Rev. D **55** (1997) 3933 [arXiv:hep-lat/9604004].